## *Low multiplicity pion proton interactions at 5.0 and 11.5 Gev/c*

Pearson, George Edward

# LOW MULTIPLICITY PION PROTON INTERACTIONS AT 5·0 AND 11·5 GEV/C

A thesis presented

by

George Edward Pearson B.Sc.

for the

Degree of Doctor of Philosophy

at the

University of Durham

May 1969

## ABSTRACT

The interactions of positive pi-mesons in a hydrogen bubble chamber have been studied at incident momenta of 5·0 Gev/c and 11·5 Gev/c. The various channel reactions have been separated by the processes of scanning, measuring, and computer analysis.

The total cross sections are 26·5mb and 24·9mb at 5 Gev/c and 11·5 Gev/c respectively. The elastic channel has been found to exhibit an energy independent optical diffraction character in that the slopes of the very forward differential cross sections remain in the region of 7-9 $Gev^{-2}$ over a large energy range.

The inelastic reaction $\pi^+p \rightarrow \pi^+p\pi^o$ shows the production of the $N^{*++}(1236)$ and $\rho^+(760)$ resonances in highly peripheral interactions. However, the fraction of such quasi-two-body reactions falls sharply from 24·8% at 5 Gev/c to 8·2% at 11·5 Gev/c.

The $\rho^+(760)$ differential cross section and decay density matrix elements are in reasonable agreement with absorptive peripheral model predictions for one pion exchange, whereas the $N^{*++}(1236)$ differential cross section disagrees with the model prediction for $\rho$ exchange. However, the Regge pole model for $\rho$ trajectory exchange gives a reasonable fit to the $N^{*++}$ differential cross section at both energies.

The slopes of the differential cross sections for $N^{*++}$ and $\rho^+$ production have been found to have values in the range 7-9 $Gev^{-2}$ of the same order as that for elastic scattering, indicating, rather qualitatively, an optical diffraction nature for the reactions.

The NO FIT reactions (with more than one neutral particle in the final state) show production of the $\eta^o(550)$ and $f^o(1260)$ mesons, and also the quasi-two-body production of $N^{*++}\eta^o$ and $N^{*++}f^o$. There is evidence for the $A_2(1300)$ meson and possibly the $A_3(1640)$ meson, although it is only observed at 5 Gev/c.

CONTENTS

# PREFACE

This thesis is an account of the work carried out by the author whilst at Durham University and contains a description of the investigations made into the various aspects of the interactions of pi-mesons with protons. The work on the analysis of the two pronged events forms part of two general experiments on the interactions of pi-mesons with protons at 5·0 Gev/c and 11·5 Gev/c undertaken by the High Energy Nuclear Physics Group of Durham University in collaboration with similar groups in Bonn, Nijmegen, Paris, and Turin at 5·0 Gev/c, and in Hamburg, Genoa, Milan, and Saclay at 11·5 Gev/c. However, at the time of writing data was unavailable from Bonn, Paris, Turin, and Hamburg.

The author has been concerned with most stages of both experiments: the 11·5 Gev/c exposure at CERN, the scanning and measurement of the films, and the investigations undertaken in Durham on the available data.

# LIST OF TABLES

## LIST OF FIGURES

Figure

13 A Diagram of fiducial volume in the 2 metre CERN bubble chamber

B Diagram of fiducial volume in the British National bubble chamber

14 Block diagram of Moire fringe digitization

15 System of co-ordinate punching on Moire fringe machines

16 Schematic diagram of co-ordinate punching on the Coventry machine

17 Block diagram of mechanical digitization

18 Bubble density vs momentum. Proton, kaon, and pion tracks

19 $\chi^2$ and $MM^2$ for the reaction $\pi^+p \rightarrow \pi^+p$ at 5 Gev/c

A $\chi^2$

B $MM^2$

20 $\chi^2$ and $MM^2$ for the reaction $\pi^+p \rightarrow \pi^+p\pi^o$ at 5 Gev/c

A $\chi^2$

B $MM^2$

21 $\chi^2$ and $MM^2$ for the reaction $\pi^+p \rightarrow \pi^+\pi^+n$ at 5 Gev/c

A $\chi^2$

B $MM^2$

22 $\chi^2$ for the reaction $\pi^+p \rightarrow \pi^+p$ at 11·5 Gev/c

23 $\chi^2$ for the reaction $\pi^+p \rightarrow \pi^+p\pi^o$ at 11·5 Gev/c

24 $\chi^2$ for the reaction $\pi^+p \rightarrow \pi^+\pi^+n$ at 11·5 Gev/c

25 $MM^2$ for the reaction $\pi^+p \rightarrow \pi^+p$ at 11·5 Gev/c

26 $MM^2$ for the reaction $\pi^+p \rightarrow \pi^+p\pi^o$ at 11·5 Gev/c

Figure

27 $MM^2$ for the reaction $\pi^+p \rightarrow \pi^+\pi^+n$ at 11·5 Gev/c

28 $MM^2$ vs ME for the reactions $\pi^+p \rightarrow \pi^+p$ and $\pi^+p \rightarrow \pi^+p\pi^o$ (Durham data)

A 11·5 Gev/c

B 5 Gev/c

29 $\pi^+p$ inelastic cross sections at various incident momenta

A $\pi^+p \rightarrow \pi^+p\pi^o$

B $\pi^+p \rightarrow \pi^+\pi^+n$

30 t vs $\phi$ in the reaction $\pi^+p \rightarrow \pi^+p$

A 11·5 Gev/c

B 5 Gev/c

31 Differential cross section $(\delta\sigma/\delta t)$ for the reaction $\pi^+p \rightarrow \pi^+p$ at 5 Gev/c

A All t values

B $-t < 0{\cdot}6$ Gev$^2$

32 Differential cross section $(\delta\sigma/\delta t)$ for the reaction $\pi^+p \rightarrow \pi^+p$ at 11.5 Gev/c

A All t values

B $-t < 0{\cdot}6$ Gev$^2$

33 Centre of mass momentum (P*) for the inelastic reactions at 5 Gev/c

A Reaction (B) $\pi^+p \rightarrow \pi^+p\pi^o$

B Reaction (C) $\pi^+p \rightarrow \pi^+\pi^+n$

34 Centre of mass angle ($\theta$*) distributions for the inelastic reactions at 5 Gev/c

Figure

A Reaction (B) $\pi^+p \rightarrow \pi^+p\pi^o$

B Reaction (C) $\pi^+p \rightarrow \pi^+\pi^+n$

35 $M(p\pi^+)$ vs $M(\pi^+\pi^o)$ in reaction $\pi^+p \rightarrow \pi^+p\pi^o$ at 5 Gev/c

36 $M(p\pi^o)$ vs $M(\pi^+\pi^o)$ in reaction $\pi^+p \rightarrow \pi^+p\pi^o$ at 5 Gev/c

37 $M(n\pi^+)$ vs $M(\pi^+\pi^o)$ in reaction $\pi^+p \rightarrow \pi^+\pi^+n$ at 5 Gev/c

38 $M(p\pi^+)$ and $M(p\pi^o)$ in reaction $\pi^+p \rightarrow \pi^+p\pi^o$ at 5 Gev/c

A $M(p\pi^+)$

B $M(p\pi^o)$

39 $M(\pi^+\pi^o)$ in reaction $\pi^+p \rightarrow \pi^+p\pi^o$ at 5 Gev/c

A Selected events

B Outside $MM^2$ cuts

40 $M(n\pi^+)$ and $M(\pi^+\pi^+)$ in reaction $\pi^+p \rightarrow \pi^+\pi^+n$ at 5 Gev/c

A $M(n\pi^+)$

B $M(\pi^+\pi^+)$

41 Chew Low plot of $M(p\pi^+)$ vs $t(p/p\pi^+)$ in reaction $\pi^+p \rightarrow \pi^+p\pi^o$ at 5 Gev/c

42 Chew Low plot of $M(\pi^+\pi^o)$ vs $t(\pi^+/\pi^+\pi^o)$ in reaction $\pi^+p \rightarrow \pi^+p\pi^o$ at 5 Gev/c

43 Peyrou Plots for $N^{*++}$ and $\rho^+$ production in reaction $\pi^+p \rightarrow \pi^+p\pi^o$ at 5 Gev/c

A $N^{*++}$

B $\rho^+$

44 $\delta\sigma/\delta t$ vs t distribution for $N^{*++}$ production in reaction $\pi^+p \rightarrow \pi^+p\pi^o$ at 5 Gev/c

45 $\delta\sigma/\delta t$ vs t distribution for $\rho^+$ production in reaction $\pi^+p \rightarrow \pi^+p\pi^o$ at 5 Gev/c

Figure

46 Jackson angular distributions at 5 Gev/c (the solid curves show the fits $A+B\cos^2\theta$ and $A+B\cos^2\phi$)

A $N^{*++}$

B $\rho^+$

47 Linear extrapolations of the function $-F(w,t)\times\mu^2/t$ vs $t/\mu^2$ in reaction $\pi^+p\rightarrow\pi^+p\pi^o$ at 5 Gev/c

48 Treiman Yang angle ($\theta$ TY) and $\sigma(\pi^+\pi^o)$ in reaction $\pi^+p\rightarrow\pi^+p\pi^o$ at 5 Gev/c

A Treiman Yang angle for $\rho^+$ ($-t < 0.3$ Gev$^2$)

B $\sigma(\pi^+\pi^o)$ ($-t < 0.26$ Gev$^2$)

49 $M(p\pi^+)$ and missing mass (MM) in reaction (D) $\pi^+p\rightarrow\pi^+p\pi^o$ ($m\pi^o$) $m \geqslant 1$ at 5 Gev/c

A $M(p\pi^+)$

B MM

50 MM and $M(\pi^+$+missing neutrals) in reaction (D) $\pi^+p\rightarrow\pi^+p\pi^o$ ($m\pi^o$) $m \geqslant 1$ at 5 Gev/c

A MM ( $M(p\pi^+)$ in $N^{*++}$ )

B $M(\pi^+$+neutrals) ( $M(p\pi^+)$ not in $N^{*++}$ )

51 $M(p\pi^+)$ vs $M(\pi^+\pi^o)$ in reaction $\pi^+p\rightarrow\pi^+p\pi^o$ at 11·5 Gev/c

52 Laboratory momenta of secondary pions

A 11·5 Gev/c

B 5 Gev/c

53 $MM^2$ assuming the reaction $d+p\rightarrow p+p+n$ for events fitted with the reaction $\pi^+p\rightarrow\pi^+p\pi^o$

54 Centre of mass momentum (P*) for the inelastic reactions at 11·5 Gev/c

A Reaction (B) $\pi^+p\rightarrow\pi^+p\pi^o$

Figure

B Reaction (C) $\pi^+p \rightarrow \pi^+\pi^+n$

55 Centre of mass angle ($\theta^*$) distributions for the inelastic reactions at 11·5 Gev/c

A Reaction (B) $\pi^+p \rightarrow \pi^+p\pi^o$

B Reaction (C) $\pi^+p \rightarrow \pi^+\pi^+n$

56 $M(p\pi^+)$ vs $M(\pi^+\pi^o)$ in reaction $\pi^+p \rightarrow \pi^+p\pi^o$ at 11·5 Gev/c

57 $M(p\pi^o)$ vs $M(\pi^+\pi^o)$ in reaction $\pi^+p \rightarrow \pi^+p\pi^o$ at 11·5 Gev/c

58 $M(n\pi^+)$ vs $M(\pi^+\pi^+)$ in reaction $\pi^+p \rightarrow \pi^+\pi^+n$ at 11·5 Gev/c

59 $M(p\pi^+)$ and $M(p\pi^o)$ in reaction $\pi^+p \rightarrow \pi^+p\pi^o$ at 11·5 Gev/c

A $M(p\pi^+)$

B $M(p\pi^o)$

60 $M(\pi^+\pi^o)$ in reaction $\pi^+p \rightarrow \pi^+p\pi^o$ at 11·5 Gev/c

A Selected events

B Before any cuts applied to data

61 $M(n\pi^+)$ and $M(\pi^+\pi^+)$ in reaction $\pi^+p \rightarrow \pi^+\pi^+n$ at 11·5 Gev/c

A $M(n\pi^+)$

B $M(\pi^+\pi^+)$

62 Chew Low plot of $M(p\pi^+)$ vs $t(p/p\pi^+)$ in reaction $\pi^+p \rightarrow \pi^+p\pi^o$ at 11·5 Gev/c

63 Chew Low plot of $M(\pi^+\pi^o)$ vs $t(\pi^+/\pi^+\pi^o)$ in reaction $\pi^+p \rightarrow \pi^+p\pi^o$ at 11·5 Gev/c

64 Peyrou plot and Jackson angular distributions for $N^{*++}$ in reaction $\pi^+p \rightarrow \pi^+p\pi^o$ at 11·5 Gev/c

A Peyrou plot for $N^{*++}$

B Jackson angles for $N^{*++}$ (the solid curves show the fits $A+B\cos^2\theta$ and $A+B\cos^2\phi$)

Figure

65 $\delta\sigma/\delta t$ vs t distribution for $N^{*++}$ production in reaction $\pi^+p \rightarrow \pi^+p\pi^o$ at 11.5 Gev/c

66 $M(p\pi^+)$ and missing mass (MM) in reaction (D) $\pi^+p \rightarrow \pi^+p\pi^o$ $(m\pi^o)$ $m \geq 1$ at 11.5 Gev/c

A $M(p\pi^+)$

B MM

67 MM and $M(\pi^+$+missing neutrals) in reaction (D) $\pi^+p \rightarrow \pi^+p\pi^o$ $(m\pi^o)$ $m \geq 1$ at 11.5 Gev/c

A MM ( $M(p\pi^+)$ in $N^{*++}$ )

B $M(\pi^+$+neutrals) ( $M(p\pi^+)$ not in $N^{*++}$ )

# INTRODUCTION

The construction of high energy beams of pions, kaons, and protons have enabled physicists to investigate the nature of the strong interaction of matter during the past few years. The bubble chamber has proved to be a particularly useful instrument in this repect in that a permanent record of an event can be kept on film.

The dominant feature of these investigations has been the discovery of the production of many resonant states which subsequently decay into two or more stable particles. The quantum numbers of most of these resonances have been determined and attempts made to classify them according to their quantum numbers.

From a theoretical point of view the type of interaction which lends itself most easily to theoretical investigation is that in which there are only two particles or resonances in the final state. Several theories, which have been examined critically over the past few years, have been put forward to explain this 'two-body' strong interaction, but as yet there appears to be no theory which satisfactorily explains all of the features. It is with these two-body processes in pion proton interactions that this thesis is mainly concerned.

In Chapter 1 a review is given of the strong interaction

with particular reference to the quantum numbers, classification schemes, and the various theoretical models employed to explain the two-body processes. Chapters 2 and 3 contain a description of the exposures at the CERN proton synchrotron and the methods of scanning, measuring, and classification of the events. The remaining chapters are concerned with the experimental results. In Chapter 4 the cross sections are given and checks made on the compatibility of the data from the different laboratories. Chapter 5 contains a description of the resonant states observed and a critical examination of the two-body processes in terms of the models reviewed in Chapter 1.

# CHAPTER 1

## A REVIEW OF STRONG INTERACTIONS

This chapter reviews briefly the subject of hadron interactions in which many baryon and meson resonant states have been found in formation and production experiments. Since in the strong interaction all quantum numbers are conserved there is first a description of the principal quantum numbers applied to the particle and resonant states and the consequent selection rules. Secondly there is a description of particle classification schemes, and finally a discussion of phenomenology and the most successful interaction models which have been applied particularly to the two-body and quasi-two-body processes.

### 1.1 Quantum numbers and conservation laws

Besides the conservation of energy, momentum, angular momentum, number of baryons, and number of leptons, there are other fundamental conservation laws which govern the strong interaction.

#### a) Isotopic spin (I)

The observation of charge independence in p-n and p-p

nuclear forces when they are in the same orbital angular momentum and spin state suggested that the proton and neutron are the charged components of a basic state called the nucleon. It is represented by a vector I in isotopic spin space (Cassen and Condon 1936). Isotopic spin I behaves like angular momentum $\ell$ in ordinary space in that I is quantized in one direction $I_3$ ('the charge axis') in analogy with the quantization $\ell_z$ of $\ell$, and the rules of addition of angular momentum apply directly to isotopic spin.

The nucleon has I = 1/2 with components $I_3 = \pm 1/2$ (representing the proton and neutron) along the 'charge axis' in isotopic spin space. The charge of the nucleon is given by

$$Q = I_3 + B/2$$

where B is the baryon number. The pion has I = 1 with components $I_3 = \pm 1, 0$ representing $\pi^+$, $\pi^-$, and $\pi^o$. Evidently for pions $I_3$ gives the charge directly (B = 0).

b) Parity (P)

The parity operation represents a reflection of the space co-ordinates of a wave function. In the reflected system the wave function may have either the same sign or the opposite sign to the original wave function corresponding to even or odd parity. In strong interactions the parity of a system before and after must remain the same, that is

parity is conserved. The orbital angular momentum ($\ell$) part of the wave function has even parity for even $\ell$ and odd parity for odd $\ell$, hence the parity is $(-1)^{\ell}$.

The intrinsic parity of particles must be introduced in strong interactions which involve creation or annihilation of particles. This is defined as even for the nucleon and determined experimentally for the other particles (the pion has odd parity).

Thus the parity of a two particle system with intrinsic parities $P_1$ and $P_2$ and relative orbital angular momentum $\ell$ is given by

$$P = P_1.P_2.(-1)^{\ell}$$

c) Charge conjugation (C)

Charge conjugation transforms particles into anti-particles as follows

$$C|\pi^{\pm}\rangle = +|\pi^{\mp}\rangle$$
$$C|\pi^{o}\rangle = +|\pi^{o}\rangle$$

Obviously charged particles are not eigenstates of C and no useful selection rules can be obtained by applying C alone. However, a $\pi^+\pi^-$ (boson-antiboson) combination must according to Bose statistics be symmetric to interchange of the space co-ordinates and charge. That is

$$C.P = +1$$

giving $$C(\pi^+\pi^-) = (-1)^{l}$$

Hence the decay $\rho^o \rightarrow \pi^+\pi^-$(p-wave) gives $C(\rho^o) = -1$.
It should be noted that only neutral particles can have a definite 'C-parity'.

d) G-Parity

Lee and Yang (1) suggested a new conserved quantity, G-parity, taking into account the simultaneous conservation of C and I in strong interactions, and defined by

$$G = C.\exp(i\pi I_2)$$

where $\exp(i\pi I_2)$ represents a rotation of $\pi$ around the 2-axis in isotopic spin space. It is at once obvious that although only the neutral member of a non-strange and non-baryon multiplet can be an eigenstate of C, the whole multiplet can be an eigenstate of G since the rotation around the $I_2$ axis again reverses the charge.
The G-parity of the pion multiplet can be found as follows. The zero-spin pion can be represented in isotopic spin space by the spherical harmonics

$$|\pi^o\rangle = Y_1^0 \quad \alpha \quad \cos\theta \quad = \quad z$$
$$|\pi^+\rangle = Y_1^1 \quad \alpha \quad -\sin\theta e^{i\phi} \quad = \quad -x-iy$$
$$|\pi^-\rangle = Y_1^{-1} \quad \alpha \quad \sin\theta e^{-i\phi} \quad = \quad x-iy$$

applying charge conjugation C

$$G|\pi^o\rangle = Ce^{i\pi I_2}|z\rangle = C|-z\rangle = C|-\pi^o\rangle = -|\pi^o\rangle$$
$$G|\pi^\pm\rangle = Ce^{i\pi I_2}|\mp x-iy\rangle = C|\mp x+iy\rangle = C|-\pi^\mp\rangle = -|\pi^\pm\rangle$$

and hence $G(\pi^{\mp o}) = -1$

From this it is evident that for a system of n pions $G = (-1)^{n_\pi}$, and since G is conserved in strong interactions the number of pions at a Feynman vertex must be even. Applying the above results to the decays

$$\omega^o \rightarrow 3\pi \quad \text{and} \quad \rho \rightarrow 2\pi$$

one obtains $G(\omega) = -1$ and $G(\rho) = +1$

For the neutral member of a multiplet ($I_3 = 0$) which is an eigenstate of C, G becomes $C.(-1)^I$. Thus it is only necessary to find G for the neutral member and then it applies to the whole multiplet.

e) Strangeness (S) and Hypercharge (Y)

The concept of strangeness was introduced by Gell Mann and Nishijima (2) to account for the strong production of the particles $K, \Lambda, \Sigma$, and $\Xi$ in pion-nucleon interactions and their weak decay back into pions and nucleons. The strong and weak interactions correspond to strangeness conservation and non-conservation respectively.

The strangeness of an isotopic multiplet is defined as twice the displacement of its centre of charge from the 'non-strange' nucleon or pion multiplet centre of charge

depending upon whether the multiplet being considered is baryonic or mesonic. Hence

$S(N,\pi) = 0 \quad S(\Lambda,\Sigma) = -1 \quad S(K) = +1 \quad S(\Xi) = -2 \quad S(\Omega) = -3$

The hypercharge is simply defined as twice the average charge of a multiplet. Hence

$$Y(N,K) = +1 \quad Y(\Lambda,\Sigma,\pi) = 0 \quad Y(\Xi) = -1 \quad Y(\Omega) = -2$$

Strangeness, hypercharge, and baryon number are related simply by

$$Y = S + B$$

Since strong interactions conserve the quantities I, P, J, and G all particles can be assigned these quantum numbers when produced in strong interactions in the form $I^G J^P$. For example for the ρ-meson

$$I^G J^P = 1^+ 1^-$$

With these quantum numbers various selection rules can be built up, as for example in the reaction $\pi^+ p \rightarrow N^{*++}\pi^o$ where the ρ-meson is the only possible exchange particle.

## 1.2 Particle classification

In view of the number of particles, including resonances, having definite quantum numbers it was a natural consequence

that attempts be made to group them into schemes or multiplets. This section will be entirely devoted to a discussion of unitary symmetry which has had a great deal of success in the classification and prediction of particles and resonances. As there are few particles that can be placed on Regge trajectories the Regge Pole model will not be treated until section (1.3 d) on interaction mechanisms for which its predictions are more useful.

a) SU(2)-SU(3)

Charge independence and the isotopic spin multiplets are consequences of the Special Unitary symmetry group SU(2). The application of 2x2 unitary unimodular transformations on the basic states p, n, $\bar{p}$, and $\bar{n}$ give rise to the singlets, doublets, triplets, and quartets in isotopic spin space.

Gell Mann (3) and Ne'eman (4) were able to extend SU(2) to the higher symmetry of SU(3) and 3x3 unitary unimodular transformations on 3 basic states (quantum numbers the same as for p, n, $\Lambda$) producing an 8-component unitary spin with the same $J^P$ but different hypercharge Y into which could be fitted the baryon octet $N, \Lambda, \Sigma$, and $\Xi (J^P = 1/2^+)$ and the meson octet $\pi, \eta$, and $K (J^P = 0^-)$.

By an extension of the dimensions, components of 1, 8, 10, and 27 could be generated to accomodate the baryon decuplet $N^*(1236), \Sigma^*(1385), \Xi^*(1530)$, and $\Omega^- (J^P = 3/2^+)$, the meson octet $K^*(892)$, $\rho$, and $\omega (J^P = 1^-)$, and the two meson

singlets $\phi$ ($J^P = 1^-$) and $X^o$ ($J^P = 0^-$).

The basic prediction of SU(2) and SU(3) is that the members of each multiplet should have the same mass. This obviously is not so. However, the small mass differences in the isotopic spin multiplets are due to violation of the SU(2) symmetry in electromagnetic interactions, that is I is not conserved. Similarly in SU(3) there is assumed to be a medium strong force violating the symmetry, non-conserving the new spin, and producing the large mass differences. Okubo (5) was able to produce a general mass formula which accurately predicted the mass differences.

The great achievement of SU(3) was in predicting the $\Omega^-$ (discovered by Barnes et al (6)) to complete the baryon decuplet, its mass being derived from the Okubo formula.

b) SU(6)

The supermultiplets of SU(3) have been interpreted by Gursey and Radicati (7) in terms of the 'quark model' where the 3 basic states become fractionally charged particles called 'quarks' with baryon number 1/3. The multiplets of SU(3) can thus be constructed on the assuption that baryons are formed of quark triplets and mesons of quark-antiquark doublets.

On this basis SU(3) has been successfully extended to the symmetry of SU(6) where the quarks are considered to have spin 1/2 thus giving 6 basic states. From SU(6) is

generated a meson singlet and 35-plet, and a baryon 56-plet. The meson singlet is the $X^o$ and the 35-plet breaks down into the two SU(3) octets and the singlet $\phi$. The baryon 56-plet breaks down into the SU(3) octet and decuplet. The quarks are assumed to be in an s-state, and the introduction of higher orbital angular momentum states gives higher spin multiplets such as the meson octet $f^o(1260)$, $A_2(1300)$, and $K_N(1420)$ ($J^P = 2^+$) and the singlet $f'(1515)$ ($J^P = 2^+$). The meson multiplets can be grouped together as $0^-$, $1^-$, and $2^+$ nonets.

There is still doubt as to the correct assignments of the less firmly established resonances and some multiplets still require members. Furthermore SU(6) is non-relativistic and attempts are being made to extend to higher symmetries to correct this. However, SU(3) and SU(6) have been strikingly successful in predicting mass differences in the multiplets and in estimating the magnetic moments of particles.

## 1.3 Interaction cross sections and mechanisms

This section is devoted to a description of interaction cross sections, elastic scattering, and the main interaction models which have been applied particularly to the two-body and quasi-two-body reactions at primary energies above 1 Gev.

### a) Cross sections

The total cross sections for K-N, N-N, and $\pi$-N interactions above 6 Gev/c primary momentum are shown in Fig.(1A). It is evident that they are all tending toward constant values. Further it can be seen that the cross sections for particle-particle and antiparticle-particle interactions are tending towards equality, as postulated by Pomeranchuk in 1956. This approach of total cross sections to a constant value implies that, as the energy increases and higher and higher multiplicity channels open, the lower multiplicity cross sections are decreasing.

At lower energies the elastic and inelastic cross sections for $\pi^+p$ interactions, Fig.(1B), exhibit sharp structure, and in particular the peak at an incident momentum of about 200 Mev/c in the elastic cross section was attributed to the first known resonant state of $\pi^+p$, namely the $N^{*++}(1236)$. Other enhancements can be explained in a similar manner.

b) Elastic scattering

The data quoted is taken from Focacci and Giacomelli (8) and Svensson (9).

The forward diffraction peak

At incident momenta above 1 Gev/c the elastic scattering angular distributions are dominated by a strong forward diffraction peak due to the absorption of incident waves by many open inelastic channels. Up to about 4 Gev/c $\pi p$ and $\bar{p}p$

FIG. 1

INTERACTION CROSS SECTIONS

A. HIGH ENERGY TOTAL CROSS SECTIONS

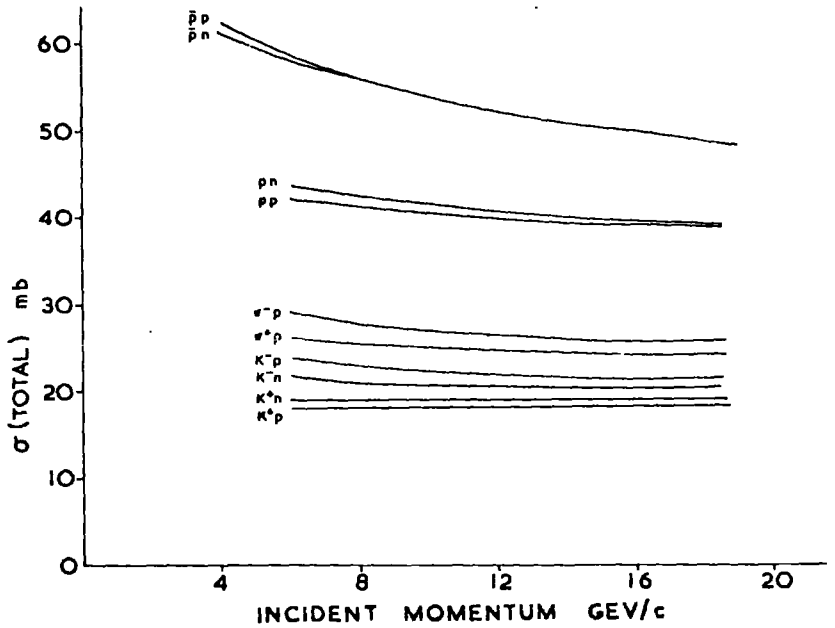


B. STRUCTURE IN LOW ENERGY PION-PROTON CROSS SECTIONS

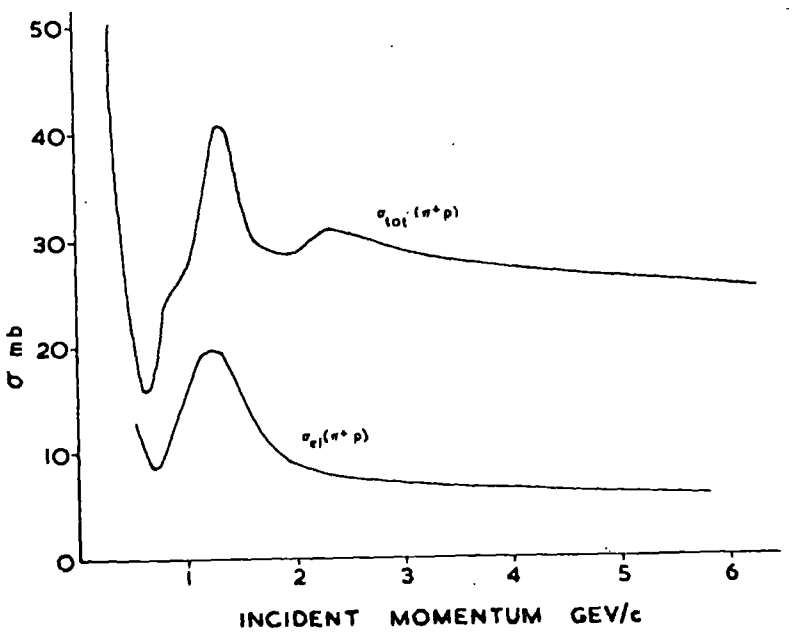

scattering show a 'dip-bump' structure, whereas above 4 Gev/c none of the reactions show structure.

The diffraction peaks can be fitted with an exponential of the form

$$\frac{\delta\sigma_{el}}{\delta t} = \left[\frac{\delta\sigma_{el}}{\delta t}\right]_o .\exp(At)$$

where t is minus the square of the 4-momentum transfer. A varies from ~5 ($K^+p$) to ~14 ($\bar{p}p$) $(Gev/c)^{-2}$, and is energy independant for $\pi p$ and $K^-p$ scattering. However, for pp and $K^+p$ scattering A increases (shrinking diffraction peak), and for $\bar{p}p$ A decreases (expanding diffraction peak). Above 5 Gev/c all reactions are fitted well by

$$\frac{\delta\sigma_{el}}{\delta t} = \left[\frac{\delta\sigma_{el}}{\delta t}\right]_o .\exp(At + Bt^2) \qquad -t \lesssim 2\ (Gev/c)^2$$

where A and B are approximately energy independent, but varying from reaction to reaction.

The optical model predicts secondary maxima and minima outside the diffraction peak and so agrees qualitatively with the experimental data below 4 Gev/c. For small t values the optical model gives for the differential cross section as an approximation

$$\frac{\delta\sigma_{el}}{\delta t} = \pi R^4 .\exp\left[+(R/2)^2 t\right]$$

thus the radius of the interaction volume R can be roughly determined from the slope A of the diffraction peak. For example $R \approx 1$ fermi for $\pi p$ scattering. However, the energy dependence of A and the departure from a pure exponential are features not explained by the optical model. Furthermore the model assumes that the scattering amplitude is purely imaginary and that there are no spin effects. Experimental results show that the ratio of the real part to imaginary part of the forward scattering amplitude is non-zero, except perhaps asymptotically. For example in pp scattering this ratio is 0.35 (5 Gev/c) and 0.15 (12 Gev/c). Polarization measurements for the same reaction at 6 Gev/c give a 20% contribution to the scattering amplitude from spin-flip terms.

It is therefore quite evident that any simple optical diffraction model can only reproduce the gross features of elastic scattering.

Large angle scattering

At a scattering angle of $\theta \approx 90^{\circ}$ the cross section is 6 to 12 orders of magnitude smaller than the forward cross section, and the best fits to this region seem to be obtained by using empirical exponentials.

Both $\pi p$ and Kp scattering show definite peaks in the backward direction ($\theta \approx 180^{\circ}$) about 100 times smaller than the forward peaks. These can be fitted with an exponential

similar to that used for the forward peaks but with slightly greater slope (10 to 20 $(Gev/c)^{-2}$). However, the cross section in the backward direction decreases rapidly with energy.

Charge exchange scattering shows the same general features except that for the reaction $\pi^- p \rightarrow \pi^o n$ the structure in the forward peak does not vanish with increasing energy. However, these reactions and quasi-two-body reactions can be treated in terms of the various particle exchange models.

c) The peripheral model

Many inelastic reactions also exhibit a strong forward-backward angular distribution, suggesting a dominance by a peripheral interaction. The peripheral model (introduced by Chew and Low (10)) has been applied to many inelastic low multiplicity reactions, especially the quasi-two-body type, between 1 and 8 Gev/c with some success. Fig.(2A) shows the Feynman diagram for such a process characterised by the exchange of a virtual particle e in the Yukawa potential field.

At this point it is best to define the Mendelstam variables s, t, and u with reference to Fig.(2A).

| | |
|---|---|
| $s = (P_a + P_b)^2$ | total centre of mass energy |
| $t = (P_a - P_c)^2$ | -(4-momentum transfer from a to c)$^2$ |
| $u = (P_a - P_d)^2$ | -(4-momentum transfer from a to d)$^2$ |

FIG. 2

FEYNMAN DIAGRAMS FOR A TWO BODY REACTION WITH PARTICLE EXCHANGE (e)

A) SIMPLE

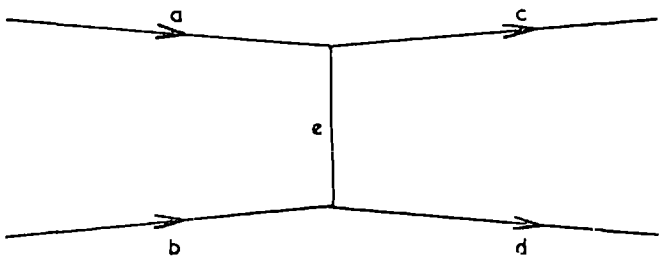


B) WITH INITIAL AND FINAL STATE INTERACTIONS (ABSORPTION)

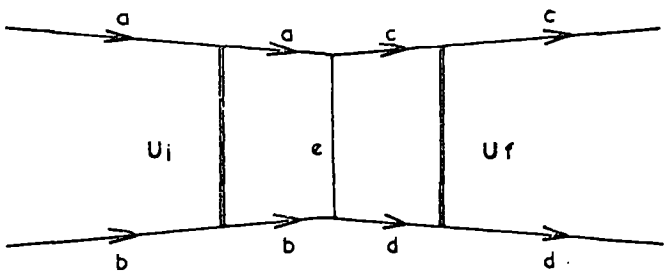

where $P_i$ is the 4-momentum of particle i.

From Feynman rules in lowest order perturbation theory the transition matrix element is given by

$$T(s,t) = V_{aec} \cdot \left[ \frac{1}{m_e^2 - t} \right] \cdot V_{bed}$$

$1/(m_e^2 - t)$ is the propagator of the exchange particle and $V_{aec}$ and $V_{bed}$ are the vertex functions which depend upon the coupling constants. The propagator term gives large amplitude for small t values close to the pole, thus giving qualitative agreement with experiment.

Jackson (11) has calculated the differential cross section for one pion exchange (O.P.E model) for the reaction $\pi^+ p \rightarrow \rho^+ p$

$$\frac{\delta\sigma}{\delta t} = \frac{(-\pi t)}{4 m_\rho^2 . m_p^2 . P^2} \cdot \left[ \frac{g^2}{4\pi} \right] \left[ \frac{G^2}{4\pi} \right] \frac{[(m_\rho - m_\pi)^2 - t]\,[(m_\rho + m_\pi)^2 - t]}{(m_\pi^2 - t)^2}$$

where g and G denote the $\rho\pi\pi$ and $\pi pp$ coupling constants respectively, and P is the laboratory momentum of the incident $\pi^+$. However, it disagrees strongly with experiment in magnitude and variation with t, and the dependance upon primary energy is wrong.

The main attempts to correct the model have been to introduce form factors and absorption processes.

Form factors

Ferrari and Selleri (12)and (13) introduced t-dependent form factors to allow for the fact that the exchange particle is off the mass shell, so that the propagator should be adjusted and the coupling constants replaced by the appropriate vertex functions. For example, in the reactions proceeding by pion exchange in the few Gev/c region, the $\delta\sigma/\delta t$ distributions are well reproduced by the form factor (Amaldi and Selleri (14))

$$F(t) = \frac{0.72}{1+\frac{(m_\pi{}^2-t)}{4.73m_\pi{}^2}} + \frac{0.28}{1+\left[\frac{m_\pi{}^2-t}{32m_\pi{}^2}\right]^2}$$

However, at higher energies a more complicated parameterization is necessary in order to reduce the predicted cross section for large t values. Moreover, to fit vector meson exchange reactions a form factor depending very strongly on t is needed which tends to mask the t dependence of the propagator. In order to account for the energy dependence a form factor is required which also depends upon the primary energy, whereas a true form factor should depend only on t.

Apart from pseudoscalar exchange the form factor approach is unsatisfactory and its physical significance is doubtful.

The absorption model

In high energy interactions there are many inelastic open channels competing with one another and contributing to the total cross section. In particular, the quasi-two-body process is reduced by this absorption which is stronger for smaller impact parameters (ie. low partial waves). Thus the contribution of the low partial waves to the quasi-two-body cross section is reduced, and since these correspond to large angle scattering the cross section for large t is reduced.

The absorption model, introduced by Sopkovitch (15) and developed by Gottfried and Jackson (16), takes account of the absorptive effects by initial and final state interactions $U_i$ and $U_f$ as illustrated in Fig.(2B). The reaction amplitude in the distorted wave Born approximation for potential V is

$$T_{fi} = \langle \psi_f | V | \psi_i \rangle$$

from which the amplitude has been calculated by Gottfried and Jackson (16) using the helicity representation of Jacob and Wick (17) for the general case of particles with spin

$$\langle \lambda_c \lambda_d | T^J | \lambda_a \lambda_b \rangle \approx e^{i\delta_J^+} \langle \lambda_c \lambda_d | B^J | \lambda_a \lambda_b \rangle e^{i\delta_J^+}$$

where $\lambda$ denotes the helicities, $\delta_J^+$ and $\delta_J^-$ are the complex scattering phase shifts in the initial and final states, and $B^J$ is the Born term for the Jth partial wave projection of T.

By assuming an optical model picture of elastic scattering in the initial and final states the phase shifts $\delta$ can be estimated (Svensson (18)).

On applying the absorption model to the reaction $\pi^+p \rightarrow \rho^+p$ (Gottfried and Jackson (19)) the necessary damping of the differential cross section is obtained. Furthermore, the initial and final state interactions explain the correlation between the plane of the two decay pions and the plane of the initial and final nucleons, which should not exist according to simple pseudoscalar exchange (Treiman and Yang (20)).

Angular correlations

If the particle d is a resonance decaying $d \rightarrow \alpha+\beta$ (see Fig.(3A)) then after its production d will, in general, be in a mixture of pure spin states, this mixture depending upon the vertex bed and $J_e{}^P e$, and is described by the (2J+1) dimensional density matrix of d with elements $\rho_{mm'}$.
For example for a J = 1 particle (eg. $\rho$) the density matrix is

$$\rho_{mm'} = \begin{vmatrix} \rho_{11} & \rho_{10} & \rho_{1,-1} \\ \rho^*_{10} & \rho_{00} & -\rho^*_{10} \\ \rho_{1,-1} & -\rho_{10} & \rho_{11} \end{vmatrix}$$

which leads to the decay angular distribution (Gottfried and Jackson (19))

FIG. 3

A) FEYNMAN DIAGRAM OF THE PRODUCTION AND DECAY OF A RESONANCE ($d \longrightarrow \alpha + \beta$)

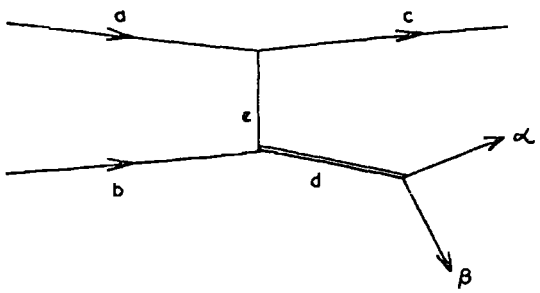


B) DEFINITION OF THE JACKSON ANGLES FOR RESONANCE d IN ITS OWN REST SYSTEM.

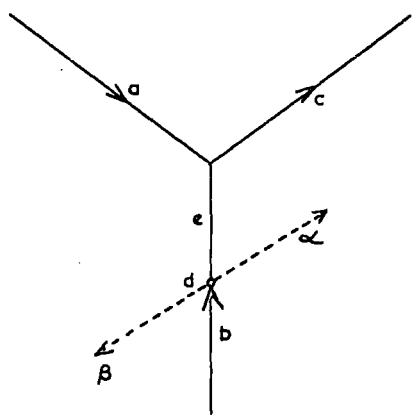


a, c, e, and b are coplanar (production plane)

α and β are collinear, but not in the production plane.

$$\cos\theta = \frac{\vec{b}\cdot\vec{\alpha}}{|\vec{b}||\vec{\alpha}|}$$

$$\cos\phi = \frac{\vec{a}\times\vec{c}}{|a\times c|}\cdot\frac{\vec{b}\times\vec{\alpha}}{|b\times\alpha|}$$

$$W(\theta,\phi) = \frac{3}{4\pi}\left[\rho_{00}\cos^2\theta+\rho_{11}\sin^2\theta-\rho_{1,-1}\sin^2\theta\cos2\phi-\sqrt{2}\mathrm{Re}(\rho_{10})\sin2\theta\cos\phi\right]$$

The angles $\theta$ and $\phi$ are defined in Fig.(3B). This relation is valid for any particle with a polarization vector which does not have a component in the production plane. Values for $\rho_{mm'}$ are predicted depending upon the exchange particle e.
For example the O.P.E model predicts for the reaction $\pi^+p\rightarrow\rho^+p$ that $\rho_{00} = 1$ and all the other elements zero. $N^{*++}$ production by $\rho$ exchange has been treated by Stodolsky and Sakurai (21) in analogy with the electromagnetic transition $N\gamma N^*$ since the $\rho$ has the same quantum numbers as the $\gamma$.

Experimental survey of the absorption model

The absorption model gives quite a satisfactory description of the matrix elements, energy dependence, and differential cross sections in most pseudoscalar ($\pi$) exchange processes such as $\pi^+p\rightarrow\rho^+p$ and $\pi^+p\rightarrow\rho^oN^{*++}$ for small t transfers for example at 4 Gev/c (22-25) and 8 Gev/c (26-28). But fails to describe photo-$\rho$ and photo-$\omega$ production.
The model properly predicts the matrix elements for processes dominated by vector exchange ($\rho$) such as $\pi^+p\rightarrow\pi^oN^{*++}$ at the above energies and $K^+p\rightarrow K^oN^{*++}$ at for instance 3 Gev/c (29,30). However, violent disagreement is found between the predicted cross section energy dependence and that observed, and the model fails to account for the shape of the differential cross-sections in some vector meson exchange reactions. For example

the reaction $K^+p \rightarrow K^oN^{*++}$ is fitted well but not the reaction $\pi^+p \rightarrow \pi^oN^{*++}$ unless form factors are introduced. For reactions requiring both pseudoscalar and vector meson exchange (eg. $K^+p \rightarrow K^{*+}p$) the differential cross sections are well fitted, but again the energy dependence is wrong.

A model which does provide an energy dependence in very reasonable agreement with experiment is the Regge Pole model.

d) The Regge pole model

From potential theory the scattering amplitude is given by

$$F(s,t) = \frac{8\pi\sqrt{s}}{k} \sum_{o}^{\infty} (2\ell+1) f_\ell(s) P_\ell(\cos\theta)$$

Regge (31) extended the partial wave amplitude $f_\ell(s)$ to hold for non-integer and complex values of angular momentum $\ell$, and several people (eg. Chew and Frautschi (32)) applied the consequent theory to the field of elementary particles.

If the new complex function $f(\ell,s)$ has a pole in the complex angular momentum plane (called a Regge pole) at $\ell = \alpha$, then in the neighbourhood of $\ell = \alpha$ the partial wave amplitude becomes

$$f(\ell,s) \approx \frac{\beta}{\ell-\alpha}$$

and since $f(\ell,s)$ depends on s, so do the pole position $\alpha = \alpha(s)$ and the pole residue $\beta = \beta(s)$. As the value of s increases

the pole moves in the complex $\ell$-plane giving rise to a trajectory $\alpha = \alpha(s)$ known as a Regge trajectory. If the real part of $\alpha(s)$ passes through a non-negative integer n at an energy $s = s_n$ it gives rise to

i) a bound state if $s_n < s_{threshold}$

ii) a resonant state if $s_n > s_{threshold}$

A trajectory thus connects not only bound states of different angular momentum $\ell$, but possible resonances to each other and to the bound states. This is better seen on a Chew-Frautschi plot of $Re\alpha(n) \equiv \ell$ against s. Particles can lie on the same Regge trajectory only if they have the same set of quantum numbers except spin.

The concept of signature must be introduced due to exchange forces, where a Regge pole of even (odd) signature contributes only to a partial wave of even (odd) $\ell$. Thus an even (odd) signature Regge trajectory can only contain a particle of even (odd) $\ell$, that is there is a $\Delta\ell = 2$ spacing rule.

For nucleon resonances there seem to be 3 trajectories with at least two members

i) $N(938,1/2^+)$ - $N^*(1688,5/2^+)$

ii) $N^*(1518,3/2^-)$ - $N^*(2190,7/2^-)$

iii) $N^*(1236,3/2^+)$ - $N^*(1950,7/2^+)$

There are a few singlets, but extrapolation of the presumed trajectories predicts resonances (recurrencies) of higher and higher spins. Boson trajectories are not so firmly established.

There seems to be only two trajectories which 'might' have two particles on them

i) $\rho(765,1^-)$ - $g(1650,3^-)$

ii) $A_2(1300,2^+)$ - $S(1930,4^+)$

where g and S have been suggested by drawing trajectories through the $\rho$ and $A_2$ of the same slope ($\sim 1$ (Gev/c)$^{-2}$) as the fermion trajectories.

Experimental survey of the Regge pole model

The transition matrix element for a two body or quasi-two-body reaction is given assymptotically as

$$T(s,t,u) \approx \sum_i \left[\frac{s-u}{s_i}\right]^{\alpha_i(t)} . \beta_i(t) \frac{1 + e^{i\pi\alpha_i(t)}}{\sin\pi\alpha_i(t)}$$

where the sum is performed over all the relevant trajectories, and $s_i$ is a conveniently chosen normalisation mass.

From Regge pole theory the total cross sections are assymptotically constant if there is exchanged a pole of even signature having $\alpha(0) = 1$. This pole (the Pomeron) has the quantum numbers of the vacuum but is not a real particle since odd $\ell$ should correspond to odd signature.
In forward scattering the dominance of a single pole exchange gives a differential cross section which shrinks with energy

$$\frac{\delta\sigma}{\delta t} \approx F(t) \left[\frac{s}{s_o}\right]^{2\alpha(t)-2}$$

This agrees with pp scattering but not $\pi p$ and $\bar{p}p$. Thus it must be concluded that present energies are not high enough for one pole dominance.

The Regge pole model gives good fits (Phillips and Rarita (33)) for $\pi p$ scattering and total cross sections for multi-trajectory exchange. The energy dependence of $\pi^{\pm}p$ scattering comes directly from the model, and the dip in $\pi^{+}p$ backward scattering arises from the exchanged N and N* trajectories in the u channel, whereas $\pi^{-}p$ backward scattering can only exchange N*.

For the charge exchange process $\pi^{-}p \rightarrow \pi^{o}n$, where only $\rho$ exchange is allowed, the energy independent dip in the differential cross section is well reproduced.

For the quasi-two-body processes

$\pi^{-}p \rightarrow \eta^{o}n$ ($A_2$ trajectory exchanged)

$\pi^{-}p \rightarrow \pi^{o}N^{*++}$ ($\rho$ trajectory exchanged)

$\pi^{+}p \rightarrow K^{o}N^{*++}$ ($\rho$ and $A_2$ trajectories exchanged)

the differential cross sections are well fitted by the model.

It is evident that the Regge pole model can reproduce the energy dependence of the differential cross sections for vector meson exchange where the absorption model fails. However, the Regge pole model gives little information about angular correlations where the absorption model has been most successful.

# CHAPTER 2

## THE EXPERIMENTAL CONDITIONS OF THE EXPOSURES

Approximately 180,000 pictures of 11.5 Gev/c positive pions in the CERN 2m hydrogen bubble chamber were obtained in one exposure at the CERN proton synchrotron in July 1966 using the U3 beam. In two similar exposures in October 1964 and January 1965 300,000 pictures were obtained of 5 Gev/c positive pions in the British national hydrogen bubble chamber using the 02 beam. Throughout both runs the beams were operated by members of each collaboration and the author was one of the Durham group representatives in the 11.5 Gev/c exposure in 1966.

### 2.1 The layout of the U3 and 02 beams

The U3 and 02 beams were both constructed in the east experimental area of the CERN proton synchrotron to supply the respective chambers with reasonably pure beams of pions, kaons, and protons at different momenta up to about 20 Gev/c. The U3 beam contained to RF separators for mass analysis, these being more effective at the higher particle energies than electrostatic separators which were used in the 02 beam. For ease of operation all the beam collimators were remotely

adjustable and in order to reduce the contamination due to scattered particles all the vertical and horizontal images were separated. Both beams consisted of three separate stages. Firstly those particles lying within the correct momentum interval were selected. The second stage produced the mass analysis, and in the final stage the momentum was redefined and the beam shaped for entry into the respective chamber.

a) The U3 beam

The layout of the components of the 170m long beam is illustrated schematically in Fig.(4). The protons in the synchrotron, having reached a momentum of about 22 Gev/c, were extracted by fast ejection (bunch by bunch) onto a copper target (2×1×150mm). The angular acceptance of the secondary particles was defined by the product of the target area and the apertures of the horizontal and vertical collimators C1 and C2. The quadrupole lens system Q1-Q4 focussed the horizontal part of the beam into collimator C4, while bending magnets B1 and B2 produced a deflection of about 100mr with dispersion. Momentum analysis took place at C4 ('the momentum slit'), and collimator C3 defined the angular acceptance of the beam in the vertical plane.

Immediately behind the 'momentum slit' was a quadrupole Q5 and bending magnets B3 and B4 producing a deflection equal in size and direction to the first, removing scattering and dispersion from the beam. Thus after the second group of

FIG. 4

SCHEMATIC DIAGRAM OF $U_3$ BEAM LAYOUT

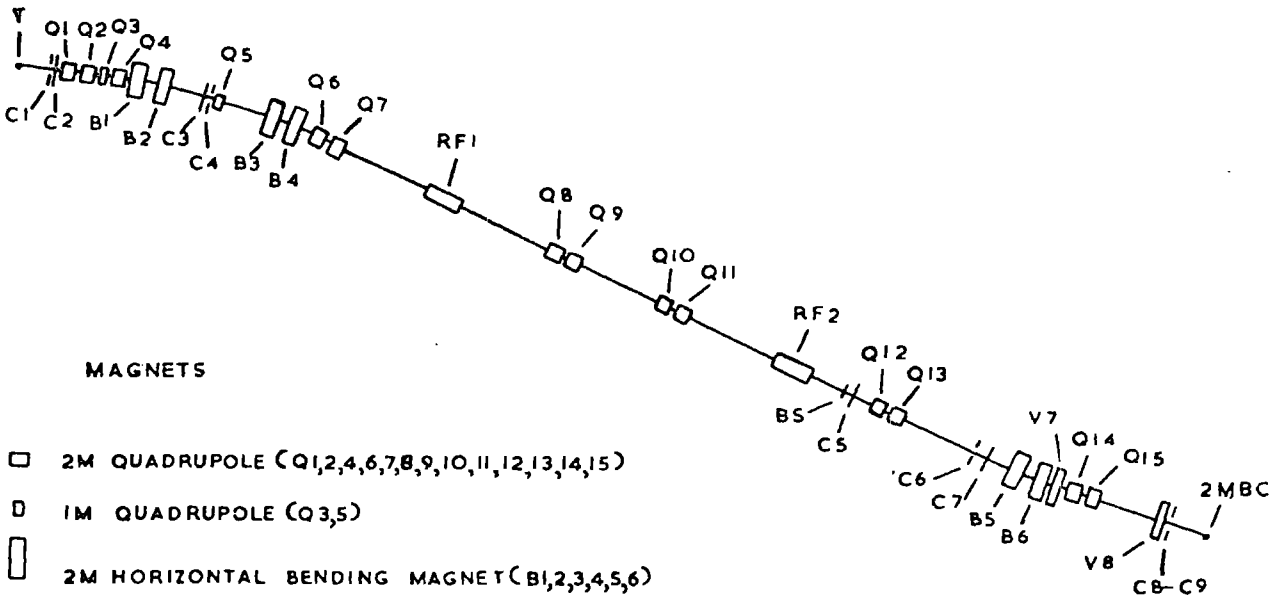


MAGNETS

- 2M QUADRUPOLE (Q1,2,4,6,7,8,9,10,11,12,13,14,15)
- 1M QUADRUPOLE (Q3,5)
- 2M HORIZONTAL BENDING MAGNET (B1,2,3,4,5,6)
- 1M VERTICAL BENDING MAGNET (V7,8)

COLLIMATORS

- HORIZONTAL COLLIMATOR (C1,4,6,8-9)
- VERTICAL COLLIMATOR (C2,3,5,7)
- BEAM STOPPER (BS)

SEPARATORS

- RADIOFREQUENCY SEPARATOR (RF1,2)

T = TARGET

BC = BUBBLE CHAMBER

magnets there was a monochromatic beam to ±0.2% (neglecting chromatic aberation) without dispersion.

A doublet Q6-Q7 gave a vertical image of the target and a horizontal image of the 'momentum slit' in the centre of the first RF cavity RF1. The two doublets Q8-Q9 and Q10-Q11, symmetrically placed in the space between RF1 and RF2, produced horizontal and vertical images in RF2, after which the wanted and unwanted particles were separated. The beam stopper BS, which was placed at the image of C3, stopped the unwanted particles. Following the beam stopper was a collimator C5 which limited the vertical part of the beam and reduced the muon contamination.

The doublet Q12-Q13 produced a horizontal and vertical image in the centres of collimators C6 and C7 so redefining the beam before the final momentum analysis. The momentum redefinition stage consisted of a 100mr deflection by bending magnets B5 and B6 and the focussing of the horizontal part of the beam into the collimators C8 and C9 by the quadrupoles Q14 and Q15, which also produced a parallel beam in the vertical plane. The two vertical magnets V7 and V8 defined the vertical acceptance of the beam and shaped it for entry into the chamber.

b) <u>The 02 beam</u>

The layout of the 180m long beam is shown in Fig.(5). When the protons in the synchrotron had reached a momentum of

FIG. 5

## SCHEMATIC DIAGRAM OF $O_2$ BEAM LAYOUT

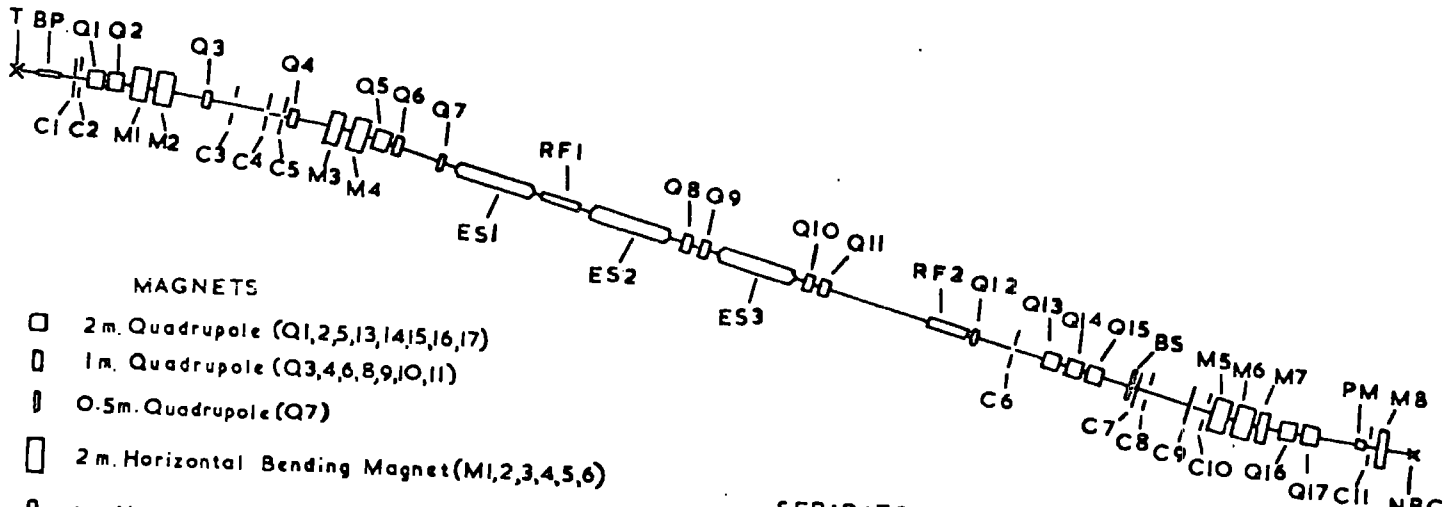


MAGNETS

- 2 m. Quadrupole (Q1,2,5,13,14,15,16,17)
- 1 m. Quadrupole (Q3,4,6,8,9,10,11)
- 0.5m. Quadrupole (Q7)
- 2 m. Horizontal Bending Magnet (M1,2,3,4,5,6)
- 1m. Vertical Bending Magnet (M7,8)
- 1m. Pulsed Vertical Bending Magnet (PM)

SEPARATORS

- Electrostatic Separator (ES1,2,3)
- Radiofrequency Separator (RF1,2)

COLLIMATORS

- Horizontal Collimator (C2,3,8,10,11)
- Vertical Collimator (C1,4,5,6,7,9)
- Beam Stopper (BS)

T = Target

NBC = Bubble Chamber

20-25 Gev/c (intensity $\sim 5 \times 10^{11}$ protons/pulse) a beryllium target (0.5x2x80mm) was placed in the beam for approximately 1ms. The secondary particles produced were extracted at an angle of $5 \cdot 1^{o}$ through an iron pipe BP, which protected them from the field of the following magnet in the synchrotron ring.

The 02 beam was very similar in operation to the U3 beam except that instead of two RF separators three electrostatic separators were used in the mass analysis stage. These had a plate length of 9m, a gap of 10cm, and an electric field of 50 Kv/cm. More collimators were used for definition and two extra bending magnets M7 and M8 were incorporated for steering the lower energy beam into the chamber. An extra quadrupole doublet Q16-Q17 and sweeping magnet PM were used to produce divergence and spread in the beam on entry into the chamber.

## 2.2 Running the U3 and 02 beams

The numbers of secondary particles from the targets of both beams were monitored continuously by counters and proportional values displayed in binary form. The fluctuations observed were mainly due to variations in the proton beam intensities. Checks on the number and distribution of tracks in the chambers necessitated adjustments of the collimator apertures and vertical magnets to maintain an average of about 15 particles entering the chambers.

The currents in the bending magnets and the voltages in the separators were monitored and regularly checked. The values in the U3 beam remained very stable requiring little resetting. However, reports from the 02 beam run showed that there was instability in the voltages of the electrostatic separators necessitating retuning of the mass analysis stage from time to time.

2.3 The U3 and 02 beam momenta

The momentum of the 02 pion beam was determined (D.J. Schotanus. Nijmegen 1965) by taking a sample of unambiguous four-prong events and processing them through the THRESH-GRIND kinematic reconstruction programme which fitted the beam momentum. From a plotted distribution the average value was

$$4.990 \pm 0.006 \text{ Gev/c}$$

after corrections for the magnetic field. A similar determination (H.Nagle. Hamburg 1968) of the U3 pion beam momentum gave

$$11.53 \pm 0.02 \text{ Gev/c}$$

Measured values of the beam momenta gave widths of at least 100 Mev/c due to multiple scattering and measurement errors. Consequently it was necessary to take a weighted average in the programme GRIND between the known values of the beam momenta and the measured values in order to reduce the

effects of these errors. The measured value is required to determine the angle of the beam in the chamber.

## 2.4 Muon contamination in the beams

The author has made calculations of the muon contaminations assuming that the muons come from decay pions after the mass slits (C6 in the 02 beam, the beam stopper in the U3 beam). Taking into account the 'bites' of the momentum redefinition stages, the apertures of the last collimators, the isotropic decay of pions in their rest system, and the fact that any muons diverging by more than ~1cm from the other tracks along the length of the chamber could be eliminated.

Calculations give for the muon contamination in the U3 beam a value of

$$0.05 \pm 0.5\%$$

For the 02 beam the value is

$$1.5 \pm 0.5\%$$

At the momentum of 11.5 Gev/c the two RF separators in the U3 beam could be tuned to reject both protons and kaons. Pions and other particles were not rejected, consequently it is possible that the hadron contamination might have been 1-2% (P. Layzeras 1969) allowing the possibility of deuteron contamination in the beam, the importance of which will be seen in Chapter 5.

## 2.5 The CERN 2m hydrogen bubble chamber

### a) General construction

The chamber consisted of a single aluminium casting with an internal clear section of dimensions 200×51×60cm. This clear section was closed at the front and back by plane glass windows 171mm thick of good optical quality glass and protected by a hydrogen cold tank. The whole was enclosed in a stainless steel vacuum tank to reduce heat losses. Fig.(6) shows a plan view of the chamber construction.

The chamber was filled with about 1000 litres of liquid para-hydrogen which was kept at a temperature of 27° Kelvin and under a pressure of approximately 6 atmospheres.

### b) The magnetic field

Surrounding the vacuum tank was a large electromagnet producing a near uniform magnetic field over the liquid chamber volume. This field has been mapped (G. Petrucci 1963) by measuring the field over a 3-dimensional matrix with respect to the central field value. With a nominal current in the magnetic windings of 1000 amperes the induction at the centre of the chamber was 17.385 kilogauss, with a deviation of no more than 3% at the extremities. The values of the percentage variations were tabulated and used in the kinematic reconstruction programmes.

FIG.6

2 METRE C.E.R.N. BUBBLE CHAMBER (HORIZONTAL SECTION)

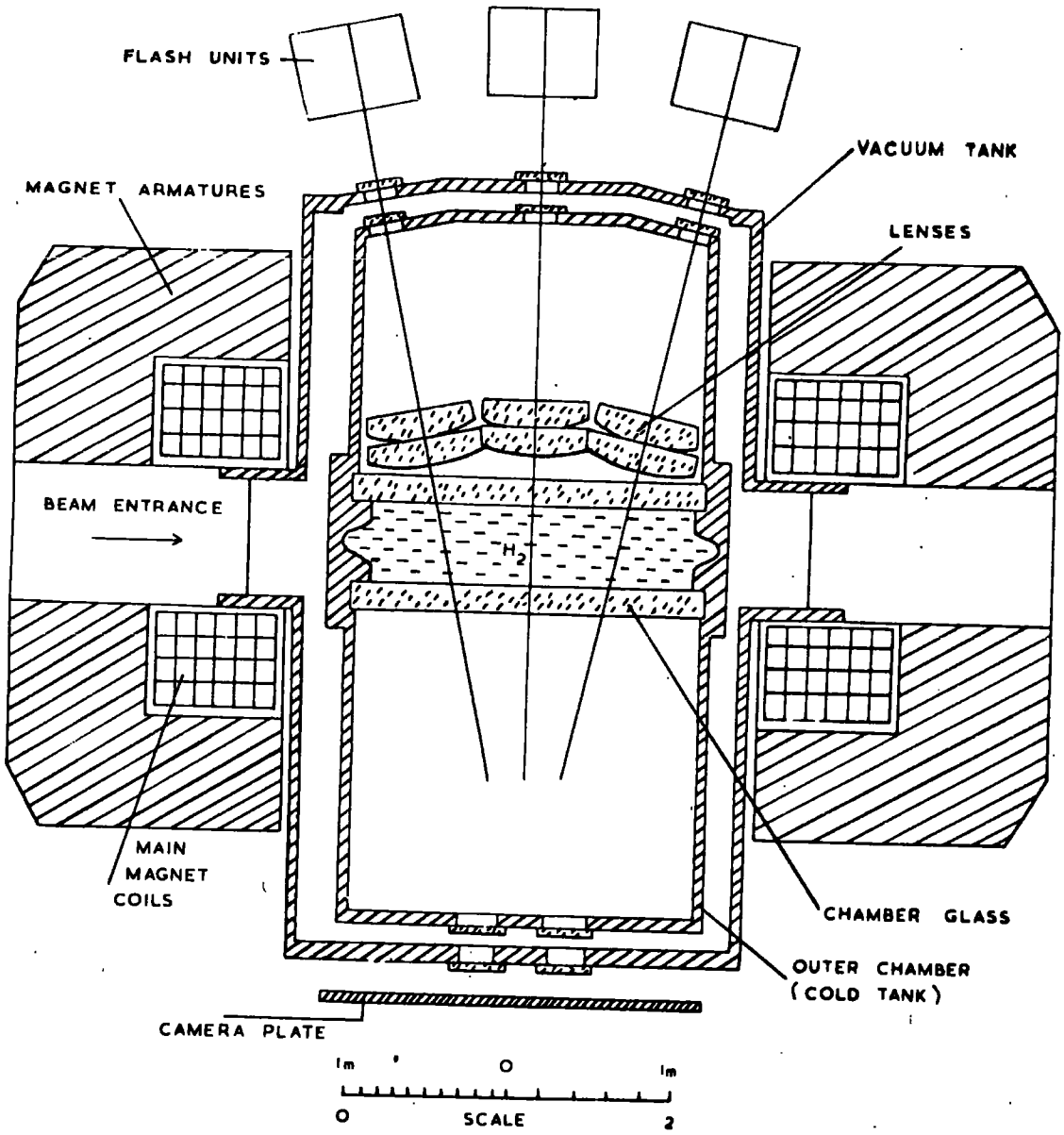

c) The illumination and photographic system

The CERN 2m chamber used the 'through illumination' system with three condensors supplied by neon flash tubes using monochromatic filters. The duration of the light flash was 200$\mu$s. The four camera objectives were mounted on the same baseplate in a diamond array with their axes perpendicular to the chamber windows as shown in Fig.(7A). The focal lengths averaged 182·3mm with aperture f/32, the distance between the principal plane (object side) and the reference plane (inside surface of front chamber window) was 243cm, and the camera-plate and the film plane were parallel to ±0·5mr. Each camera saw through a set of three small windows, one in the cold tank and two in the vacuum tank, of total thickness 7·55cm. They were so arranged that the light deviation was no more than 0·15mr.

The camera film used was unperforated 50mm in 300m lengths containing 1500 frames. Later this was halved to give rolls of 750 frames suitable for the measuring machines.

## 2.6 The British national hydrogen bubble chamber

a) General construction

The British national bubble chamber was similar in construction to the CERN chamber except that the clear section was 152x50x46cm closed on either side by 155mm high quality glass windows. The chamber held some 500 litres of hydrogen

FIG. 7

A. CAMERA CONFIGURATION OF THE 2 METRE CERN BUBBLE CHAMBER

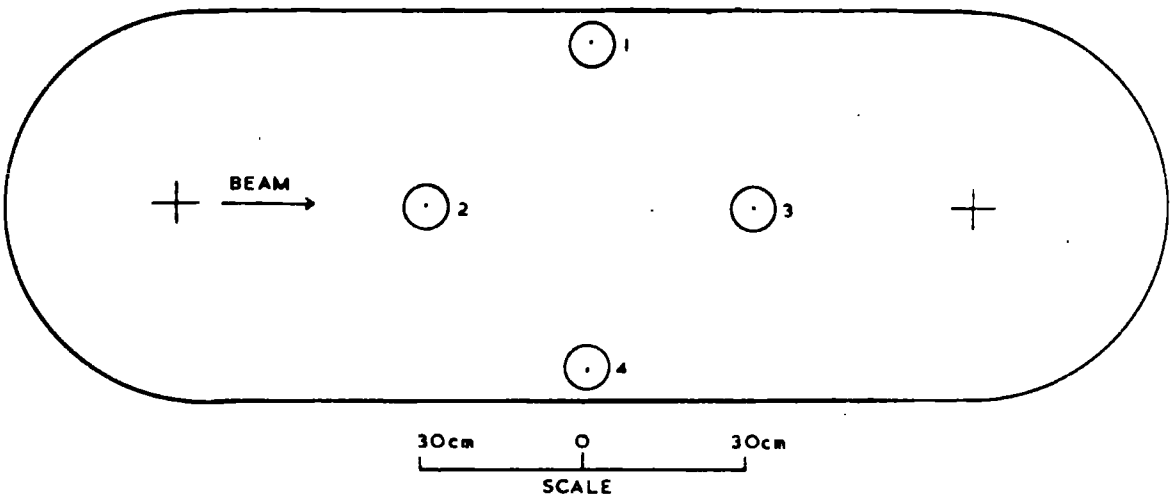


B. CAMERA CONFIGURATION OF THE BRITISH NATIONAL BUBBLE CHAMBER

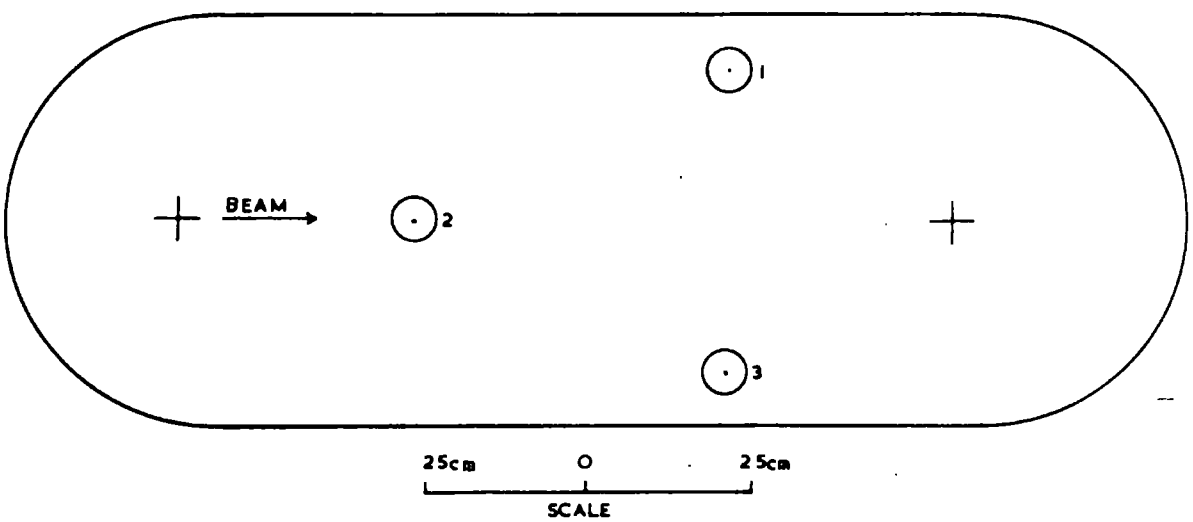

enclosed by a hydrogen tank and vacuum tank (Fig.(8)).

b) The magnetic field

The electromagnet of the British chamber produced an induction of 13.46 kilogauss with an excitation current of 10,000 amperes. The field was mapped (33) and showed a variation over the chamber of no more than 3%.

c) The illumination and photographic system

The British chamber also used the through illumination system with three monochromatic flash tubes. However, only three cameras were used set in a triangular array as shown in Fig.(7B) with average focal length of 82mm, aperture f/32, and used 35mm unperforated film containing 2500 frames. The distance from the chamber reference plane to the camera nodal points was on average 174.6cm and the thicknesses of the windows in the hydrogen and vacuum tanks were 25.5mm and 16.0mm respectively.

2.7 Operation cycle of the chambers

A signal from the proton synchrotron triggered the expansion valves of the chamber causing the pressure at the surface of the liquid (~6.5 atmospheres) to fall rapidly in 10ms to ~2.8 atmospheres. The liquid then became superheated and boiling commenced in areas of high charge density. The latter were provided by the arrival of the beam at the beginning of this superheated sensitive period. A scintillation counter in the

FIG. 8 PLAN VIEW OF B.N.H.B.C. SHOWING OPTICAL SYSTEM AND MAGNET.

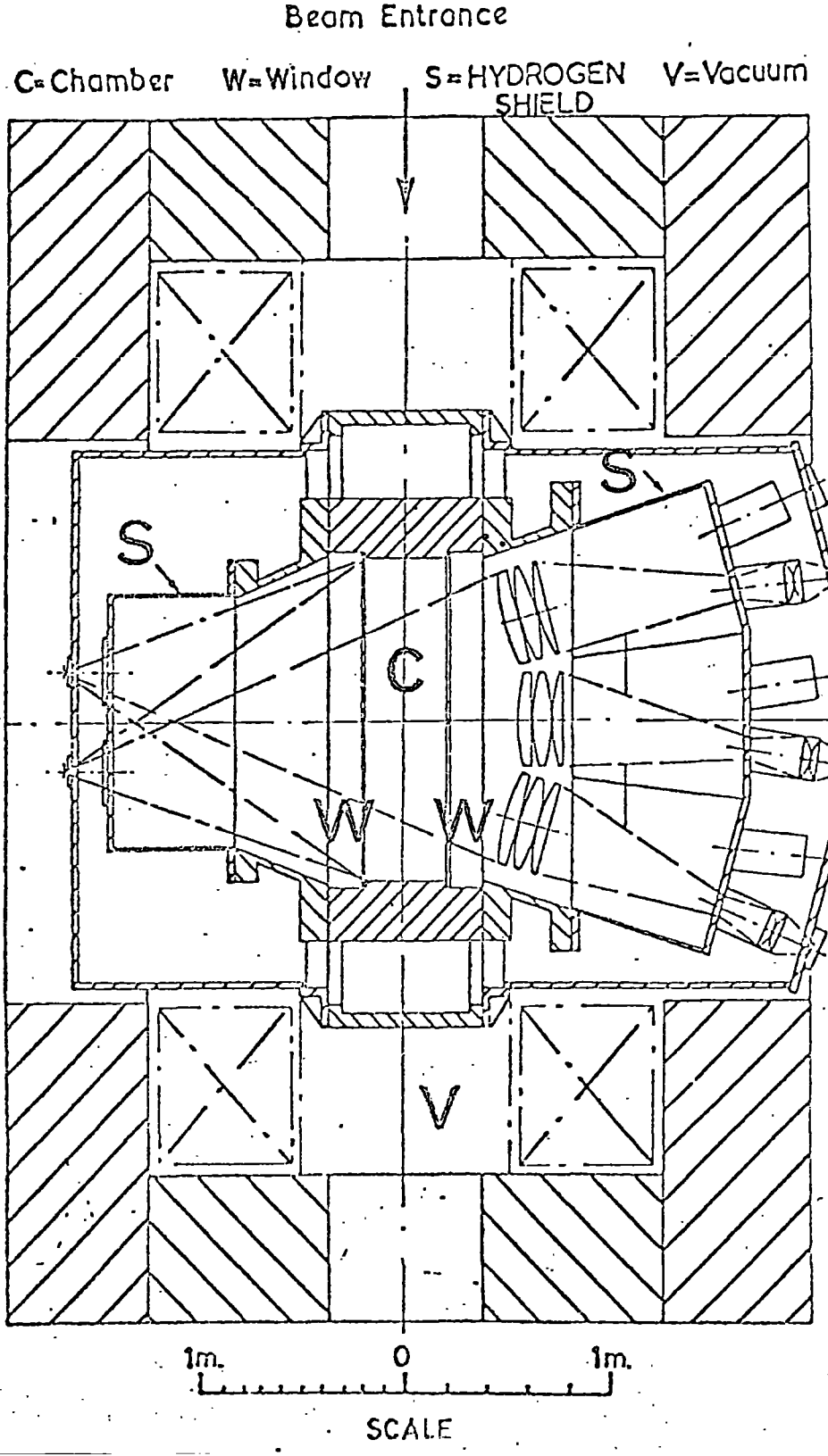

beam triggered the neon flash tubes about 1·5ms later giving the bubbles time to grow to a suitable size of ~200$\mu$. The 2ms sensitive time was followed by the recompression stage which took about 10ms. However, a further 100ms were required for the liquid turbulence to cease.

The films in the cassettes were automatically wound forward and the cycle repeated every 2 seconds.

## 2.8 Picture layout and chamber reference systems

In addition to the beam tracks and interactions on each frame there was superimposed an image of the data box containing information such as the serial number of the expansion and the date of the experiment.

The reference systems used in event reconstruction were provided by a set of fiducial crosses etched into the surfaces of the chamber windows. There were also two crosses etched into the metal of the camera gates which provided the only co-ordinate system independent of the distortions of the camera objectives.

## 2.9 Picture quality during the exposures

In order to keep a continual check on the quality of the pictures as they were taken a few frames were removed from the end of each roll and developed soon after their exposure. The bubble density of the beam tracks was determined by counting the gaps between bubbles with a low powered microscope.

This density was required to be 10-12 bubbles/cm and could be adjusted by altering the 2ms sensitive time with respect to the beam arrival. By adjusting the time of the flashes it was possible to maintain a correct bubble size of ~200$\mu$.

The collimators at the ends of the beams were adjusted to give 10-15 tracks per frame, and the quadrupoles adjusted to give proper shaping of the beam.

2.10 Rejection of films from the exposures

Following the observation of the Milan group that, in scanning the 11·5 Gev/c film, there appeared some instability in the relative positions of the fiducial marks between frames, and a report from the 2m bubble chamber crew that in the early part of the run the film suffered from poor seating in the cameras, the author and colleagues decided to investigate the quality of the film in more detail.

a) Measurements

The method followed was that described by Fleury, Shephard, and Vanderhaghen (34). In each film the positions of the fiducial marks 1-12 on the back of the front chamber window (Fig.(9)) were measured on each of 20 frames uniformly distributed throughout each of 12 films initially available to the Durham group. Measurements were made on the 3 views used in the kinematical reconstruction of events (cameras 1, 3, and 4). The setting error of the measuring machines and measurers was

FIG. 9

CONFIGURATION OF FIDUCIAL CROSSES

ON THE REAR OF THE FRONT GLASS OF THE

CERN 2M CHAMBER

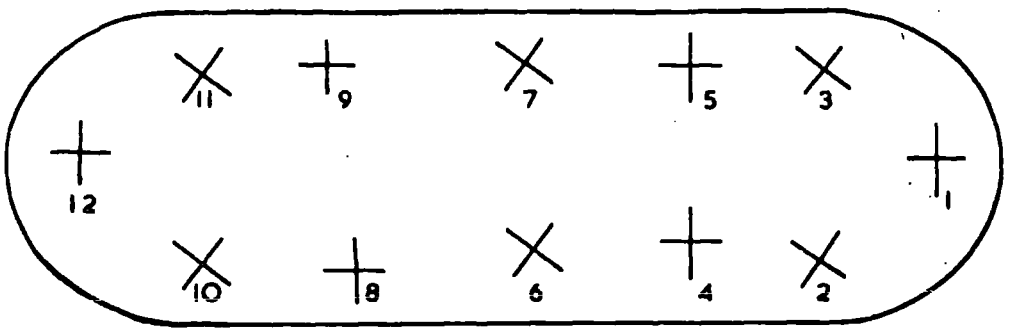


SELECTED LENGTHS

| LENGTH | DISTANCE BETWEEN CROSSES | |
|---|---|---|
| 1 | 1 | 2 |
| 2 | 1 | 3 |
| 3 | 1 | 12 |
| 4 | 2 | 3 |
| 5 | 2 | 6 |
| 6 | 3 | 7 |
| 7 | 4 | 5 |
| 8 | 4 | 6 |
| 9 | 5 | 7 |
| 10 | 6 | 7 |
| 11 | 6 | 8 |
| 12 | 6 | 10 |
| 13 | 7 | 9 |
| 14 | 7 | 11 |
| 15 | 8 | 9 |
| 16 | 10 | 11 |
| 17 | 10 | 12 |
| 18 | 11 | 12 |

SELECTED ORTHOGONAL RATIOS

| | | | | | | | | | | |
|---|---|---|---|---|---|---|---|---|---|---|
| $14/16$ | $3/7$ | $3/10$ | $3/15$ | $3/16$ | $12/16$ | $11/18$ | $14/10$ | $12/10$ | $5/7$ | $7/9$ |

determined from repeated settings on the same fiducial mark in a frame. The standard deviation of these settings was 2 IEP units (A IEP unit is 2·5$\mu$) and was the same for 3 measurers.

b) Analysis and results

Eighteen inter-fiducial distances and from them eleven orthogonal ratios (Fig.(9)) were determined from the measurements by means of a programme written by the author. The comparison of these orthogonal ratios is probably the best way of detecting any distortion of the film. Fiducial mark 3 was not clearly visible and was subject to large setting errors, consequently it was not used in any of the calculations.

The standard deviation of all ratios in each film was determined and divided by the expected standard deviation calculated from the setting error. This quantity $\sigma$(observed)/$\sigma$(expected), which is in fact the ratio of the observed width of the distribution of an orthogonal ratio to that expected, should be unity under perfect film conditions. It soon became apparent that the two films in the poor seating region possessed by Durham suffered from distortions as $\sigma$(observed)/$\sigma$(expected) was much greater than unity for all ratios, whereas the other films gave values close to unity.

Fig.(10) shows $\sigma$(observed)/$\sigma$(expected) for all ratios in all films for each of the 3 cameras. The cross hatching is for all ratios in the two badly affected films. Camera 3 seems to have suffered less from poor seating than the other two. This

FIG. 10

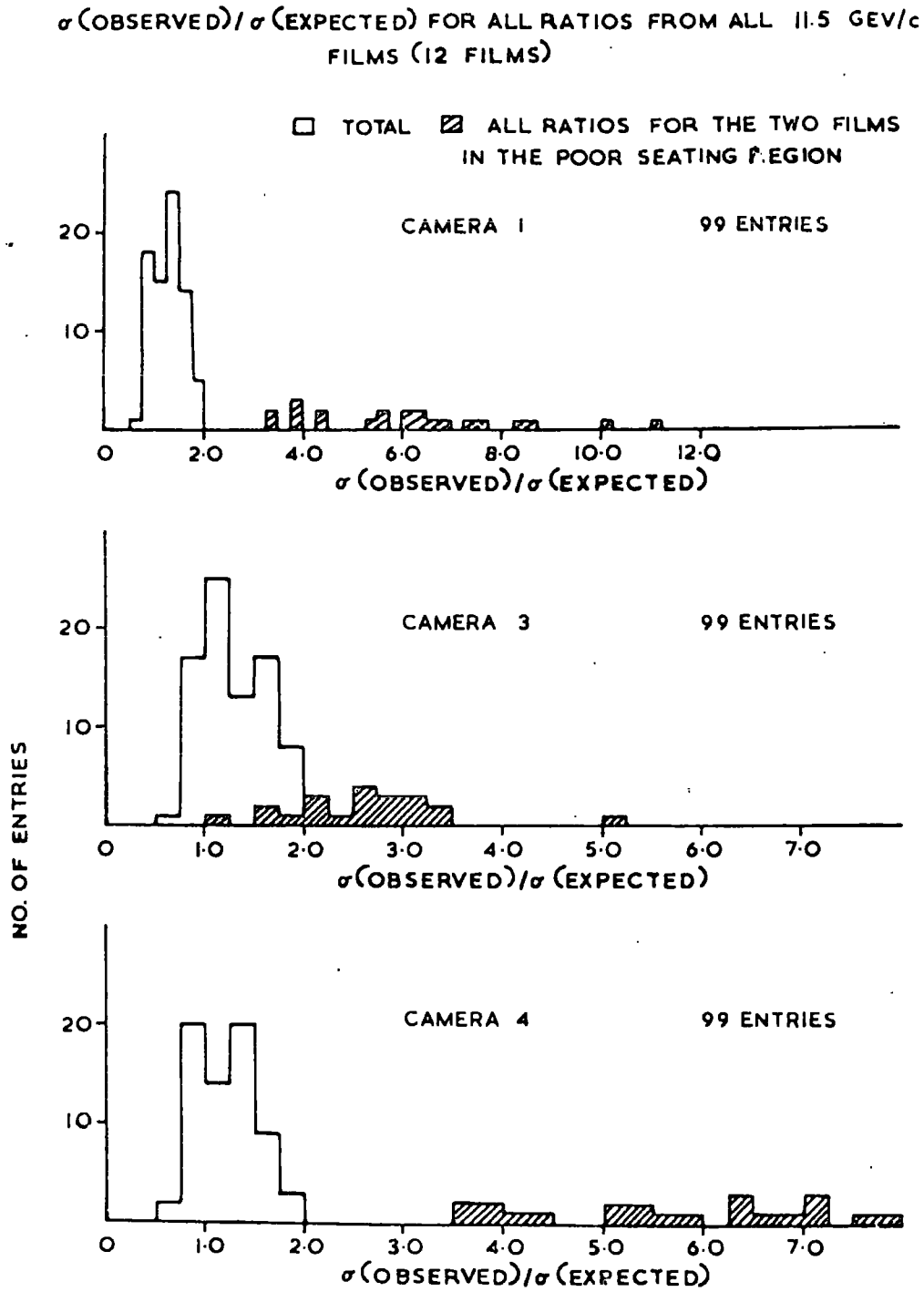
σ (OBSERVED)/σ (EXPECTED) FOR ALL RATIOS FROM ALL 11.5 GEV/c FILMS (12 FILMS)
TOTAL
ALL RATIOS FOR THE TWO FILMS IN THE POOR SEATING REGION
CAMERA 1
99 ENTRIES
CAMERA 3
99 ENTRIES
CAMERA 4
99 ENTRIES
NO. OF ENTRIES
σ (OBSERVED)/σ (EXPECTED)

is difficult to understand since each camera was served by the same vacuum. At best the distributions for the other two cameras correspond to a standard deviation in the setting error of ~30$\mu$ instead of the expected 5$\mu$.

Also it can be seen that the distribution of orthogonal ratios for the good films is about 30% broader than expected ($\sigma$(observed)/$\sigma$(expected) $\approx$ 1.3). This could be due to an underestimation of the setting error which might have deteriorated in a long series of measurements, or to a smaller degree of poor seating.

The 5 Gev/c film was investigated in the same way by the Durham group in 1965 (35). Of the films taken in October 1964 all were found to suffer from poor seating and had to be rejected. Consequently only the 150,000 pictures taken in February 1965 were analysed as these were found to be free from such defects.

## 2.11 Optical distortions in the chambers

The optical distortions present in the experimental arrangements of the chambers and cameras had to be illiminated before events within the chambers could be reconstructed. The sources of distortion were from film tilt, non-alignment of the lens mechanical axis with the optic axis, and from distortions within the lens itself. The chamber windows also added to the distortion through tilting and being slightly wedge shaped. Fig.(11) shows a schematic diagram of general chamber

FIG. 11

## SCHEMATIC DIAGRAM OF CHAMBER OPTICS

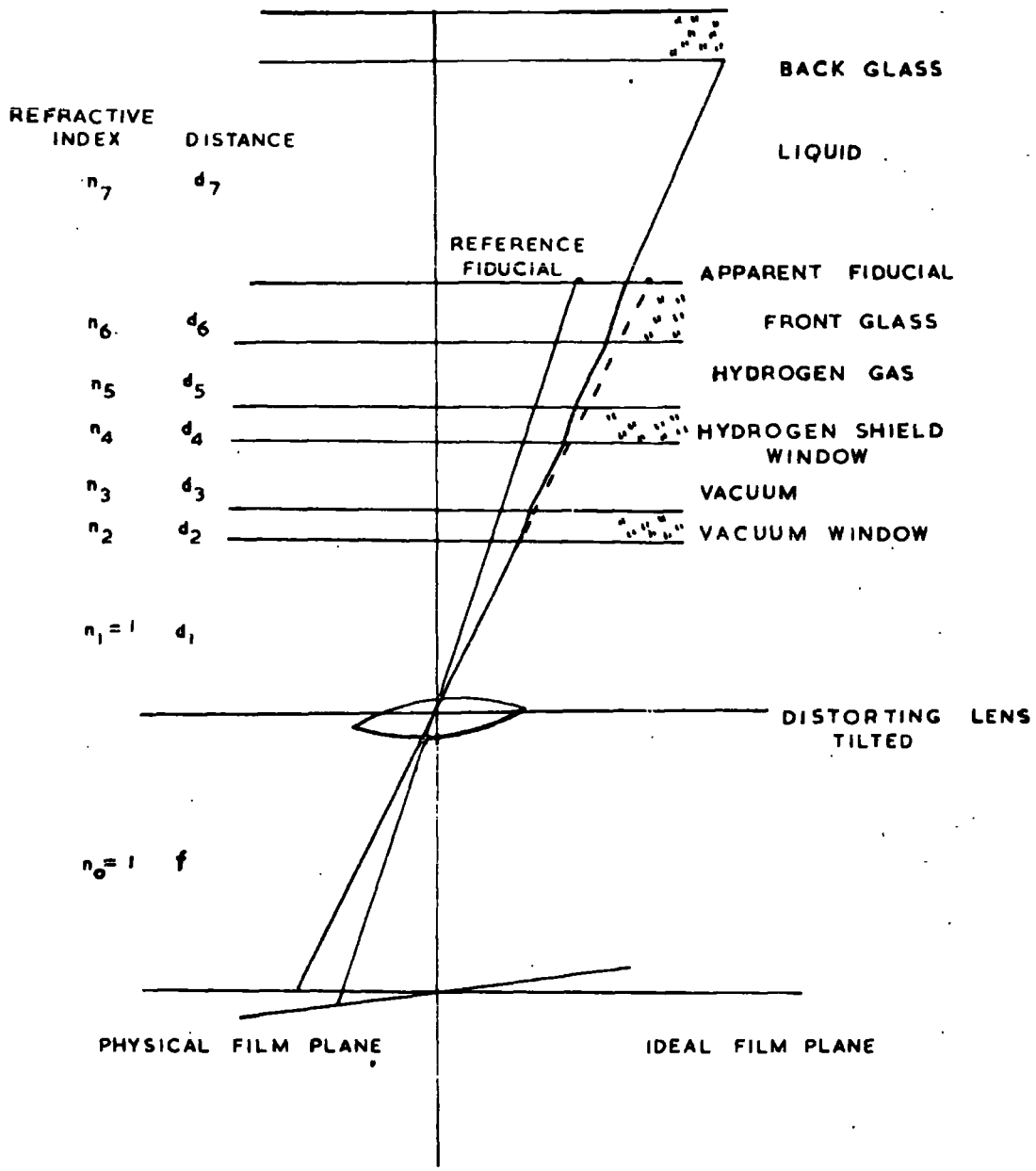

optics.

The CERN TC programme PYTHON was used to correct for the distortions which, by means of an iterative procedure, uses IEP measurements of fiducial marks to compute increasingly more accurate values for the distortion coefficients, the optic axis parameters, and the camera positions. It is assumed that the positions of the fiducials on the chamber planes, the depth of the chamber, and the refractive index of hydrogen are accurately known, and that all the other parameters are approximately known.

The distortion coefficients $\beta_i$ are expressed in the form of a transformation S between the co-ordinates of the physical film plane (the IEP measurements when the effect of film stretch has been illiminated) and those of the ideal film plane (G. Kellner 1965)

$$S = 1 + \beta_1 \cdot \frac{x}{f} + \beta_2 \cdot \frac{y}{f} + \beta_3 \cdot \frac{xy}{f^2} + \beta_4 \cdot \frac{x^2}{f^2} + \beta_5 \cdot \frac{y^2}{f^2} + \beta_6 \cdot \frac{(x^2 + y^2)^2}{f^4}$$

$\beta_1$ and $\beta_2$ are the coefficients of the tilt angle, $\beta_3$, $\beta_4$, and $\beta_5$ are the coefficients of elliptical distortion (which might arise if the mechanical axis of the lens was not lined up with the optic axis), and $\beta_6$ measures higher order distortions.

The 11·5 Gev/c film fiducials were measured on a large number of pictures in Durham and PYTHON run at CERN. The 5 Gev/c film was treated in the same way by the Paris group. Both sets of parameters so determined were inserted into the titles of

the CERN TC geometrical reconstruction programme THRESH. With the distortion coefficients in the titles the number of fitting iterations required to reconstruct tracks was 2 or 3 as opposed to 4 or 5 without the coefficients.

2.12 Films taken without the magnetic field

Approximately 200 pictures were taken of the British chamber with the magnetic field removed in order to investigate track distortions in the chamber apart from measurement errors and multiple scattering which are taken account of in the programme THRESH. There was in fact a residual field of about 4 gauss, but this would give a negligable curvature to the 5 Gev/c beam tracks.

About 100 tracks, with a length more than 40cm, were measured and processed by THRESH. The distribution of $1/\rho$, although consistent with measurement and multiple scattering errors, had a mean value significantly different from zero

$$\frac{1}{\rho} = +0{\cdot}7 \pm 0{\cdot}2 \times 10^{-5} \text{ cm}^{-1}$$

giving a maximum detectable momentum of about 580 Gev/c. This value is in opposite sense to the $1/\rho$ for the beam tracks and so positive track measurements are underestimated by about 50 Mev/c.

Some no-field film was taken in a recent exposure with the U3 beam and the 2m chamber although unfortunately none were

taken in the first run in 1966. Preliminary results suggest a reduction in the momentum of positive tracks of about 70 Mev/c, which gives a residual curvature of

$$\frac{1}{\rho} = +0.3 \pm 0.1 \times 10^{-5} \text{ cm}^{-1}$$

and a maximum detectable momentum of about 1750 Gev/c.

The residual curvature is a systematic error attributed to the distortion of the hydrogen during expansion. The kinematic reconstruction programme GRIND however uses a weighted average of the measured and known beam momentum so that the distortion could be ignored. The error on the secondary tracks would be covered by the fitting procedure of GRIND although this could lead to a bias in the $\chi^2$ distributions.

# CHAPTER 3

## SELECTION AND RECONSTRUCTION OF EVENTS

This chapter is concerned with the processes of scanning, measuring, and computation necessary to find and analyse events that had taken place within the bubble chambers. Generally the processes were identical for the 11·5 Gev/c and 5 Gev/c films. The stages of analysis are shown schematically in Fig.(12), and are fairly standard in all bubble chamber groups.

The films were scanned twice, check scanned, and every interaction found fully documented. The measurements were made on the three Durham IEP machines and the co-ordinate measurements ordered by the programme REAP. Geometrical reconstruction of the events was performed with the programme THRESH, and the kinematics and possible interpretations of the topology of the events were determined by GRIND. The most probable event topologies were then selected and a full summary of the dynamics of the events prepared with the programme SLICE. The required distributions of various quantities were obtained from this summary by means of statistics programmes written by the author.

### 3.1 Scanning

Durham's share of the 5 Gev/c film (25 rolls) and 11·5

FIG. 12

FLOW DIAGRAM OF THE ANALYSIS OF EVENTS

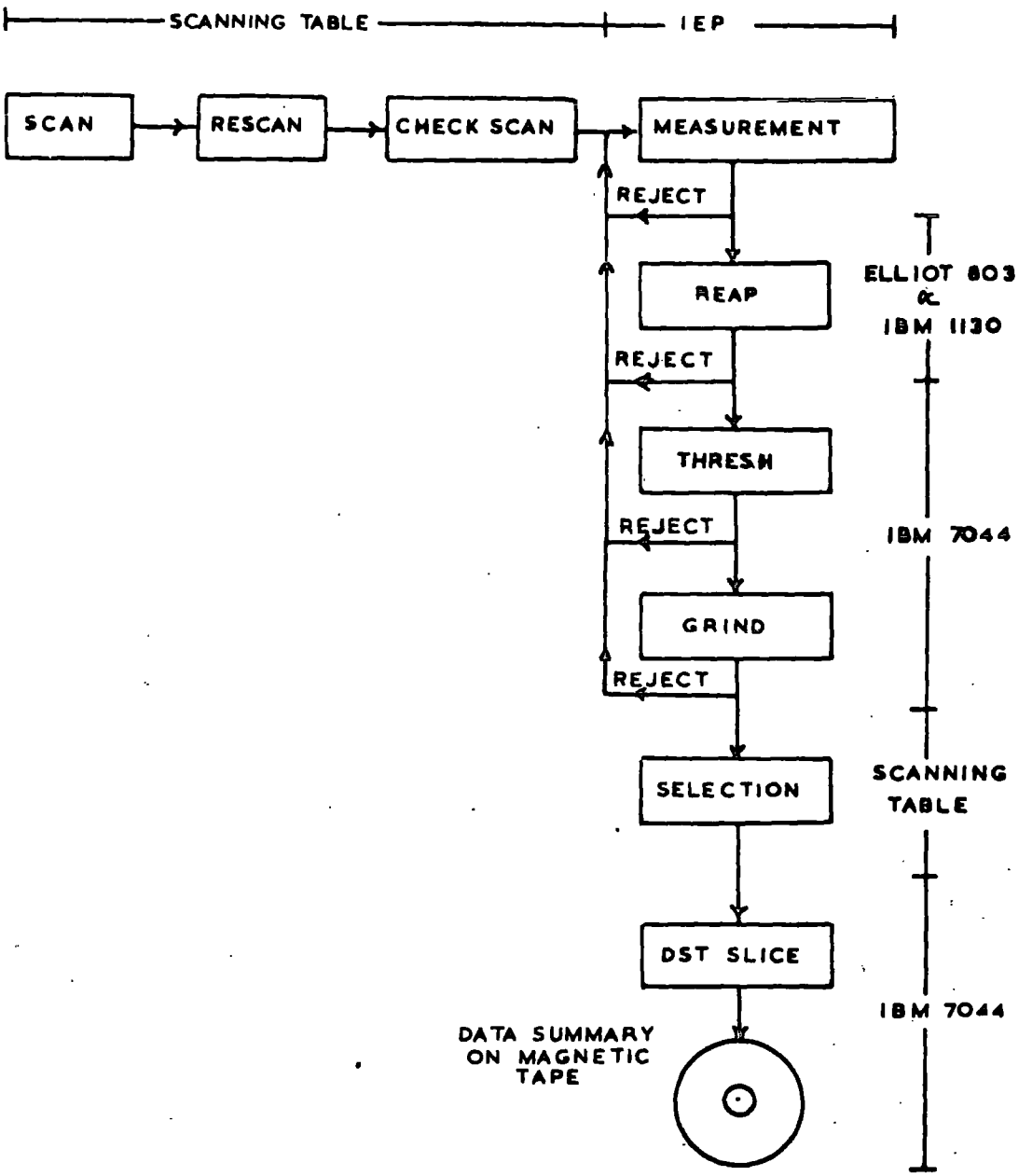

Gev/c (24 rolls) film was scanned on two Prevost machines designed to project images of the three films from the cameras onto a horizontal table with a magnification of ~14x. Two of the images overlapped for ease of reference where stopping or dipping tracks were concerned.

The fiducial volumes for the two types of film are shown in Fig.(13), camera 2 being used for the 5 Gev/c film and camera 3 for the 11.5 Gev/c film. Any interaction occurring within these volumes was recorded, including the number of secondary tracks, strange particles and electron pairs, secondary decays and interactions, and stopping tracks.

For the 5 Gev/c film the primary track was required to enter the fiducial volume within the intervals 3,4,5, and 6 and to interact within the vertical projections of these intervals. 11.5 Gev/c interactions were required to be within vertical lines drawn between the back chamber fiducials. The vertical and horizontal limitations ensured that there was sufficient beam and secondary track length so as to make accurate reconstruction and momentum determination possible.

Rejection of frames was necessary where the illumination was poor or the tracks too faint. Furthermore, frames were rejected if there were less than 4 or greater than 25 tracks. In the former case because it was difficult to be certain which were good beam tracks, and in the latter because of difficulty in distinguishing interactions. Finally, an interaction was

FIG. 13

A. DIAGRAM OF FIDUCIAL VOLUME IN THE 2 METRE CERN BUBBLE CHAMBER

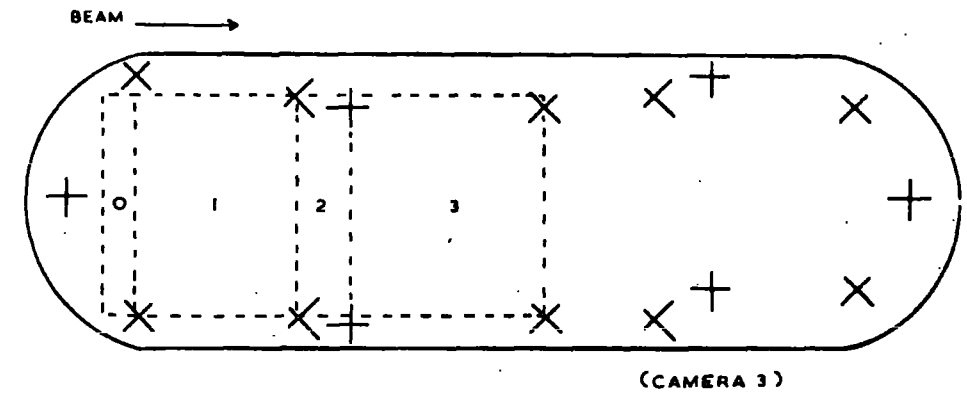


FRONT GLASS FIDUCIALS

REAR GLASS MEASURED FIDUCIALS

B. DIAGRAM OF FIDUCIAL VOLUME IN THE BRITISH NATIONAL BUBBLE CHAMBER

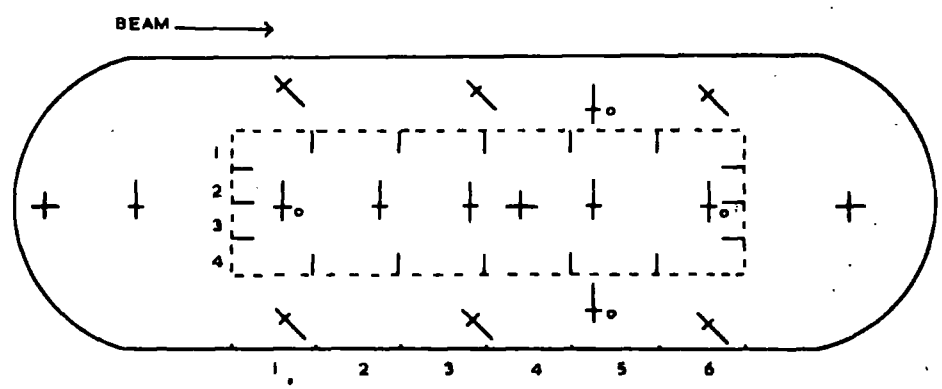


FRONT GLASS FIDUCIALS

REAR GLASS FIDUCIALS

MEASURED FIDUCIALS

rejected, rather subjectively, if the beam track appeared to deviate from other tracks judged to be parallel.

Two independent scans were performed for each film and then a check-scan, supervised by a physicist, to check differences between the first two scans. These could include missed events, mis-classifications, and wrongly identified strange particles or electron pairs. From the number of events found in the first scan but not in the second, and vice-versa, the scanning efficiency could be estimated assuming that events were missed randomly and that the efficiency of a scanner remained constant (Burhop 1962). These assumptions are justified for 4,6,8, and 10 pronged events which are relatively easy to see, but not necessarily for elastic events where the visibility depends on the momentum and angle of the recoil proton. Special corrections were made later for unseen elastic scatterings.

## 3.2 Measurement of events

The three views of the 11·5 and 5 Gev/c two pronged events, without associated $V^o$'s, were measured on the three Durham object plane digitized machines, two of which utilise a Moiré fringe optical digitization system and the third (a Coventry Gauge and Tool machine) a mechanical digitization system. The x and y co-ordinates of points measured are punched out onto paper tape for input to the sorting programme REAP.

a) Mechanical operation

The three camera films are clamped by spring loaded glass plates on to an aluminium plate (the x substage) which has a central glass section (20x20cm) and can be driven in the x direction by means of DC motors operated from the keyboard. The lamp and condenser are mounted above and below the x substage respectively forming the y substage which can be similarly driven independently of the x substage. The film spools are mounted on the main machine and wound forward or backward by AC motors operated from the keyboard. Any non-orthogonality of the substage axes is taken account of in the programme THRESH.

b) Optical system

On all machines the films are projected with a magnification of ~15x onto a screen by a mirror mounted below the y substage. The screen is a sandwich of ethulon between glass plates (80x40cm) producing a fine grain and a high quality picture. Co-ordinate measurements are made by driving the substages in order to bring the film image into coincidence with a 'dot' (about the size of a bubble) marked on the image side of the screen. By using object plane digitization optical distortions are avoided since all measurements are made near to the optic axis.

c) Digitization

i) Moiré fringe machines

The system consists of two linear gratings, one the length of the substage movement fixed to the main machine, and the other a circular grating housed in a Ferranti mounting on the moving substage. Both gratings have 125 lines/mm and are separated by ~75μ. Adjustment of the angle between the gratings produces an interference fringe pattern broader and more separated than the gratings moving at right angles to the direction of the gratings. A Ferranti 'four-splitter' lens projects four parts of the fringe pattern on to four photoelectric cells. One fringe corresponds to ~2·5μ and defines the maximum possible measuring accuracy.

The outputs from the photocells are taken in pairs in antiphase, amplified, shaped, and fed to a 17 bit bi-directional binary counter (Fig.(14)). By operation of the '/' character on an IBM typewriter the contents of the counters are transferred by a parallel read system, by way of a shift register buffer store containing 6 words of 6 bits length, to the paper tape punch which puches out the x and y co-ordinates as shown in Fig.(15). The contents of the binary counters are displayed for the operator to check correct counting.

ii) Mechanical digitization (Coventry machine)

The system consists of a Hilger and Watts mechanical digitizer for the x and y motion which has a coded drum attached to the machine drive shaft. Shaft rotation is converted

FIG. 14

BLOCK DIAGRAM OF MOIRÉ FRINGE DIGITIZATION

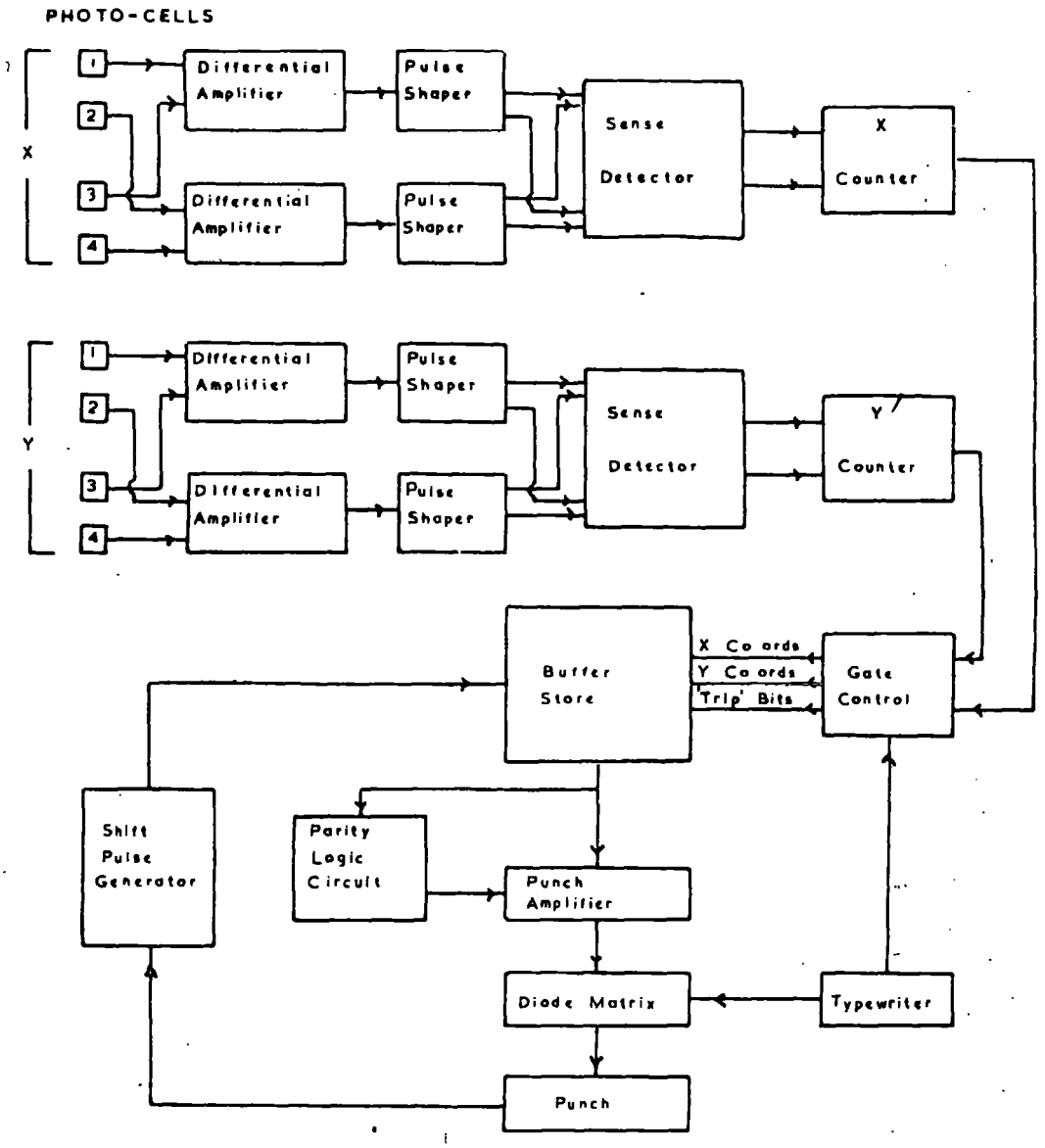

FIG. 15

SYSTEM OF CO-ORDINATE PUNCHING ON MOIRÉ FRINGE MACHINES

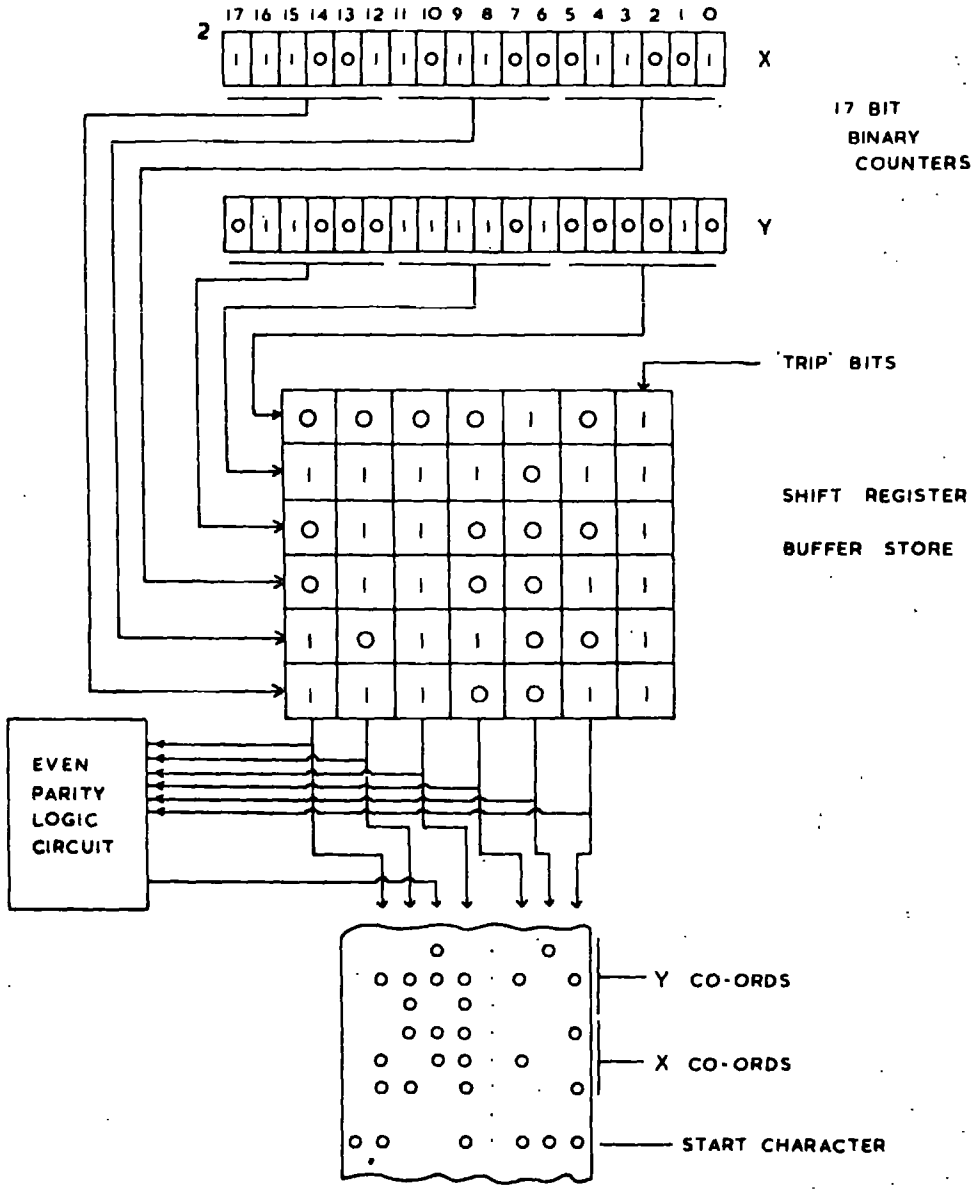


PAPER TAPE CO-ORDINATE CHARACTERS

into a number of discrete steps by coding the drum into conducting and non-conducting segments sampled by brush contacts, four to each of five bands on the drum representing the decades $10^0$-$10^4$. The coding used is Hilger and Watts reflected decimal which is shown in Fig.(16), and has the advantage that in moving from one digit to another only one segment changes and so no ambiguity arises in the count due to the brushes not being perfectly aligned. The maximum measuring accuracy is one segment corresponding to $\sim 2 \cdot 5 \mu$.

The brush contacts on each of the five decades are parallel fed to a non-bridge uniselector, five banks for the x co-ordinate and five for the y (Fig.(17)). The '/' character on the IBM typewriter advances the uniselector one step and the punching out of the x and y co-ordinates begins. The format of the co-ordinates is shown in Fig.(16).

d) Operator measurement

At the beginning of each two pronged event the operator punched the event number, topology, measurer number, and date onto the paper tape. For each view an identification label was punched and the x and y binary counters set at $2^{16}$ on some convenient point such as the apex of the event or a nearby bubble. Four fiducials (Fig.(13)), the apex of the event, and 9 points per track were measured, all being prefixed by a REAP programme identification character (eg. A9 for the beam track). For identified stopping tracks the end point was also measured, the

FIG. 16

SCHEMATIC DIAGRAM OF CO-ORDINATE PUNCHING ON THE COVENTRY MACHINE

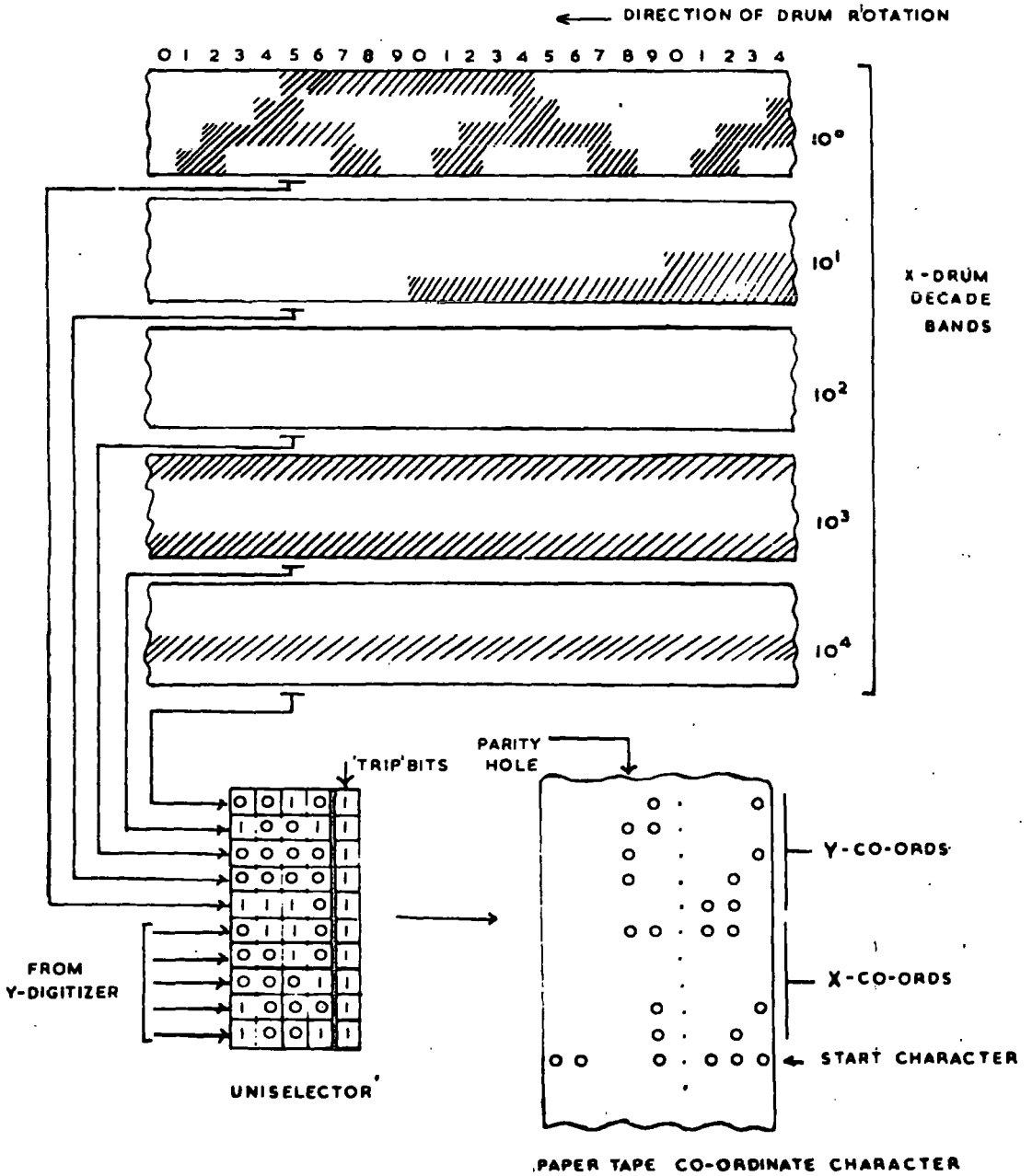

FIG. 17

BLOCK DIAGRAM OF MECHANICAL DIGITISATION

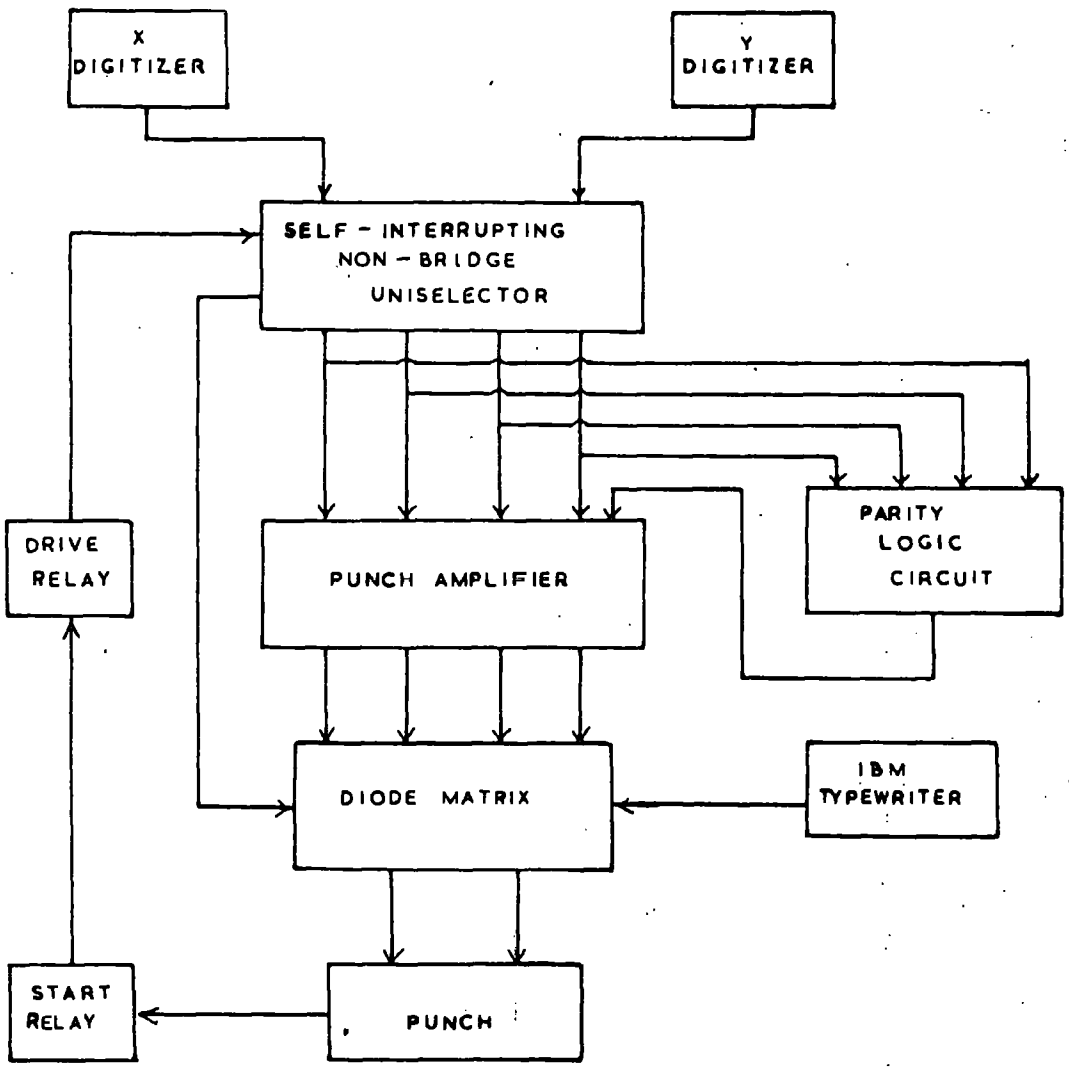

momentum being determined in GRIND from the range-energy relations. Only the first part of highly curved tracks was measured as the geometry programme THRESH which was used does not take energy loss into account.

At the end of each view the operator checked the original setting to see if there had been any shift or mis-count in the digitizers. If so the view was remeasured. The standard deviation of points measured on the film plane was 5-8$\mu$ depending upon the operator and the amount of care taken.

## 3.3 Reap

The programme REAP was written for the Durham computer for the purpose of sorting the information on the measuring machine paper tapes into a predetermined format suitable for input to THRESH, disregarding any redundant information and any errors. REAP also checks that a minimum number of fiducials, tracks, and points have been measured, and will return an event for remeasurement if these numbers should be insufficient.
During operation it is possible, if desired, for REAP to make the following checks on the quality of measurement

i) Ratios of inter-fiducial distances can be calculated and should remain constant to ~0.2%

ii) A least squares fit of the form $y = ax^2+bx+c$ can be made to tracks and the divergence of individual points should be less than about 10$\mu$ on the film.

These checks provide a quick test of the quality of the

measurement and the performance of the machines. However, care has to be taken in the case of stopping tracks where appreciable energy is lost, the curvature changes, and consequently a fit is artificially poor.

## 3.4 Thresh

THRESH is a geometry programme of the CERN TC library and was used in its mass independent form on the IBM 7044 computer at Glasgow university. Its purpose is to reconstruct events in chamber space and to find point and track parameters from a maximum of four stereoscopic views using the film measurements output from REAP.

The raw film measurements are transformed onto the 'physical film plane' (Fig.(11)) by means of the measured fiducial marks, the chamber co-ordinates of which are given in the THRESH title block FIDUC. The transformation is assumed to be linear thus correcting automatically for magnification, non-orthogonality of the measuring axes, and film shrinkage. If the fiducials are badly measured a view will be rejected. Distortions are removed by using the polynomial of section (2.11), the coefficients $\beta_i$ being in the THRESH titles after their determination from PYTHON.

Points are reconstructed in chamber space from all three views used by means of the intersection of optical paths reconstructed back to the cameras. The necessary information to do this such as camera positions and refractive indices of

intermediate media are contained in the titles. Bad convergence of these reconstruction lines could lead to a view or the whole point reconstruction being abandoned.
On completion of the reconstruction a first approximation to a helix is made of the form

$$x = \rho(\cos\theta - 1)$$

$$y = \rho\sin\theta$$

$$z = \rho\theta\tan\alpha$$

where $\rho$ is the radius of the helix and $\alpha$ is the dip angle. A final least squares fit to a helix finds small corrections to $\rho$ and $\tan\alpha$ so that reconstruction lines corresponding to all measurements in all views and the parametric equations of the helix are simultaneously satisfied at the optimum. Normally two or three iterations are required to make a fit.

The output from THRESH is on magnetic tape in the format required for input to GRIND containing the co-ordinates of the apex and stopping points, radii of curvature, dip and azimuth angles, and the measured length of tracks, all with the appropriate errors.

## 3.5 Grind

GRIND is a programme of the CERN TC library and was also used on the IBM 7044 in Glasgow. Its purpose is to propose, for each event, possible particle hypotheses using the geometry output from THRESH and experimental parameters supplied by the

programmer in the title blocks. Each hypothesis is tested by a statistical fit to the given data and the results of the fit such as the momenta and angles of the tracks and the probability of the fit are output onto magnetic tape along with the associated errors.

A complete description of an event must satisfy the four constraint equations of energy and momentum at the vertex

$$\sum P_x = \sum_{i}^{n}(P_i \cos\lambda_i \cos\phi_i) - P\cos\lambda\cos\phi \rightarrow 0$$

$$\sum P_y = \sum_{i}^{n}(P_i \cos\lambda_i \sin\phi_i) - P\cos\lambda\sin\phi \rightarrow 0$$

$$\sum P_z = \sum_{i}^{n}(P_i \sin\lambda_i) - P\sin\lambda \rightarrow 0$$

$$\sum E = \sum_{i}^{n}(\sqrt{P_i^2+m_i^2}) - (\sqrt{P^2+m^2}+M) \rightarrow 0$$

$P,\lambda,\phi$, and m are the momentum, dip, azimuth, and mass of the beam. $P_i,\lambda_i,\phi_i$, and $m_i$ are the corresponding values for the outgoing particle i, and M is the target mass. The track momenta are determined from the curvatures using the magnetic field matrix in the titles, or if stopping, from the range energy relations in the titles.

A least squares fitting procedure computes corrections to be made in order to reduce $\sum P_x, \sum P_y, \sum P_z$, and $\sum E$ to values below that given in the titles (0.0005 Gev) and to minimise $\chi^2$ which is given by

$$\chi^2 = \frac{(X_i - \bar{X}_i)^2}{X_i^2}$$

where $\bar{X}_i$ is the measured quantity and $X_i$ the fitted quantity. The $\chi^2$ probability must be greater than the value specified in the titles (0·1%), and the number of steps required must be less than the value given in the titles (15 steps).

With no neutral particle in the final state all the variables are constrained, there are four degrees of freedom and the fit is called a '4C-fit'. When a neutral particle is missing (with assigned mass) the first three equations are used to solve for P,$\lambda$, and $\phi$, leaving the fourth equation for a constraint. There is only one degree of freedom and the fit is called a '1C-fit'. When more than one particle is missing there are more unknowns than constraint equations and a fit cannot be made. A fit will fail if there is non-convergence of the constraint equations, too many unmeasured or missing variables, too many iterations, or the probability is less than that defined in the titles.

## 3.6 Error flags for tracks in THRESH and GRIND

The 'internal errors' on each track for $1/\rho$,$\lambda$, and $\phi$ are calculated by the programmes during the fitting procedures. The severity of these errors is judged by comparing them with a set of 'external errors' calculated on a track with an average measuring error, $f_o$, on the projected sagitta. $f_o$ is related to the standard error on measurement and was set at 100$\mu$ in the titles.

If the internal errors are more than three times the external

errors on 1/ρ, , and o the error words 100, 40, and 20 are flagged against the appropriate track. In addition, the error word 200 is flagged should three times the external error on 1/ρ be greater than 1/ρ itself. The important errors from THRESH are 1000, when there is non-convergence in the helix fit, and 4000 or above when there is complete failure. The latter may be due to an insufficient number of points to perform a first approximation to a helix or not enough views available.

## 3.7 Event rejection

For every event passing through GRIND it was necessary to judge from the above error flags whether to accept it as a well reconstructed event or to reject it for re-measurement. The criteria used in both the 5 and 11.5 Gev/c experiments are shown in Table (1).

TABLE 1

| Error flags on tracks | Action |
|---|---|
| 100, 40, 20 | Not serious unless on more than 2 tracks. |
| 120 (100+20)<br>140 (100+40)<br>160 (100+40+20) | Not serious if the momentum <400 Mev/c or the dip >60°, otherwise re-measure. |
| 200 | Not serious on beam tracks or short stopping tracks: otherwise re-measure. |
| 1000 | Same conditions as for the flags 160, 140, and 120. |
| 4000 and above | Re-measure |

## 3.8 Hypothesis selection

In general more than one hypothesis was well fitted for each event and it was necessary to examine the events in order to establish the correct hypothesis, or at least reduce the number of ambiguities. This was done by returning the film to the scanning table and looking at each event for indications that would make track identification possible. These include secondary interactions, decays, and the bubble density of the tracks. The latter is the number of bubbles per unit length normalised to minimum ionisation (beam tracks). For $\beta \lesssim 0.9$ the energy loss due to ionisation, and hence the bubble density D, is proportional to $1/\beta^2$, which becomes

$$D \propto 1 + \frac{m^2}{P^2}$$

where m is the assigned mass and P the momentum. For each track GRIND computes the projected bubble density $D/\cos\lambda$ ($\lambda$ is the dip angle) for the protons, kaons, and pions. Fig.(18) is a plot of the bubble density against momentum for the three particles where $\lambda$ is less than $30^{\circ}$.

In principle one can identify the tracks from the bubble density and so select the correct hypothesis. However, it can be seen that above 1300 Mev/c the difference in bubble density between protons and pions becomes less than 0.4, and unless the film is of good quality it is impossible to distinguish between them. In addition, when the momentum is less than about 150 Mev/c the

FIG. 18

BUBBLE DENSITY VS. MOMENTUM

PROTON, KAON, AND PION TRACKS.

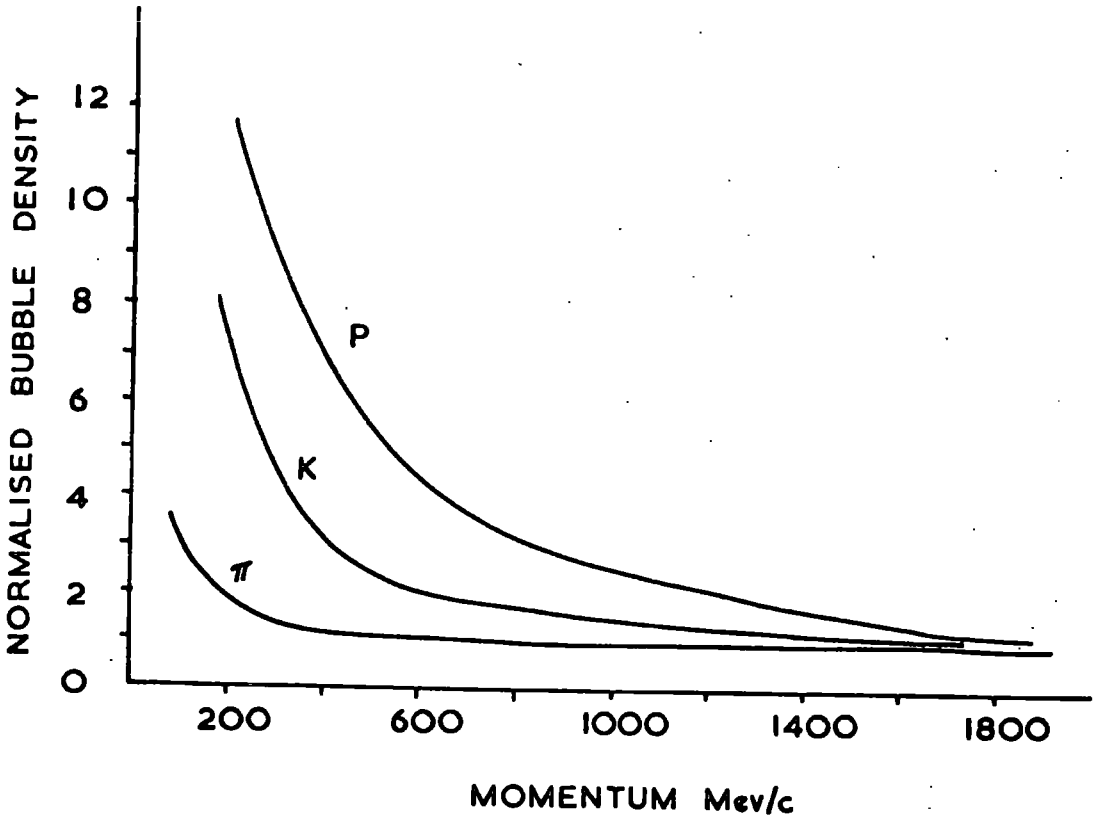

bubble density for all particles rises above saturation point (4-5) and it becomes impossible to distinguish particles unless they stop (from the range) or decay. Occassionally with highly dipping tracks the light was scattered and the tracks looked faint rather than darker. Consequently in cases where the dip was greater than $60^{o}$ a definite decision was not made.

Each succesful event from GRIND was given a code number made up of the following track identifications

2 (definite proton)

1 (possible proton)

0 (not a proton)

All hypotheses compatible with the decided coding were accepted, and events where all hypotheses were rejected recorded as no-fits.

## 3.9 The data summary tape (DST)

The CERN TC programme SLICE and a DST programme written by the author were used to prepare data summary tapes from the GRIND output. The DST contained the selected events and hypotheses and a reduced amount of dynamical information such as momenta, angles, energies, and effective mass combinations. Using the ionisation codes the possible no-fit hypotheses were also generated. The possible reaction channels entered on the two prong DST's are shown in Table (2).

TABLE 2

| No. of constraints | Reaction channel |
|---|---|
| 4 | $\pi^+p \rightarrow \pi^+p$ |
| 1 | $\pi^+p \rightarrow \pi^+p\pi^o$<br>$\pi^+p \rightarrow \pi^+\pi^+n$ |
| 0 | $\pi^+p \rightarrow \pi^+p\pi^o(m\pi^o)$ $m\geq 1$<br>$\pi^+p \rightarrow \pi^+\pi^+n(m\pi^o)$ $m\geq 1$ |

Apart from chi-squared cuts in SLICE of less than 24 (4 constraint fit) and less than 6 (1 constraint fit) in the 5 Gev/c experiment the only data restrictions applied at this stage were compatibility tests on the missing mass squared ($MM^2$) as follows

1C $\pi^o$ channel - $MM^2-2\Delta MM^2 < M^2(\pi^o)$

1C n channel - $MM^2-2\Delta MM^2 < M^2(n)$

no-fits

0C $\pi^o$ channel - $MM^2+2\Delta MM^2 > M^2(2\pi^o)$

0C n channel - $MM^2+2\Delta MM^2 > M^2(n+\pi^o)$

Any no fit failing the missing mass squared restrictions became an unclassified event and was rejected. In order to reduce the number of no fit ambiguities any track with a momentum greater than 4 Gev/c was considered not to be a proton.

## 3.10 Data analysis programmes

The data presented in this thesis was compiled in Durham using the IBM 360 computer at Newcastle university and programmes written by the author to produce histograms, Dalitz plots, Chew Low plots, and Peyrou plots from the DST tapes.

# CHAPTER 4

## TECHNICAL DATA AND TOPOLOGICAL CROSS SECTIONS

### 4.1 Scanning (Durham data)

The scanning results of the 24 rolls of film from the 11·5 Gev/c exposure are shown in Table (3). 1850 frames were rejected due to poor visibility or because there were less than 4 or more than 25 tracks per frame.

TABLE 3

11.5 Gev/c scanning data

| Prong size | Number of events found | Scanning efficiency | Corrected number of events |
|---|---|---|---|
| 2 | 6431 | .992 | 6482 |
| 4 | 6796 | .998 | 6809 |
| 6 | 2810 | .999 | 2813 |
| 8 | 476 | .999 | 476 |
| 10 | 39 | 1.0 | 39 |
| | | Total | 16619 |

Of the 25 5 Gev/c rolls of film exposed 6 were rejected initially due to poor visibility. Only 15 of the remaining 19 rolls were scanned the results of which are shown in Table (4). 1810 frames were rejected for the same reasons as in the 11·5 Gev/c

film.

TABLE 4

5 Gev/c scanning data

| Prong size | Number of events found | Scanning efficiency | Corrected number of events |
|---|---|---|---|
| 2 | 6668 | .991 | 6728 |
| 4 | 5057 | .997 | 5072 |
| 6 | 627 | .998 | 628 |
| 8 | 11 | 1.0 | 11 |
| | | Total | 12439 |

## 4.2 Measurement (Durham data)

All the two pronged events found in the scans were measured except for those with associated $V^o$'s, close secondary interactions or decays where the track length was too short to make accurate reconstruction possible, or where the visibility was too poor. In both experiments one remeasurement was made on events rejected under the criteria of section (3.7). The results of the measurement are shown in Table (5).

TABLE 5

Measurement of the two pronged events

| Experiment | Total number of events | Immeasurable or with $V^o$ | Number measured | Successful in GRIND | Pass rate |
|---|---|---|---|---|---|
| 11·5 Gev/c | 6431 | 471 | 5960 | 5136 | .862 |
| 5 Gev/c | 6668 | 473 | 6195 | 4043 | .653 |

The low GRIND pass rate in the 5 Gev/c experiment was due to the general poor quality of the whole film.

## 4.3 Topological cross sections

The topological cross sections were determined from the scanning data by each laboratory in each experiment. The Durham preliminary data is shown in Table (6).

TABLE 6

Durham cross section data

| Experiment | Scanning length(cm) | Number of tracks/frame | Total track length($cm \times 10^7$) | Total number of events |
|---|---|---|---|---|
| 11·5 Gev/c | 83·0 ±1·5 | 15·0 ±0·1 | 1·89 ±0·05 | 17470 |
| 5 Gev/c | 72·0 ±1·5 | 11·8 ±0·1 | 1·31 ±0·04 | 13025 |

The scanning lengths were determined from distributions of the x co-ordinates of the vertices of events. The dip and curvature of the beam tracks were ignored as they were found to give contributions to the lengths much less than the errors already present. The average numbers of tracks per frame were found by counting the number of tracks every tenth frame during scanning. The total track lengths given in Table (6) have been corrected for muon contamination and interactions in the chambers. The corrections were ~4% for the 11·5 Gev/c experiment and ~8% for the 5 Gev/c experiment. The latter includes a 4% correction for beam tracks going out of the side of the scanning volume

due to the higher curvature.

In addition to the corrections above the total numbers of events have been corrected for the number of two pronged elastic events not detected in scanning due to the momentum and direction of the recoil proton. The principle employed by each laboratory to make the correction was the same as that described in section (5.2). The corrections to the Durham two prongs were ~13% and ~9% in the 11·5 Gev/c and 5 Gev/c experiments respectively.

The hydrogen density used was 0·0624 g/cm$^3$ which, although having negligable variation with pressure, has a variation with temperature of about 3% per degree. This uncertainty has been allowed for in the calculated cross sections which are shown in Tables (7) and (8) for each laboratory in each experiment.

TABLE 7

11·5 Gev/c cross sections (mb)

| Lab. | 2 prong | 4 prong | 6 prong | 8 prong | 10 prong | Total |
|---|---|---|---|---|---|---|
| Durham | 10·3 | 9·6 | 4·0 | 0·7 | 0·05 | 24·9 |
| Saclay | 10·5 | 9·4 | 4·0 | 0·6 | 0·04 | 24·5 |
| Milano | 10·6 | 9·9 | 4·0 | 0·7 | 0·05 | 25.4 |
| Hamburg | 10·1 | 9·9 | 4·2 | 0·7 | 0·08 | 25.0 |
| Genoa | 10·2 | 9·6 | 4·3 | 0·8 | 0·06 | 24·9 |
| Total | 10·3±0·5 | 9·7±0·5 | 4·1±0·3 | 0·7±0·1 | 0·06±0·02 | 24·9±0·7 |

TABLE 8

5 Gev/c cross sections (mb)

| Lab. | 2 prong | 4 prong | 6 prong | 8 prong | Total |
|---|---|---|---|---|---|
| Bonn | 14·3 | 10·2 | 1·4 | 0·03 | 25·9 |
| Durham | 14·9 | 10·4 | 1·3 | 0·03 | 26·6 |
| Nijmegen | 14·4 | 10·4 | 1·3 | 0·04 | 26·1 |
| Paris* | 15·7 | 9·6 | 2·3 | 0·03 | 27·6 |
| Turin | 14·9 | 10·2 | 1·3 | 0·03 | 26·4 |
| Total | 14·8±0·5 | 10·2±0·5 | 1·5±0·3 | 0·03±0·01 | 26·5±0·7 |

* Approximate values only available from Paris.

The individual cross sections for each laboratory agree very well, and the total cross sections are in good agreement with the counter cross sections of 24·6 ±0·1mb at 11·49 Gev/c (36) and 26·67 ±0·01mb at 4·96 Gev/c (37).

## 4.4 Ambiguous fits on the DST's

Tables (9) and (10) show the numbers of events fitted successfully by one or more reactions (hypotheses) for each laboratory in each experiment. The variation in the percentages between laboratories can be explained in terms of the different measuring accuracies and the different criteria used in judging the identification of tracks from ionisation. However, no significant biases should be introduced because of this.

It is to be noted that there is a large discrepency between Durham and the other laboratories in the 11·5 Gev/c experiment with respect to unambiguous events belonging to reaction A. This is partly due to the different numbers of events not seen because of small angle scatterings, but mainly due to the fact that the other laboratories only accepted reaction A fits, irrespective of ambiguities, in events where the tracks could be definitely identified. This was done in the knowledge that

TABLE 9

Ambiguities on the 11·5 Gev/c DST

| Reaction | Durham | Saclay | Milano | Genoa |
|---|---|---|---|---|
| A $\pi^+p \rightarrow \pi^+p$ | 1250-24·4% | 818-34·2% | 638-34·3% | 836-31·4% |
| B $\rightarrow \pi^+p\pi^o$ | 619-12·0% | 234- 9·8% | 207-11·2% | 312-11·8% |
| C $\rightarrow \pi^+\pi^+n$ | 218- 4·2% | 89- 3·7% | 92- 4·9% | 101- 3·8% |
| ambiguous A-B | 418- 8·2% | 99- 4·1% | 40- 2·1% | 38- 1·4% |
| ambiguous A-C | 25- 0·5% | 0- 0·0% | 2- 0·0% | 3- 0·0% |
| ambiguous A-B-C | 27- 0·5% | 0- 0·0% | 0- 0·0% | 0- 0·0% |
| ambiguous B-C | 141- 2·7% | 26- 1·1% | 10- 0·5% | 44- 1·7% |
| D $\pi^+p \rightarrow \pi^+p\pi^o(m\pi^o)m\geq 1$ | 1086-21·2% | 441-18·4% | 414-22·3% | 564-21·2% |
| E $\rightarrow \pi^+\pi^+n(m\pi^o)m\geq 1$ | 469- 9·1% | 321-13·4% | 83- 4·5% | 150- 5·6% |
| ambiguous D-E | 617-12·0% | 270-11·3% | 307-16·5% | 435-16·4% |
| unclassified | 266- 5·2% | 96- 4·0% | 67- 3·6% | 173- 6·5% |
| Total no. of events | 5136 | 2394 | 1860 | 2656 |

TABLE 10

Ambiguities on the 5 Gev/c DST

| Reaction | Durham | Nijmegen |
|---|---|---|
| A $\pi^+p \rightarrow \pi^+p$ | 1207-29·9% | 3158-31·7% |
| B $\rightarrow \pi^+p\pi^o$ | 580-14·3% | 1182-11·9% |
| C $\rightarrow \pi^+\pi^+n$ | 196- 4·8% | 554- 5·6% |
| ambiguous A-B | 135- 3·3% | 162- 1·6% |
| ambiguous A-C | 10- 0·2% | 0- 0·0% |
| ambiguous A-B-C | 8- 0·2% | 0- 0·0% |
| ambiguous B-C | 110- 2·7% | 203- 2·0% |
| D $\pi^+p \rightarrow \pi^+p\pi^o(m\pi^o)m\geq 1$ | 823-20·3% | 1764-17·7% |
| E $\rightarrow \pi^+\pi^+n(m\pi^o)m\geq 1$ | 197- 4·9% | 706- 7·1% |
| ambiguous D-E | 512-12·6% | 1520-15·3% |
| unclassified | 273- 6·7% | 704- 7·1% |
| Total no. of events | 4051 | 9953 |

such a procedure would probably be adopted at a later stage (cf. section (4.7)). If the same criterion is applied to the Durham events the unambiguous reaction A sample increases to 31% of the total.

The unclassified sample includes poorly measured or reconstructed events and strange particle events not identified as such on the scanning table.

## 4.5 The chi-squared ($\chi^2$) distributions

The $\chi^2$ values from GRIND are a test of the goodness of the fits, and a distribution of $\chi^2$ can be compared with a theoretical distribution of the form below to check if the empirical measurement and reconstruction parameters in the GRIND titles are satisfactory.

$$f(\chi^2)d\chi^2 = \frac{(\chi^2)^{\frac{n}{2}-1} \cdot \exp(-\frac{\chi^2}{2}) \cdot d\chi^2}{2^{\frac{n}{2}} \cdot \Gamma(\frac{n}{2})}$$

n is the number of degrees of freedom and $\Gamma$ the Gamma function.

### a) 4C fits

Figs.(19A) and (22) show the distributions of $\chi^2$ for the 4C reaction A (including ambiguous events) for each laboratory in each experiment. There are obviously differences with respect to the theoretical distributions for a four constraint fit which should have a maximum value at $\chi^2 = 2$. These differences can be explained in terms of the different measuring accuracies and the different external parameters used in GRIND. For example, for the Durham $\chi^2$ distributions the external measurement error has been underestimated by at least 20%, a better estimate of $f_o$ would have been ~125$\mu$ instead of 100$\mu$. For Saclay it was found that they were using large external errors in GRIND (~30% increase in circle fitting tolerance for

straighter tracks), and consequently the event failure rate was low and the $\chi^2$ distributions narrow.

b) 1C fits

The $\chi^2$ distributions for the 1C reactions B and C are shown in Figs.(20A),(21A),(23), and (24). The samples include ambiguous events except those ambiguous with reaction A. This point will be discussed in section (4.7).

The differences between the experimental and theoretical distributions are not easy to see, consequently it was decided to determine the median $\chi^2$ values which are listed in Table (11), the expected value being $\approx 0.5$ for a one constraint fit. Again one can conclude that the differences are due to different measuring accuracies and that the value of $f_o$ has been underestimated by at least 20%. However, these effects should not introduce any significant biases in the cross section calculations.

TABLE 11

Median $\chi^2$ values for the 1C fits

| Experiment | Laboratory | Reaction B | Reaction C |
|---|---|---|---|
| 11.5 Gev/c | Durham | 0.59 | 0.60 |
| | Saclay | 0.61 | 0.80 |
| | Milano | 0.77 | 0.80 |
| | Genoa | 0.76 | 0.57 |
| 5 Gev/c | Durham | 0.60 | 0.51 |
| | Nijmegen | 0.48 | 0.59 |

FIG. 19

$\chi^2$ AND $MM^2$ FOR THE REACTION $\pi^+p \rightarrow \pi^+p$ AT 5 GEV/c

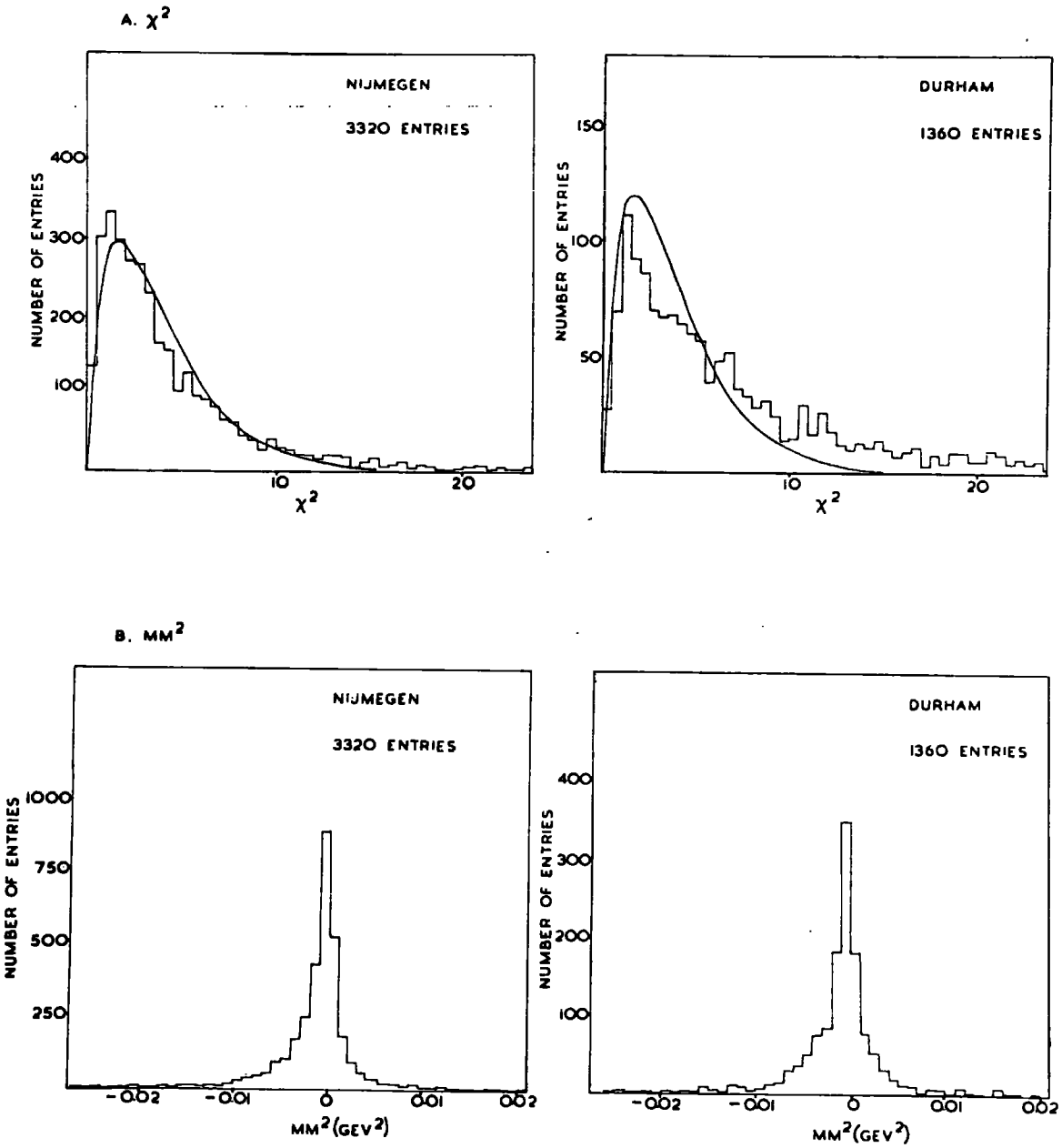

FIG. 20

$\chi^2$ AND $MM^2$ FOR THE REACTION $\pi^+p \longrightarrow \pi^+p\pi^0$ AT 5 GEV/c

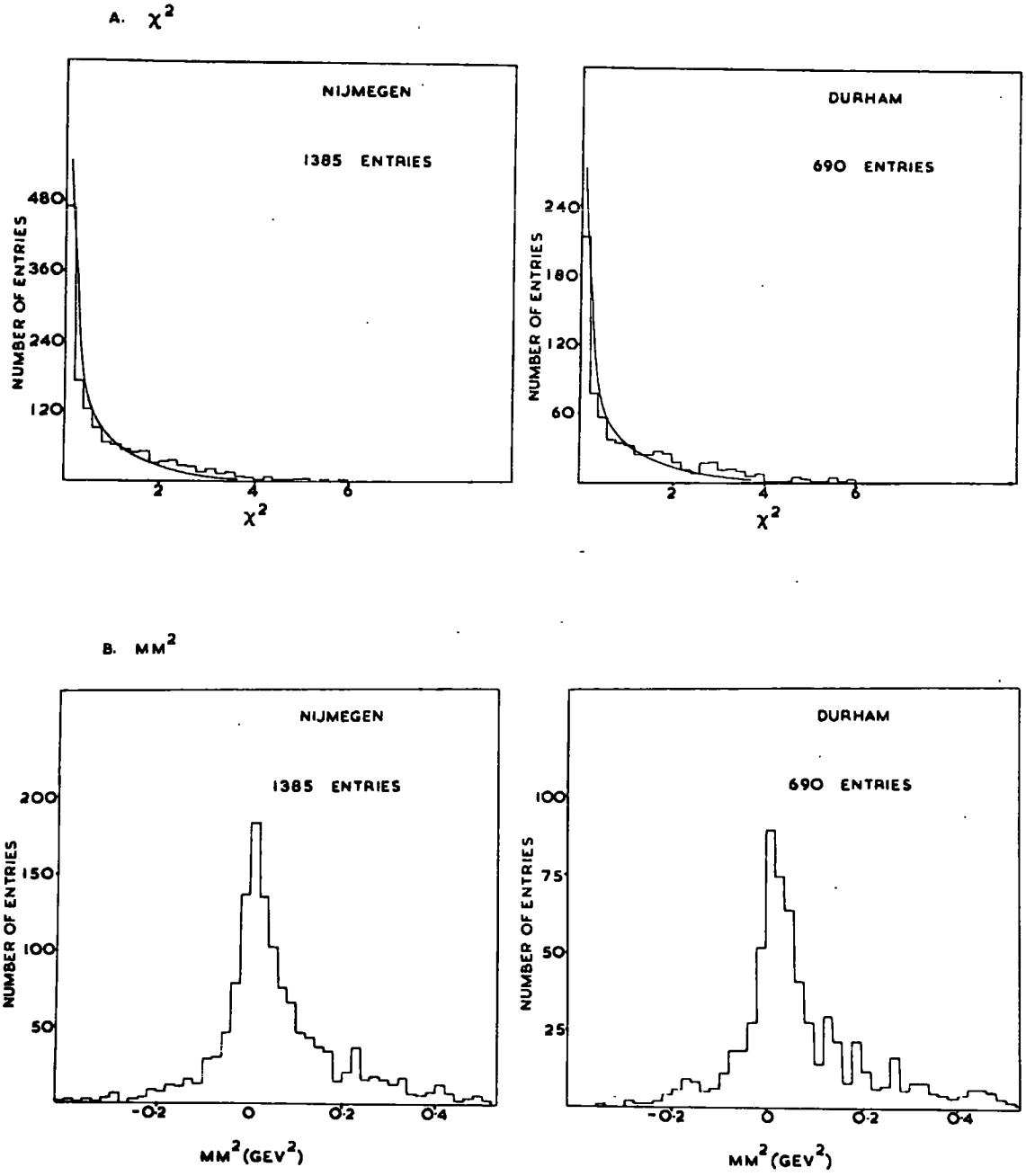

FIG. 21

$\chi^2$ AND $MM^2$ FOR THE REACTION $\pi^+p \longrightarrow \pi^+\pi^+n$ AT 5 GEV/c

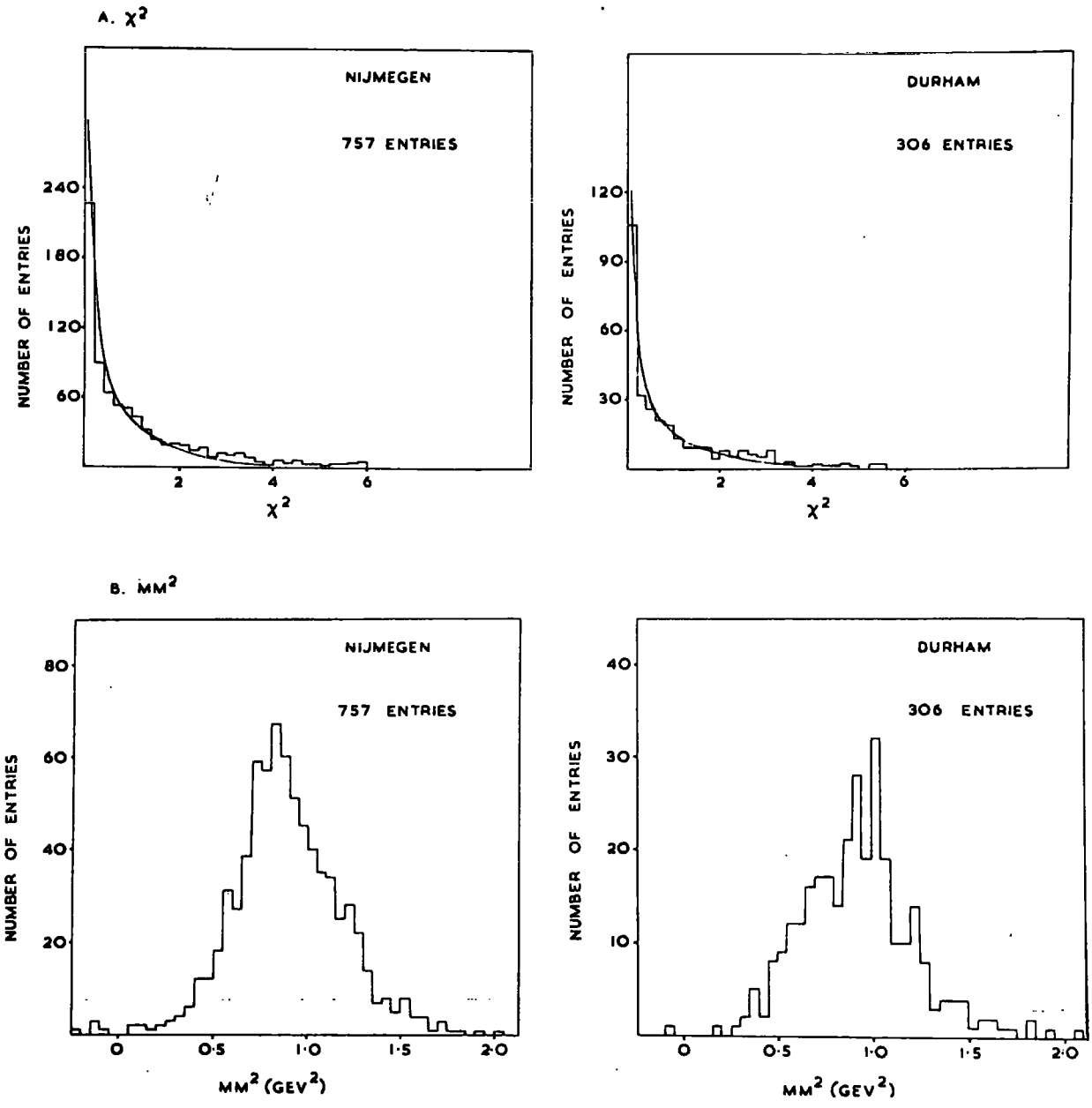

FIG. 22

$\chi^2$ FOR THE REACTION $\pi^+ p \rightarrow \pi^+ p$ AT 11·5 GEV/c

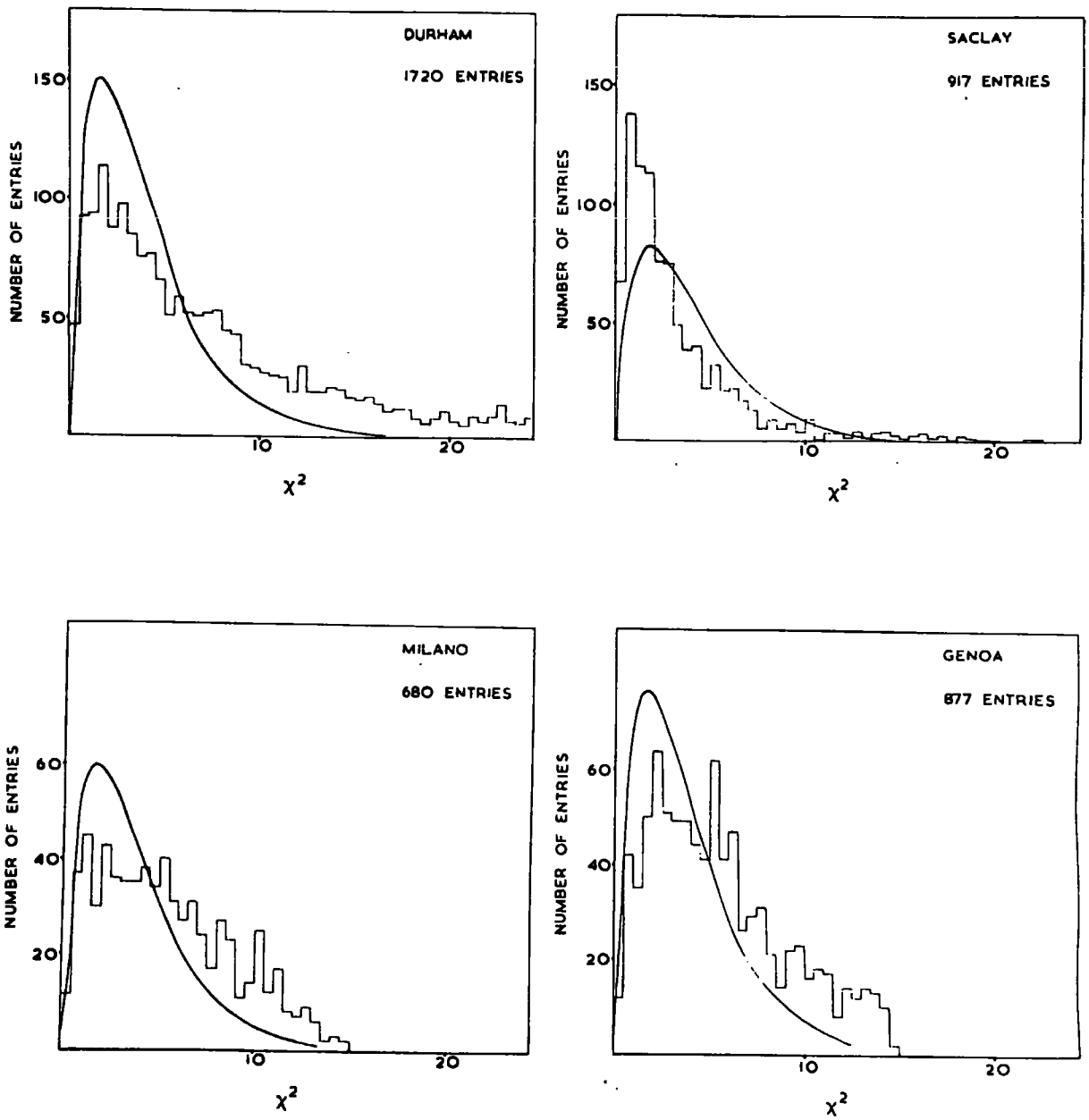

FIG. 23

$\chi^2$ FOR THE REACTION $\pi^+p \longrightarrow \pi^+p\pi^o$ AT 11·5 GEV/c

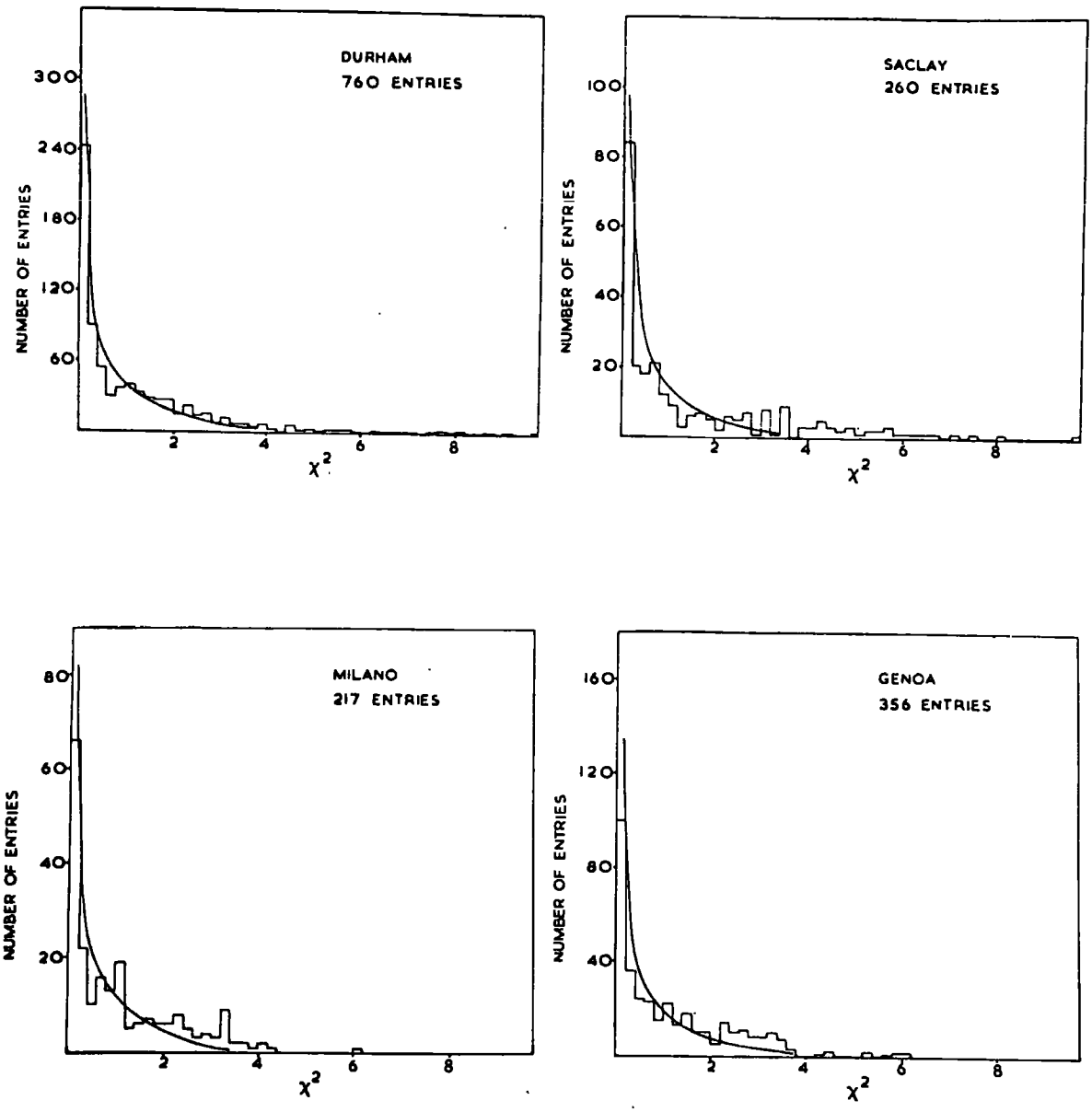

FIG. 24

$\chi^2$ FOR THE REACTION $\pi^+ p \longrightarrow \pi^+ \pi^+ n$ AT 11·5 GEV/c

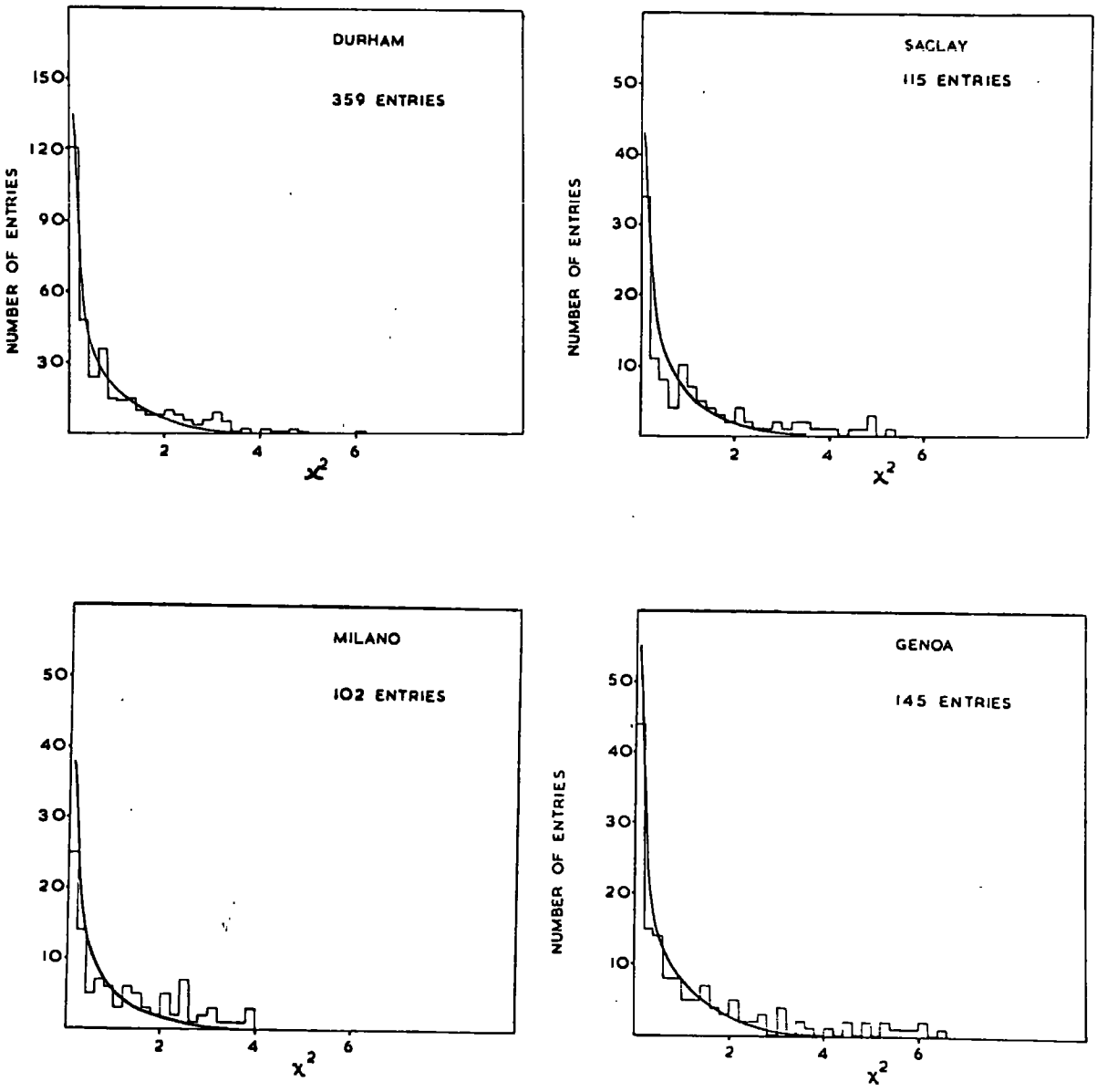

## 4.6 Missing mass squared ($MM^2$) distributions

For each reaction (hypothesis) GRIND computes, from the measured quantities, the square of the missing mass defined by

$$MM^2 = (\Delta E)^2 - (\Delta P)^2$$

where $\Delta E$ and $\Delta P$ are the missing energy and missing momentum respectively. For a 1C fit $MM^2$ is expected to correspond to the square of the mass of the appropriate missing neutral particle. For a 4C fit, where there is no missing particle, the value of $MM^2$ should be zero.

### a) 4C fits

Figs.(19B) and (25) show the $MM^2$ distributions of the 4C reaction A for each laboratory in each experiment. Instead of the expected value of zero the peaks of the distributions are significantly shifted in the negative direction by ~0.001 $Gev^2$. The reason for this shift can be understood theoretically by making a Taylor expansion of the $MM^2$ around the true values of energy and momentum in terms of the errors of measurement (38). For a 4C fit, where all the true values are zero, the first and second derivatives of the expansion are negative so making the measured $MM^2$ also negative.

### b) 1C fits

Figs.(20B),(21B),(26), and (27) show the $MM^2$ distributions for the 1C reactions B and C for each laboratory in each

FIG. 25

$MM^2$ FOR THE REACTION $\pi^+ p \longrightarrow \pi^+ p$ AT 11·5 GEV/c

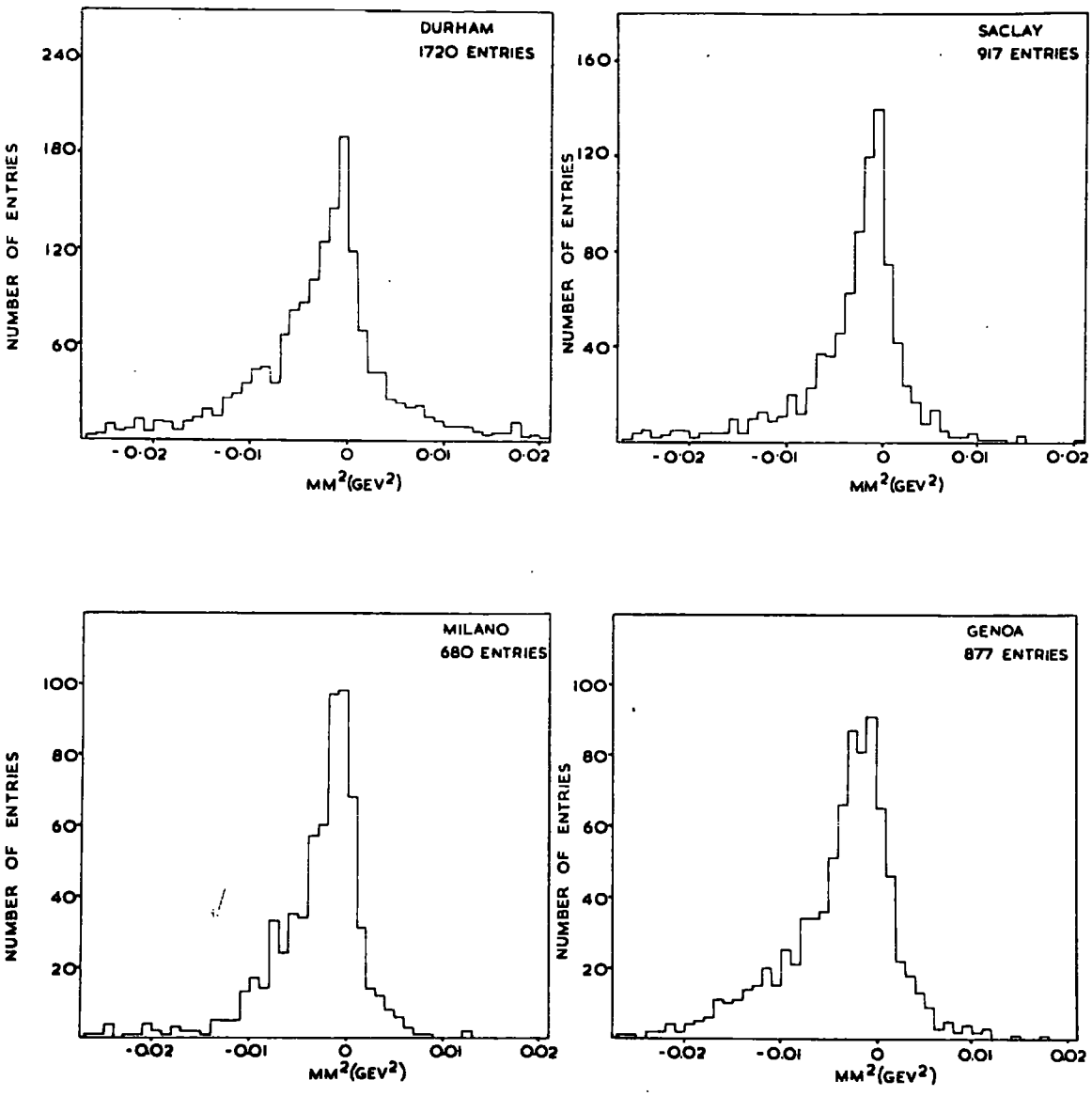

FIG. 26

$MM^2$ FOR THE REACTION $\pi^+ p \longrightarrow \pi^+ p \pi^0$ AT 11·5 GEV/c

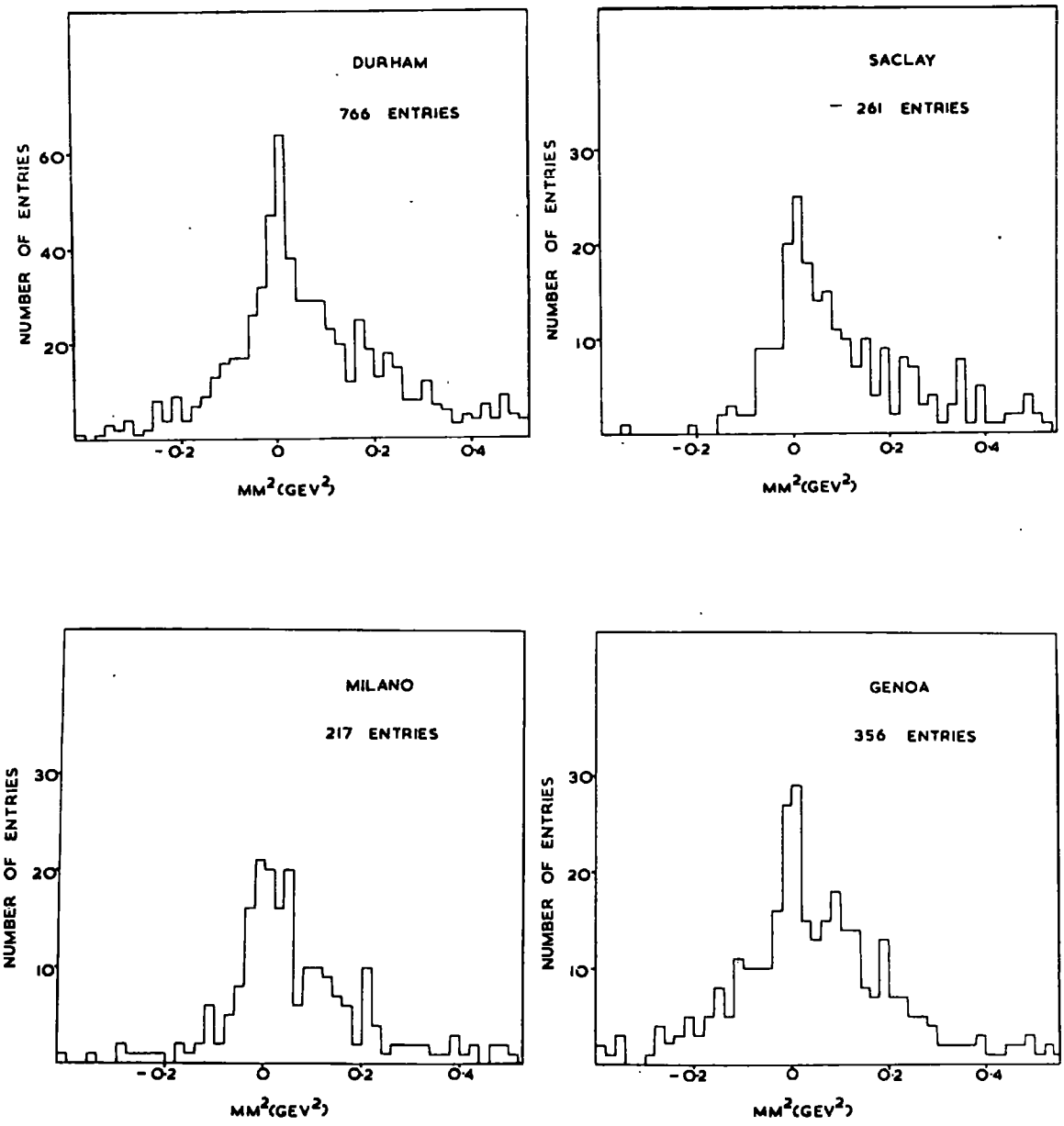

FIG. 27

$MM^2$ FOR THE REACTION $\pi^+p \rightarrow \pi^+\pi^+n$ AT 11.5 GEV/c

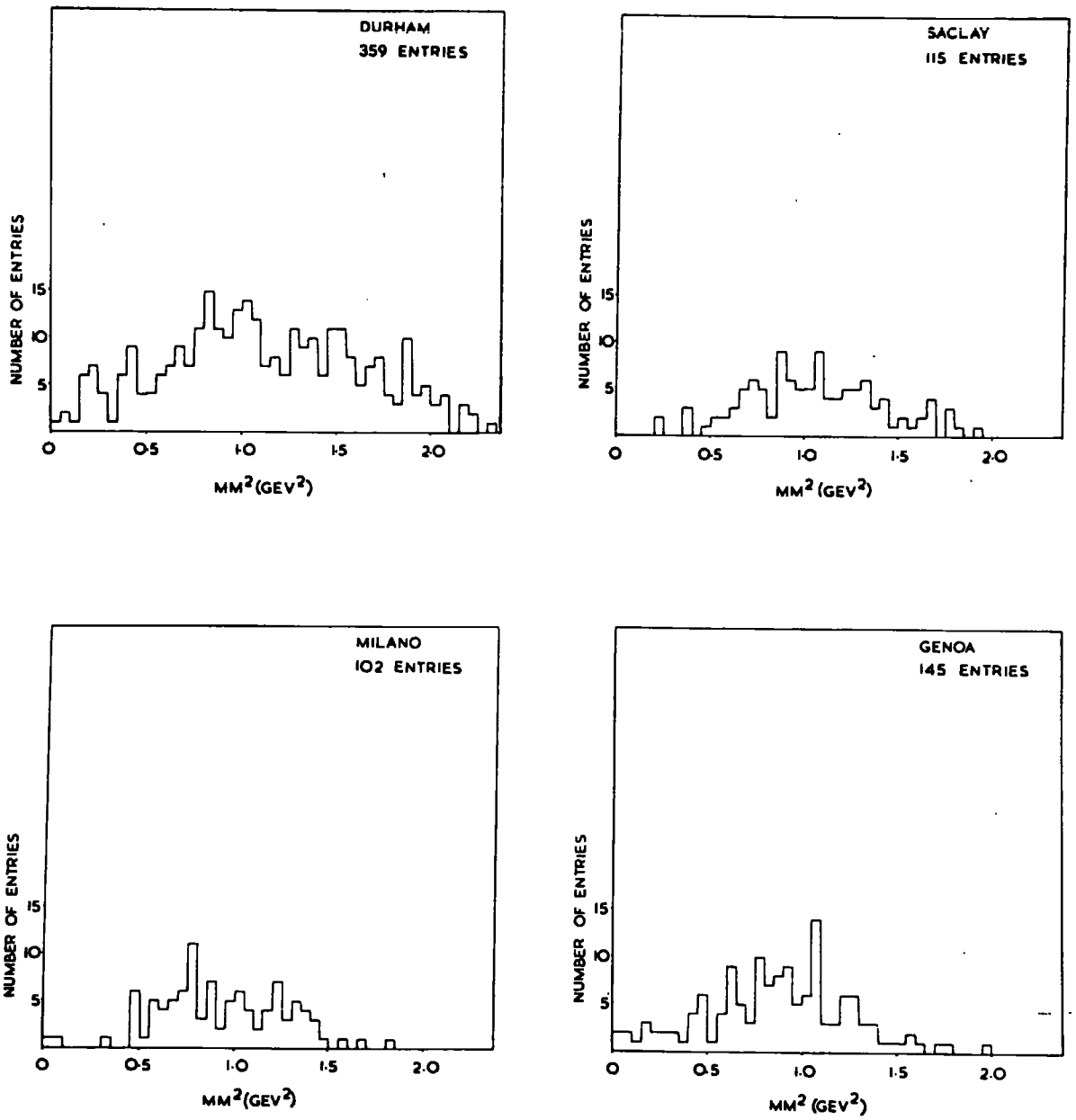

experiment. The reaction B $MM^2$ distributions peak around the square of the neutral pion mass (~0·02 $Gev^2$) as expected. However, the distributions contain a large number of entries far from the central value of which a large proportion probably do not belong to reaction B but have nevertheless given a reasonable fit.

The reaction C $MM^2$ distributions are broadly distributed around the square of the neutron mass (~0·88 $Gev^2$). Again there are a large number of entries far from the expected central value of which a large proportion probably belong to the no fit groups D or E.

It is to be noted that the 1C distributions of $MM^2$ in the 11·5 Gev/c experiment are broader than in the 5 Gev/c experiment. This is due to the higher momenta involved and consequently the greater error possible in measurement.

## 4.7 Selection of the correct reaction for each event

When an event was fitted with the 4C reaction A it was decided to accept it as the correct reaction for that event irrespective of ambiguities. This procedure is based on FAKE calculations (Lynch 1962) where generated 4C events always gave rise to a 4C fit in GRIND whereas generated 1C events did not. Furthermore, Fig.(28) shows a scatter plot of $MM^2$ against the missing energy ME for the reactions A and B in both experiments. If one simply assumes that a 1C event having values of

FIG. 28

# $MM^2$ vs ME FOR THE REACTIONS

## $\pi^+ p \longrightarrow \pi^+ p$ AND $\pi^+ p \longrightarrow \pi^+ p \pi^0$ (DURHAM DATA)

A. 11·5 GEV/c

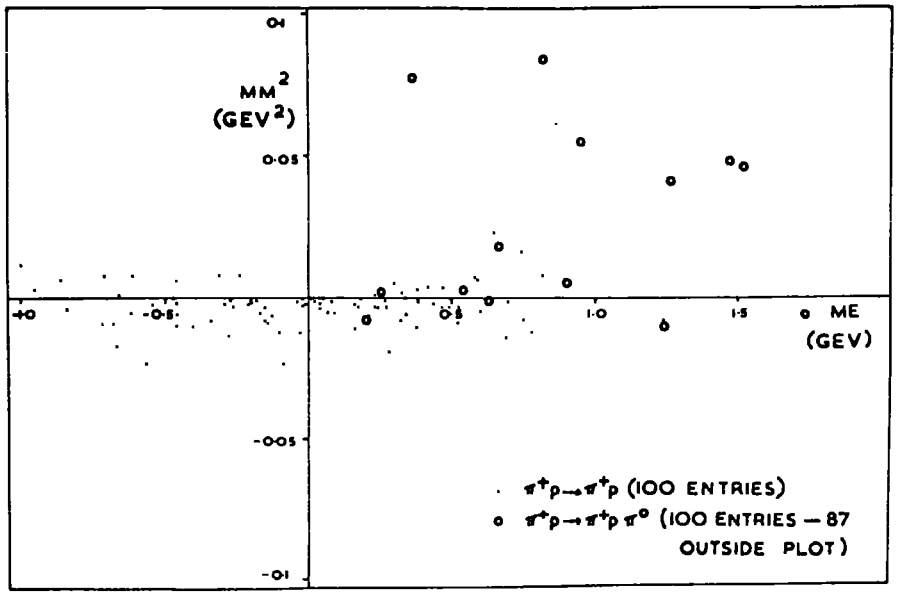


B. 5 GEV/c

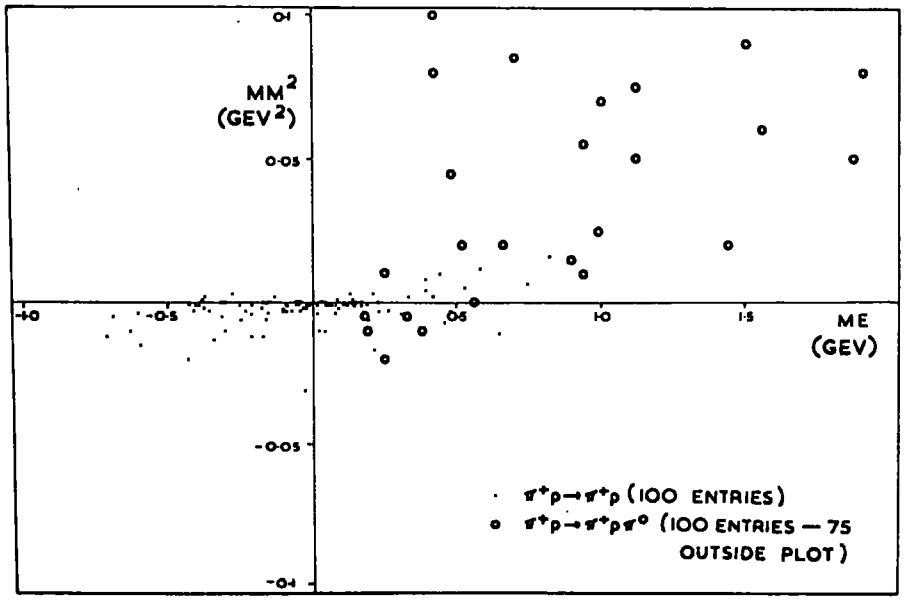

$MM^2$ and ME in the region of the 4C events would give a spurious 4C fit, then the number of reaction B events wrongly classified as reaction A events would be no more than ~3% in either experiment.

In order to reduce the possible contaminations in each reaction channel the following $MM^2$ and $\chi^2$ cuts were imposed.

| | | | |
|---|---|---|---|
| | Reaction A | - | $\chi^2 < 24$ |
| 11·5 Gev/c | Reaction B | $-0{\cdot}16 < MM^2 < 0{\cdot}16$ | $\chi^2 < 6$ |
| | Reaction C | $0{\cdot}2 < MM^2 < 1{\cdot}6$ | $\chi^2 < 6$ |
| | Reaction A | - | $\chi^2 < 24$ |
| 5 Gev/c | Reaction B | $-0{\cdot}12 < MM^2 < 0{\cdot}12$ | $\chi^2 < 6$ |
| | Reaction C | $0{\cdot}6 < MM^2 < 1{\cdot}2$ | $\chi^2 < 6$ |

The justification for the $MM^2$ cut in reaction B at 5 Gev/c is based upon $\rho^+$ meson production. For events with $MM^2$ outside the limits $\rho^+$ production is negligible (cf. Fig.(39b)). However, at 11·5 Gev/c $\rho^+$ production is not evident at this stage and no such criterion can be used. Similarly reaction C does not give clear resonant signals involving the neutral missing particle in either experiment. Consequently what has been done is to combine the $MM^2$ distributions from each laboratory and to impose a 3 standard deviation limit (determined from the width of the central peak) from the expected central value. Those events lying outside the limits were excluded from that

particular reaction cross section and from the analysis of that channel. The remaining ambiguous events between reactions B and C were classified on the basis of the highest $\chi^2$ probability. Since the number of such ambiguities remaining was no more than 4% of the reaction B total in either experiment the biases introduced by this step are not likely to be significant.

# CHAPTER 5

## ANALYSIS OF THE EVENTS

This chapter describes the preliminary analysis of the two pronged events at 5 Gev/c and 11·5 Gev/c undertaken by the author.

In the first part the reaction channel cross sections are given and the elastic scattering data analysed. Afterwards the dynamics of the inelastic reactions are examined and the production processes of the observed resonances analysed in terms of the present interaction models. Finally there is a short conclusion.

It must be emphasised that the present data is only preliminary, representing about one third of the total samples that will shortly become available. In many cases the lack of statistics is quite evident and the conclusions that can be drawn only tentative.

### 5.1 Reaction channel cross sections

The total numbers of events and cross sections for each reaction channel at 5 Gev/c and 11·5 Gev/c are given in Table (12) and Table (13) respectively.

TABLE 12

Channel cross sections at 5 Gev/c

| Reaction channel | Number of events | Cross section (mb) |
|---|---|---|
| A $p\pi^+$ | 6167 | 5·9 ±0·4 |
| B $p\pi^+\pi^o$ | 1389 | 1·3 ±0·1 |
| C $n\pi^+\pi^+$ | 723 | 0·7 ±0·1 |
| D $p\pi^+\pi^o$ $(m\pi^o)$ m>1 | 3706 | 3·5 ±0·2 |
| E $n\pi^+\pi^+$ $(m\pi^o)$ m>1 | 755 | 0·7 ±0·1 |
| ambiguous D-E | 1678 | 1·6 ±0·1 |
| unclassified | 1077 | 1·0 ±0·1 |
| Total | 15495 | 14·8 ±0·5 |

TABLE 13

Channel cross sections at 11·5 Gev/c

| Reaction channel | Number of events | Cross section (mb) |
|---|---|---|
| A $p\pi^+$ | 5691 | 4·3 ±0·4 |
| B $p\pi^+\pi^o$ | 816 | 0·6 ±0·1 |
| C $n\pi^+\pi^+$ | 525 | 0·4 ±0·1 |
| D $p\pi^+\pi^o$ $(m\pi^o)$ m>1 | 2789 | 2·1 ±0·2 |
| E $n\pi^+\pi^+$ $(m\pi^o)$ m>1 | 1096 | 0·8 ±0·1 |
| ambiguous D-E | 1860 | 1·5 ±0·1 |
| unclassified | 808 | 0·6 ±0·1 |
| Total | 13585 | 10·3 ±0·5 |

In the cases of the elastic cross sections corrections of 31% and 37%, at 5 Gev/c and 11·5 Gev/c respectively, have been made to the observed numbers of events for the losses at small scattering angles. These corrections are discussed in more detail in section (5.2). The cross sections for the inelastic reaction channels B and C are compared with other cross sections over an incident pion momentum range of 2·75 Gev/c to 11·5 Gev/c in Fig.(29). The data has been taken from references (39-41).

The reaction B cross section at 11·5 Gev/c is to be regarded with some caution due to the contaminations present in this channel and the criteria imposed to remove them (cf. section (5.5.a)).

## 5.2 Elastic scattering

In order to correct for the scanning loss of elastic events at small scattering angles the azimuthal angle ($\phi$) of the recoil proton about the beam direction has been plotted against the four momentum transfer from the target to the proton (t) in Fig.(30) at 5 Gev/c and 11·5 Gev/c. The loss of events for $-t \leq 0{\cdot}02$ Gev$^2$ and $\phi \simeq 90^\circ$ (parallel to the optic axes of the cameras) is quite marked at both energies. The loss due to the angle $\phi$ was estimated from these plots, after which the loss at low values of t was found from an exponential plot of t (after corrections for $\phi$ losses) which could be extrapolated to $-t = 0$. These corrections amounted to 1539 events

FIG. 29

$\pi^+p$ INELASTIC CROSS SECTIONS AT VARIOUS INCIDENT MOMENTA

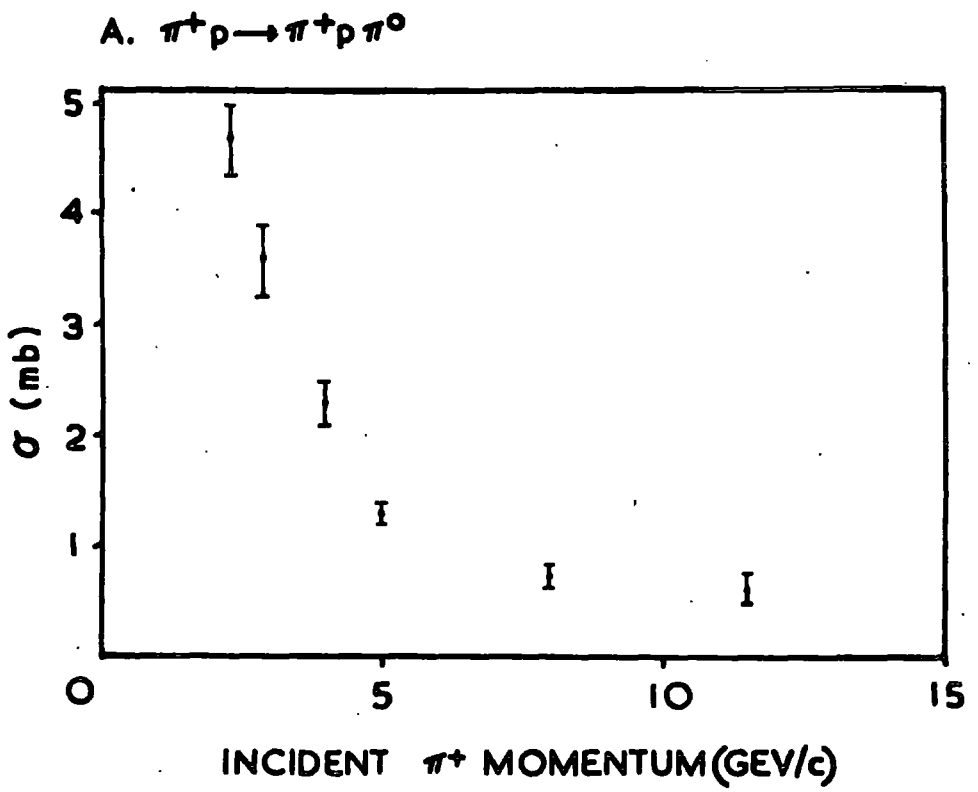


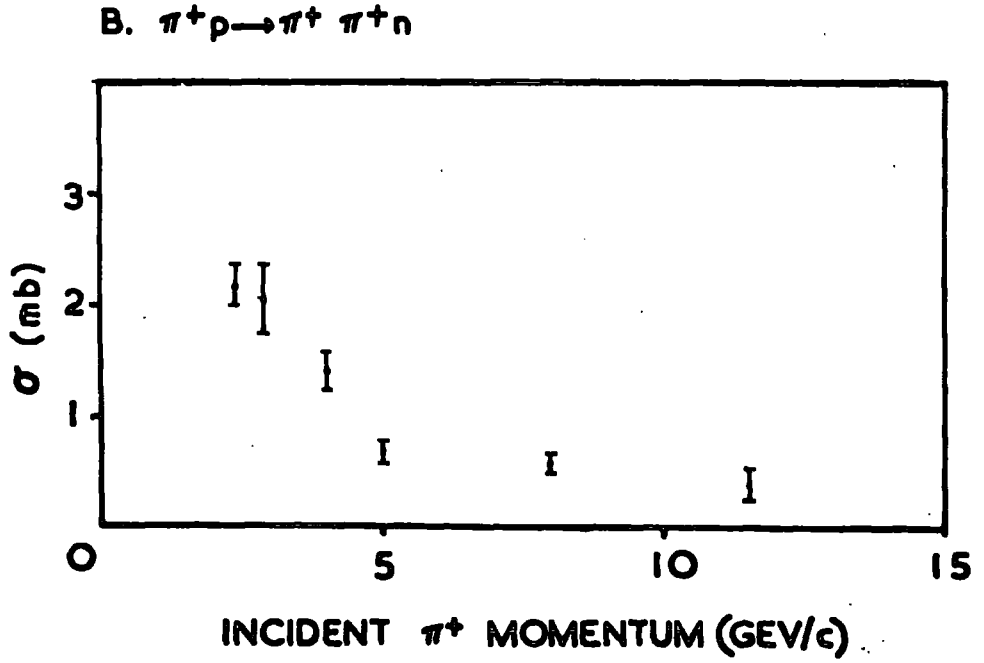

FIG. 30

# $t$ vs. $\phi$ IN THE REACTION $\pi^+p \rightarrow \pi^+p$

A. 11·5 Gev/c

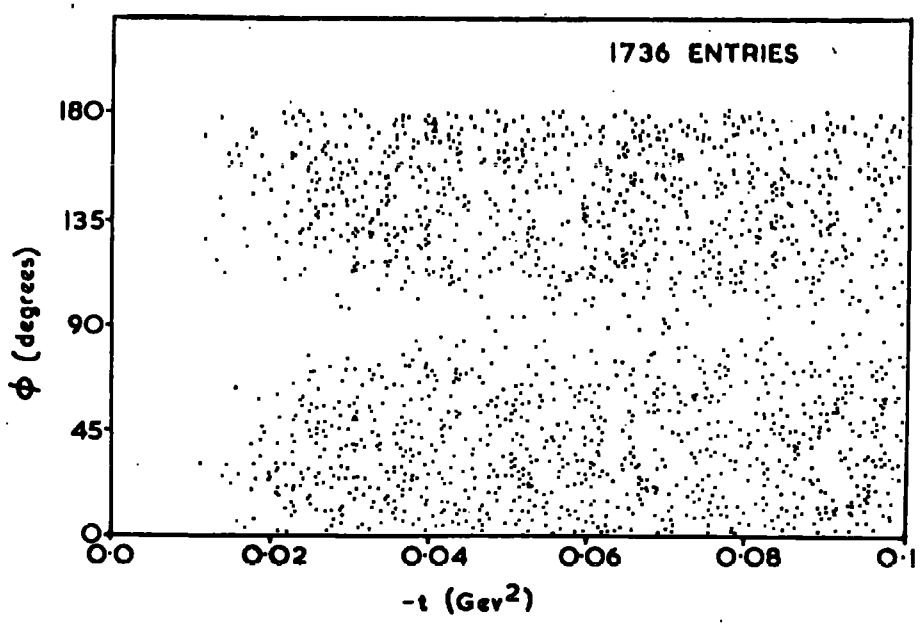


B. 5 Gev/c

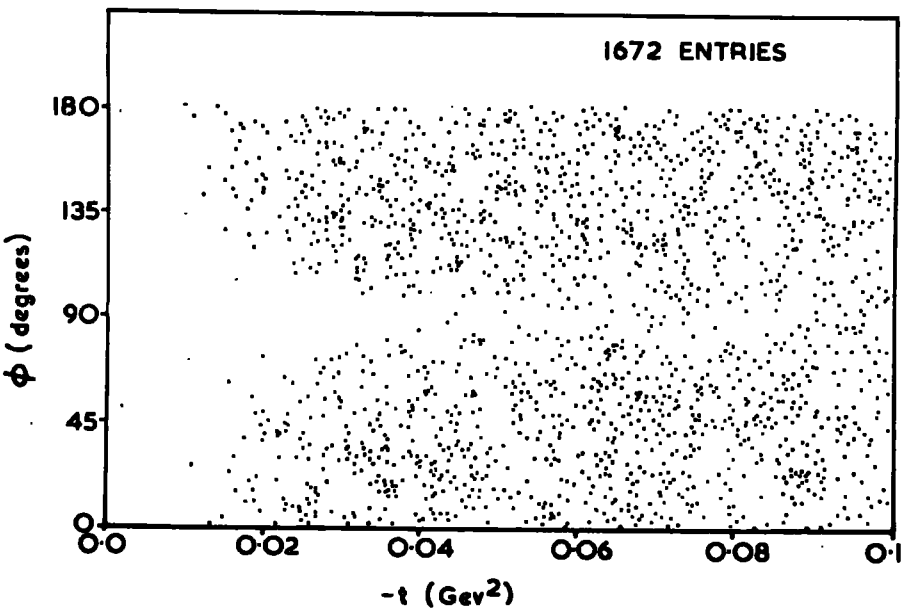

(~37% of the observed elastic total) and 1487 events (~31% of the observed elastic total) at 11·5 Gev/c and 5 Gev/c respectively.

Figs.(31B) and (32B) show the elastic differential cross sections, $\delta\sigma/\delta t$, for the forward diffraction peaks ($-t \leq 0{\cdot}6$ $Gev^2$) at 5 Gev/c and 11·5 Gev/c respectively. Both sets of data are consistent with exponential distributions of the form

$$\frac{\delta\sigma}{\delta t} = A.\exp(Bt)$$

Least squares fits over the region $0{\cdot}07 \leq -t < 0{\cdot}4$ $Gev^2$ yield values for the slope B and the intersection A ($-t = 0$) which are listed in Table (14) along with values obtained at 4 Gev/c (42) and 8 Gev/c (41).

TABLE 14

Fits to the forward diffraction peaks

| Experiment | A mb/$Gev^2$ | B $Gev^{-2}$ |
|---|---|---|
| 4 Gev/c | - | 7·3 ±0·2 |
| 5 Gev/c | 39·2 ±1·1 | 7·0 ±0·2 |
| 8 Gev/c | - | 7·5 ±0·1 |
| 11·5 Gev/c | 34·1 ±2·4 | 7·9 ±0·4 |

The values of the slope B remain fairly constant over a large energy range implying, from the optical theorem, a constant

FIG. 31

DIFFERENTIAL CROSS SECTION $\left[\frac{\delta\sigma}{\delta t}\right]$ FOR REACTION $\pi^+p \rightarrow \pi^+p$ AT 5 GEV/c

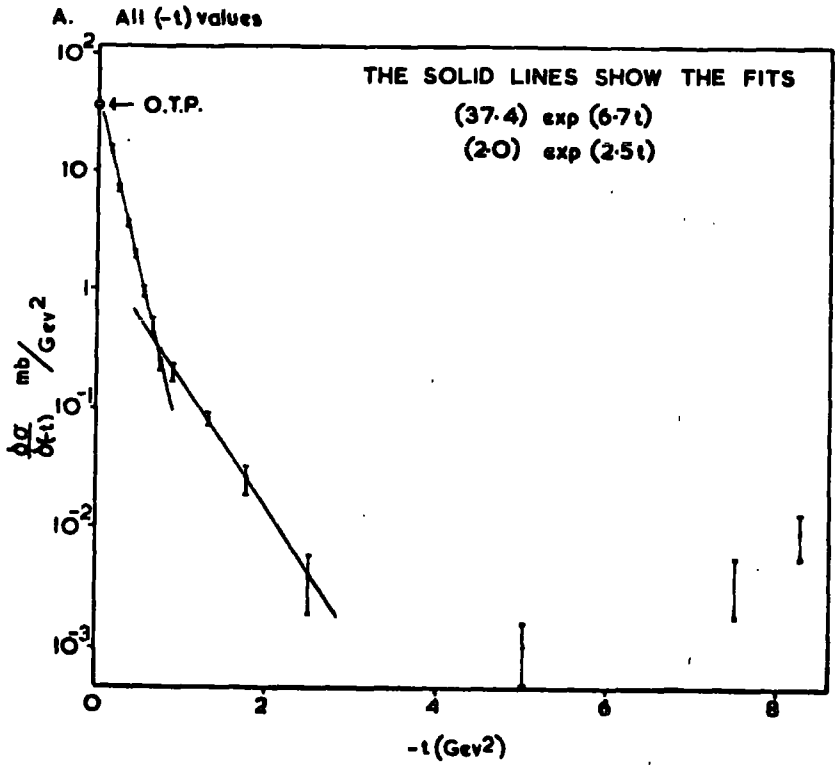


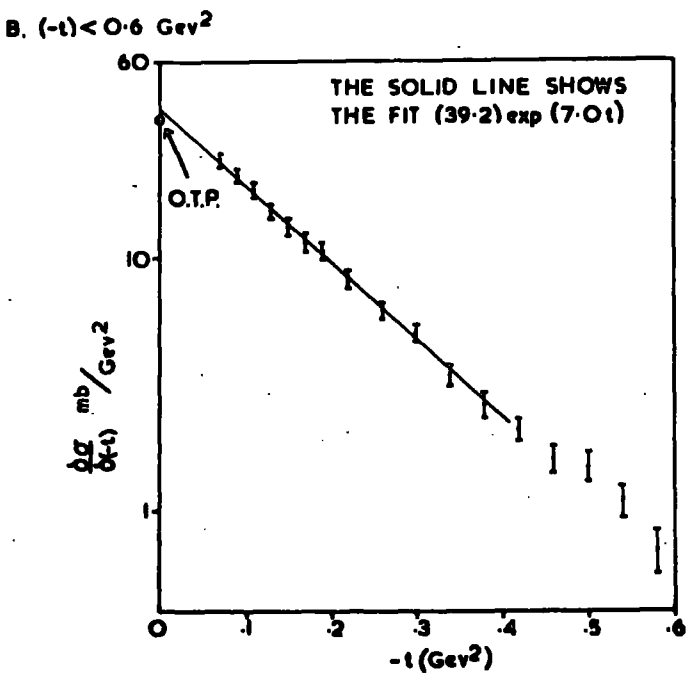

FIG. 32

DIFFERENTIAL CROSS SECTION $\left[\frac{\delta\sigma}{\delta t}\right]$ FOR REACTION $\pi^+p \longrightarrow \pi^+p$ AT 11·5 GEV/c

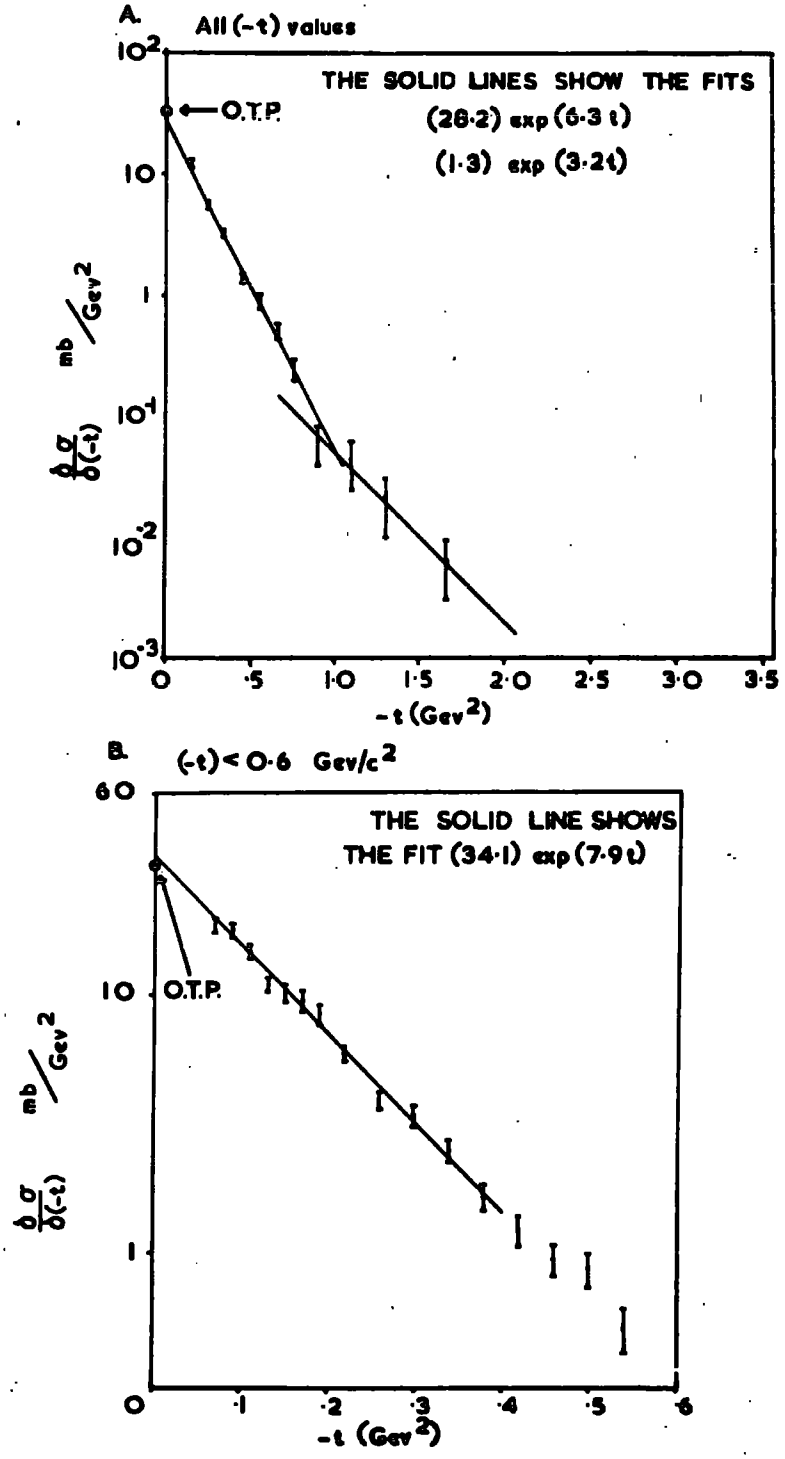

radius of interaction volume.

The optical theorem points (O.T.P) shown in Figs.(31B) and (32B) have been calculated from the total cross sections of 26·5mb and 24·9mb using the expression

$$O.T.P = \frac{\sigma^2_{total}}{16\pi}$$

From the optical theorem formula

$$\frac{\delta\sigma}{\delta t}(-t=0) = (1+\rho^2).\frac{\sigma^2_{total}}{16\pi}$$

the values of $\rho^2$ (the square of the ratio of the real to imaginary part of the forward scattering amplitude) obtained were as follows

$$\rho^2 = 0{\cdot}096 \pm 0{\cdot}006 \quad \text{at } 5 \text{ Gev/c}$$
$$\rho^2 = 0{\cdot}079 \pm 0{\cdot}005 \quad \text{at } 11{\cdot}5 \text{ Gev/c}$$

Evidently the forward scattering amplitude is almost purely imaginary and the real contribution seems to be decreasing with increasing primary energy as expected.

Figs.(31A) and (32A) show the differential cross sections over the whole range of four momentum transfer t. It is evident in both plots that up to a value of $-t \simeq 2$ Gev$^2$ they can be described by two exponentials of the form

$$\frac{\delta\sigma}{\delta t} = A_1.\exp(B_1 t) \qquad 0{\cdot}07 < -t < \sim 1{\cdot}0 \text{ Gev}^2$$

$$\frac{\delta\sigma}{\delta t} = A_2.\exp(B_2 t) \qquad \sim 1{\cdot}0 < -t < 2{\cdot}0 \text{ Gev}^2$$

This sharp change of slope has also been reported at 8 Gev/c (41). The values for the slopes $B_1$ and $B_2$ are listed in Table (15).

TABLE 15

Values of double exponential slopes

| Experiment | $B_1$ Gev$^{-2}$ | $B_2$ Gev$^{-2}$ | Intersection Point |
|---|---|---|---|
| 5 Gev/c | 6·7 ±0·3 | 2·5 ±0·5 | $-t \approx 0{\cdot}7$ |
| 8 Gev/c | 7·9 ±0·3 | 3·7 ±0·5 | $-t \approx 0{\cdot}7$ |
| 11·5 Gev/c | 6·3 ±0·5 | 3·2 ±0·7 | $-t \approx 1{\cdot}0$ |

It has been shown by Frautschi and Margolis (43) that sharp changes in the slope of the differential cross sections of elastic scattering may be interpreted as the result of multiple scattering corrections due to Pomeron exchange.

At 5 Gev/c 13 events have been observed to be scattered into the backward hemisphere corresponding to a cross section of 12·5 ±0·8$\mu$b. At 8 Gev/c (41) the backward scattering corresponds to a cross section of 4·5 ±1·2$\mu$b. Extrapolating to 11·5 Gev/c would indicate a small backward scattering cross section,

and in fact at this energy no evidence for backward scattering is seen.

In conclusion the $\pi^+p$ elastic scattering shows a diffraction character in that the differential cross section has a pronounced, approximately energy independent, peak in the forward direction, and in the sense that the forward scattering amplitude is almost purely imaginary

## 5.3 5 Gev/c inelastic 1C reactions

### a) Introduction

The centre of mass momentum and angular distributions for reaction B ($\pi^+p \rightarrow \pi^+p\pi^o$) and reaction C ($\pi^+p \rightarrow \pi^+\pi^+n$) are shown in Figs.(33) and (34). The marked peaking of the momentum distributions in reaction B reflects the two-body nature of the interaction, while the sharp forward-backward assymmetry of the angular distributions arises from the peripheral nature of the interaction. The assymmetry parameter R, which is defined as

$$R = \frac{(\text{Forward-Backward})}{(\text{Forward+Backward})}$$

where Forward means the number of particles emitted in the beam direction, is given in Table (16) for each of the particles. It is evident that there is more symmetry in the $\pi^+\pi^+$ distribution of reaction C than in the $\pi^+\pi^o$ distribution of reaction

FIG. 33

CENTRE OF MASS MOMENTUM ($p^*$) FOR THE INELASTIC REACTIONS AT 5GEV/c

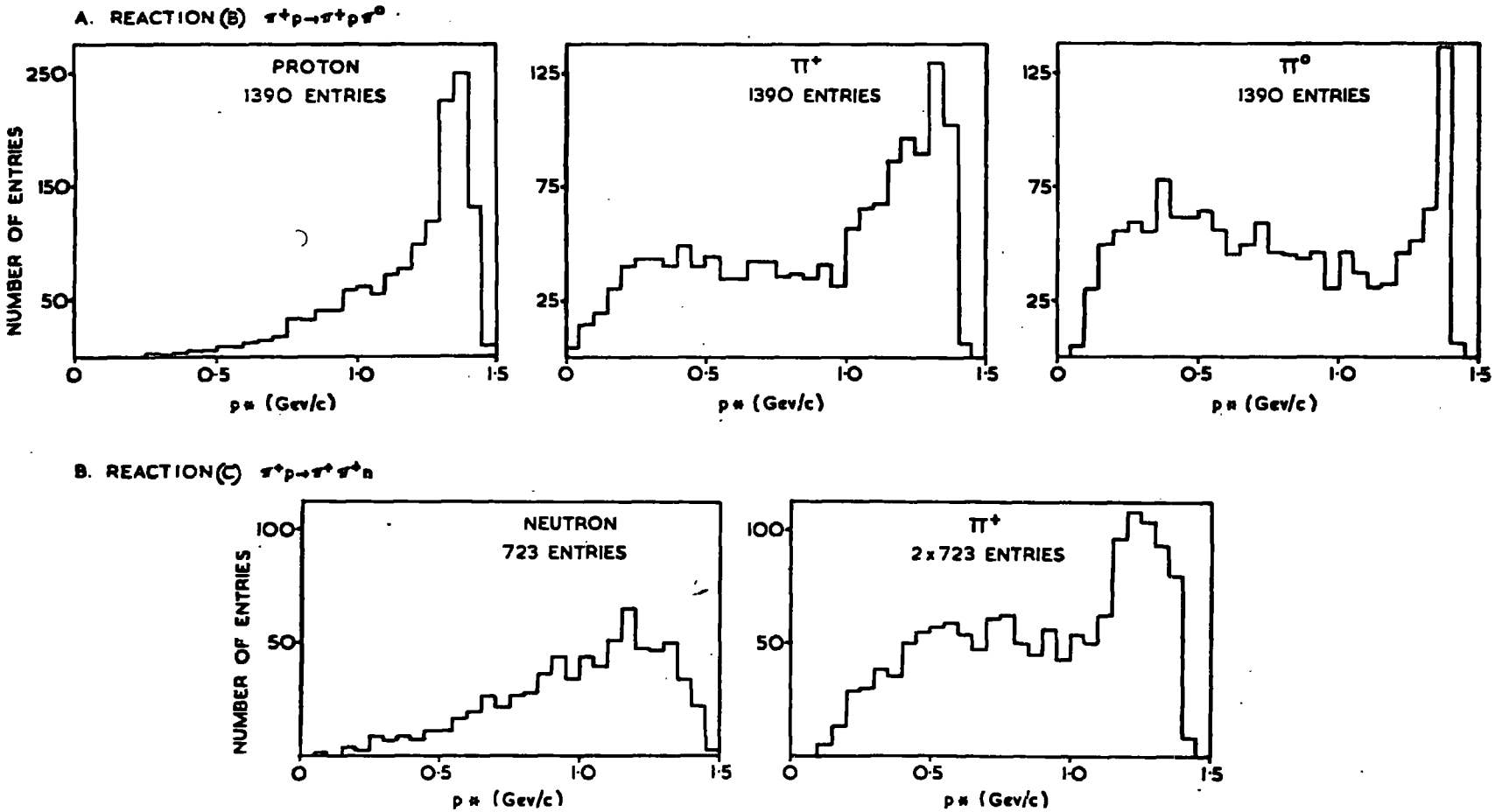

FIG. 34

# CENTRE OF MASS ANGLE ($\Theta^*$) DISTRIBUTIONS FOR THE INELASTIC REACTIONS AT 5 GEV/C

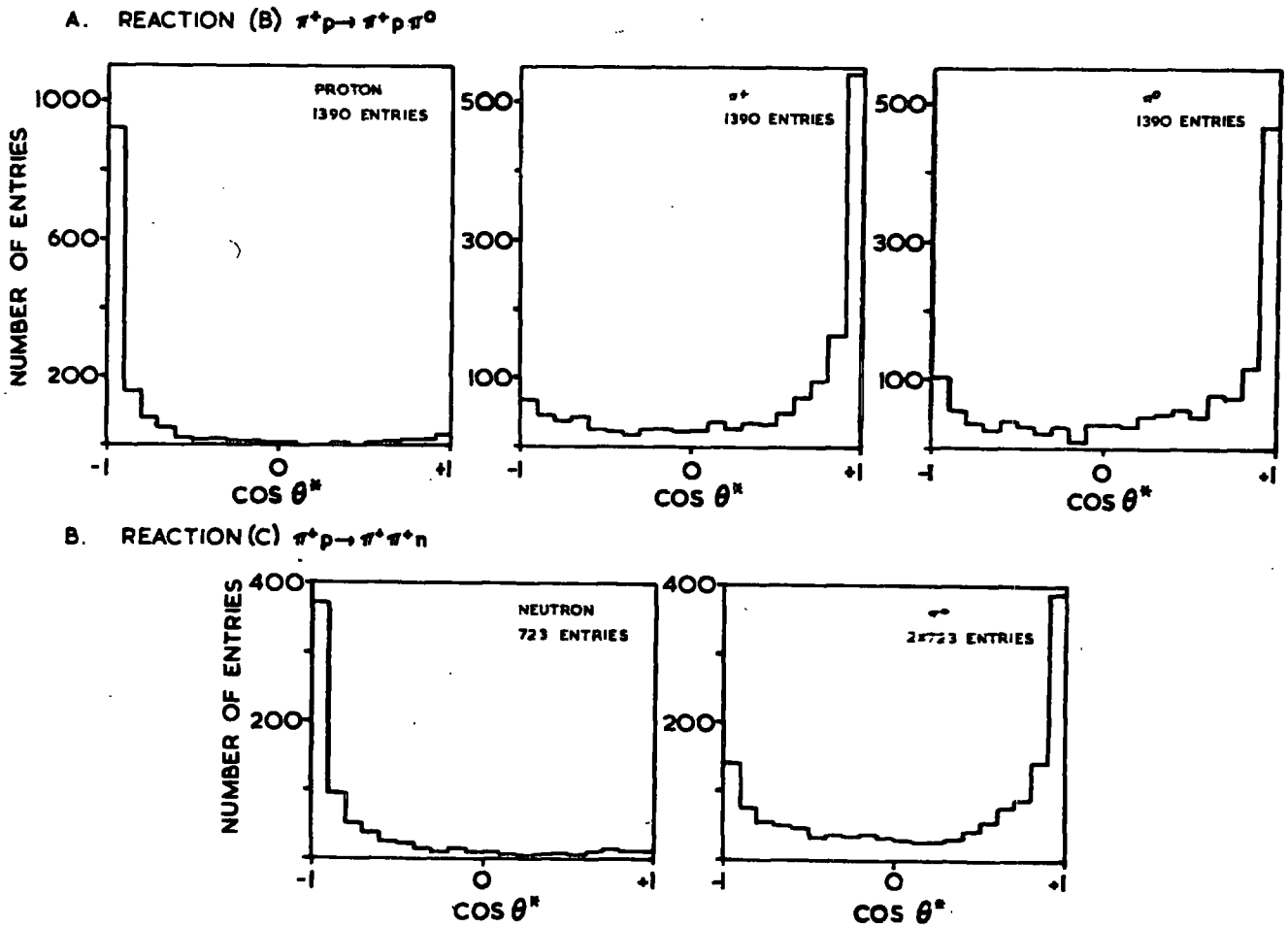

B. This could be a reflection of the conspicuous $\rho^+(760\text{Mev})$

TABLE 16

Assymmetry parameter R at 5 Gev/c

| Reaction | Particle | R |
|---|---|---|
| B. $\pi^+p \rightarrow \pi^+p\pi^o$ | Proton | $-0.86 \pm 0.09$ |
| | $\pi^+$ | $0.53 \pm 0.06$ |
| | $\pi^o$ | $0.44 \pm 0.05$ |
| C. $\pi^+p \rightarrow \pi^+\pi^+n$ | Neutron | $-0.79 \pm 0.16$ |
| | $\pi^+$ | $0.26 \pm 0.05$ |

meson production in the $\pi^+\pi^o$ system which, being a highly peripheral reaction as will be seen later, would cause the $\pi^+$ and the $\pi^o$ to go forward in the overall centre of mass.

Also the two combinations of like and unlike boson pairs may be in opposite parity states, that is the $\pi^+\pi^+$ combination ($I = 2$) will be in an even angular momentum state, and the $\pi^+\pi^o$ combination ($I = 1,2$) will be in an odd or even angular momentum state. Because of this difference and the importance of angular momentum in high energy low multiplicity interactions the angular distributions of the like and unlike pions should be different.

The effect of angular momentum conservation at 5 Gev/c can be seen in the Dalitz plot of the effective masses $M(p\pi^+)$ and $M(\pi^+\pi^o)$ in Fig.(35) where there is overpopulation of the

boundaries of the plot.

Reaction B is dominated by the production of the resonances $N^{*++}$(1236Mev) and $\rho^{+}$(760Mev); however, no evidence has been found for the $g^{+}$(1650Mev) meson or any higher mass isobars. There is little evidence for resonance production in reaction C except for a small enhancement corresponding to the $N^{*+}$(1236)

In the next sections the N* and ρ resonances are examined and, considering the peripheral nature of the interactions, attempts made to reproduce the data using the absorptive peripheral model and the Regge Pole model. Finally the $\pi^{+}\pi^{o}$ scattering cross section has been deduced using the Chew and Low extrapolation method.

b) N*(1236Mev) production

Fig.(35) shows the Dalitz plot of the effective masses $M(p\pi^{+})$ and $M(\pi^{+}\pi^{o})$ in reaction B. There is clearly an excess of events in a band around the $N^{*++}$(1236Mev) in the $p\pi^{+}$ system. Similarly Figs.(36) and (37) show the Dalitz plots of the effective masses $M(p\pi^{o})$ and $M(\pi^{+}\pi^{o})$ in reaction B and $M(n\pi^{+})$ and $M(\pi^{+}\pi^{+})$ in reaction C, but there is little evidence for the production of the $N^{*+}$(1236Mev) decaying to $p\pi^{o}$ and $n\pi^{+}$ respectively.

The projections of the Dalitz plots are shown in Figs.(38A), (38B), and (40A) where the effective mass combinations $M(p\pi^{+})$, $M(p\pi^{o})$, and $M(n\pi^{+})$ are presented. The strong production of $N^{*++}$

FIG. 35

$M(p\pi^+)$ vs. $M(\pi^+\pi^0)$ IN REACTION $\pi^+p \to \pi^+p\pi^0$ AT 5 GEV/c

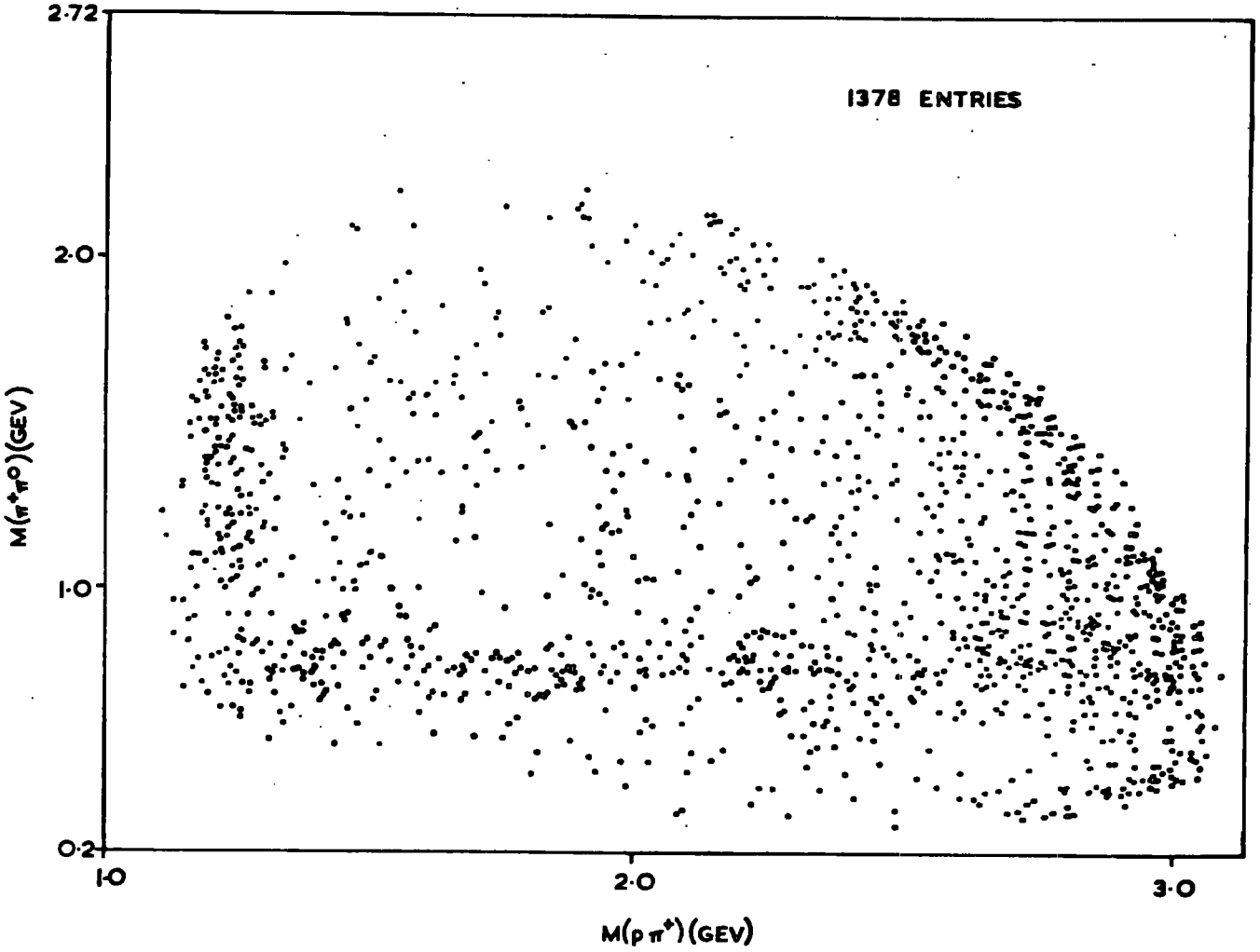

FIG. 36

$M(p\pi^0)$ vs. $M(\pi^+\pi^0)$ IN REACTION $\pi^+p \rightarrow \pi^+p\pi^0$ AT 5 GEV/c

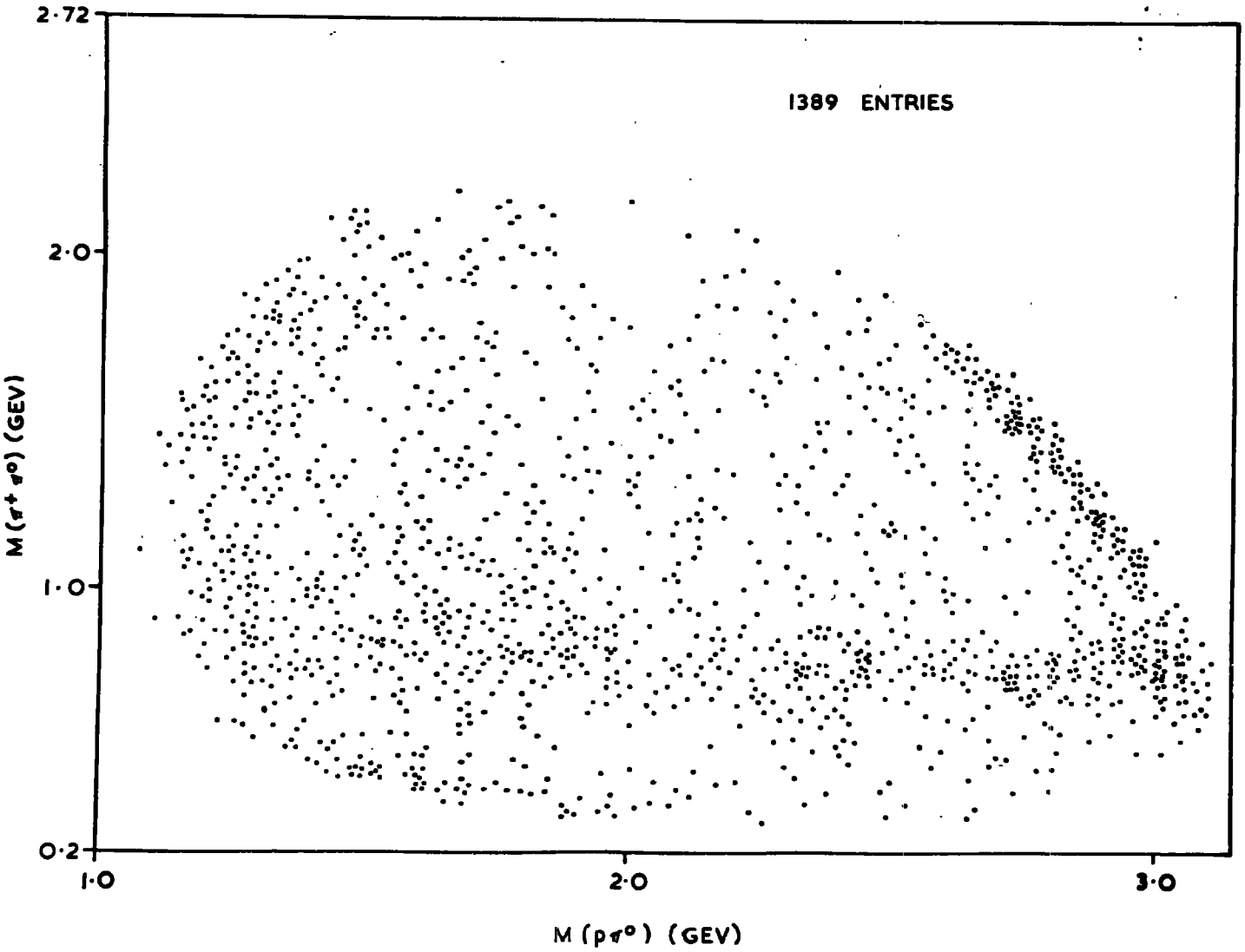

FIG. 37

# $M(n\pi^+)$ vs. $M(\pi^+\pi^+)$ IN REACTION $\pi^+ p \rightarrow \pi^+\pi^+ n$ AT 5 GEV/c

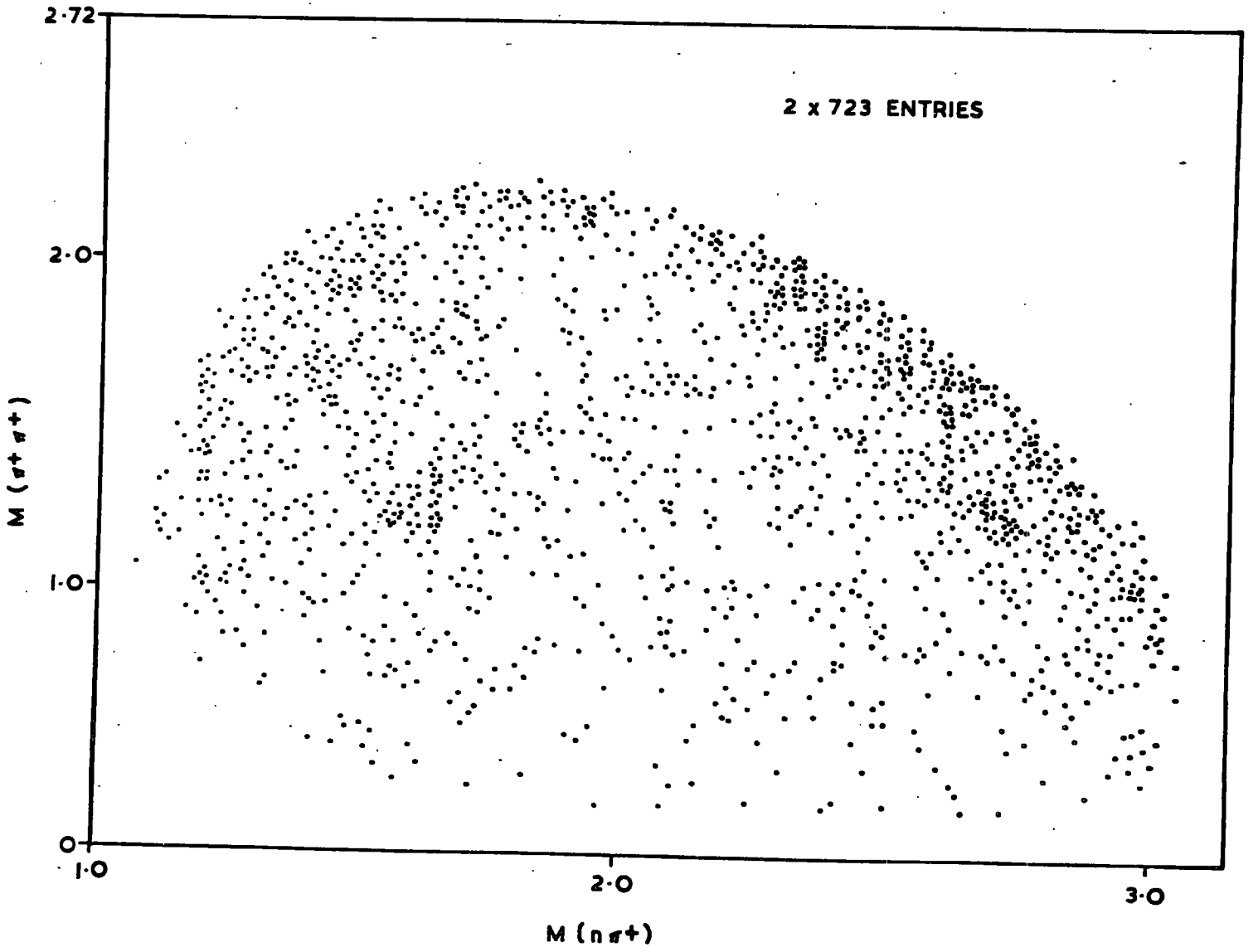

FIG. 38

# $M(p\pi^+)$ AND $M(p\pi^0)$ IN REACTION $\pi^+p \rightarrow \pi^+p\pi^0$ AT 5 GEV/c

A. $M(p\pi^+)$

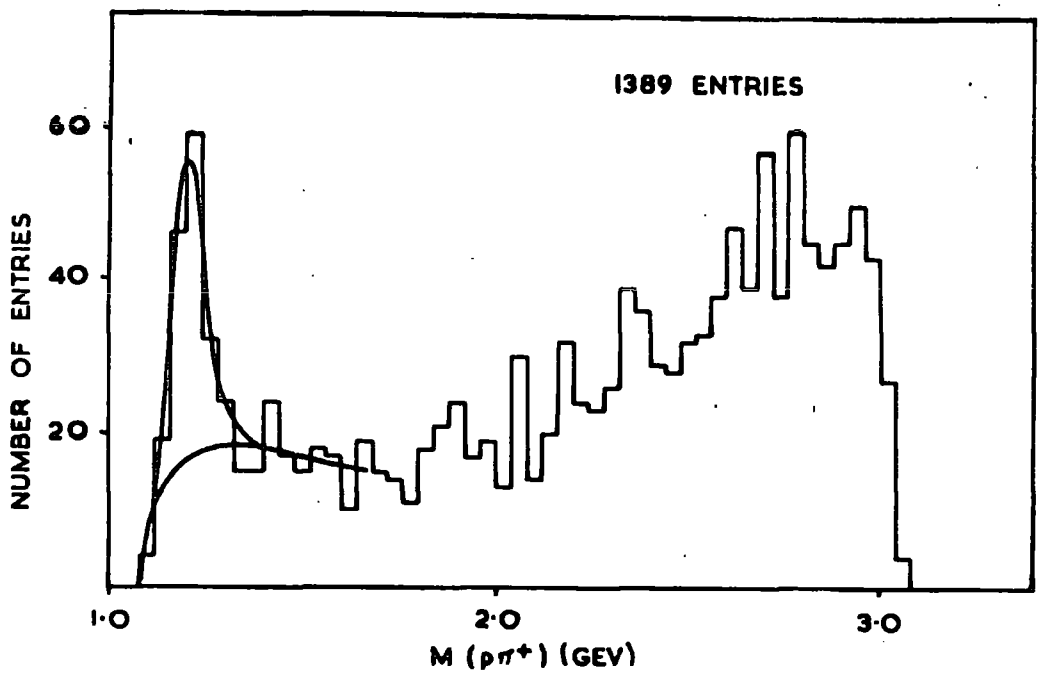


B. $M(p\pi^0)$

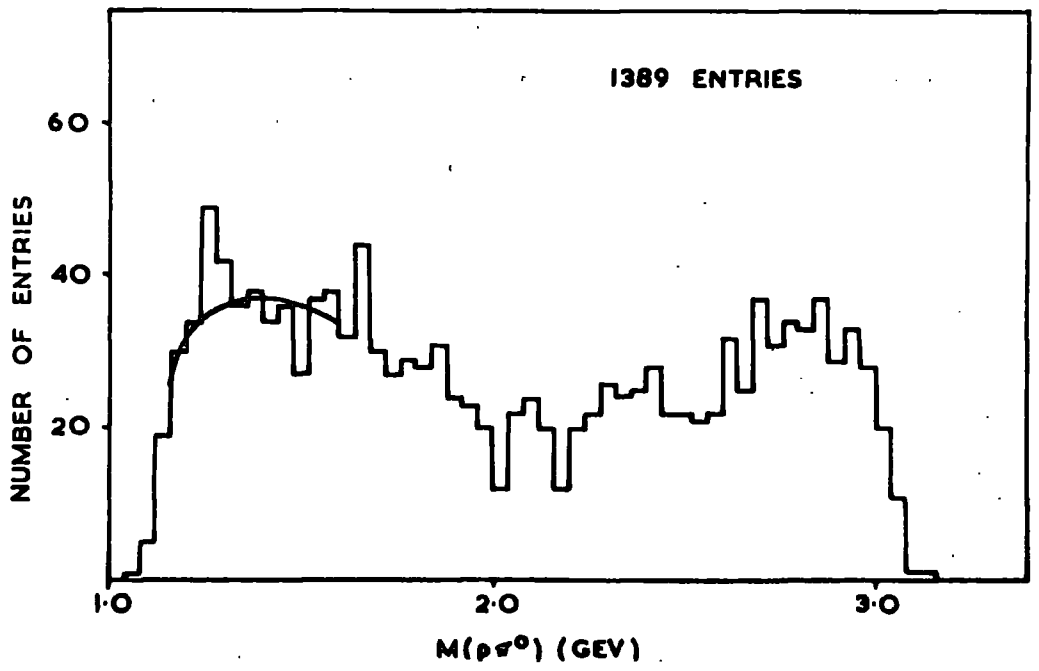

FIG. 39

# $M(\pi^+\pi^0)$ IN REACTION $\pi^+ p \rightarrow \pi^+ p \pi^0$ AT 5 GEV/c

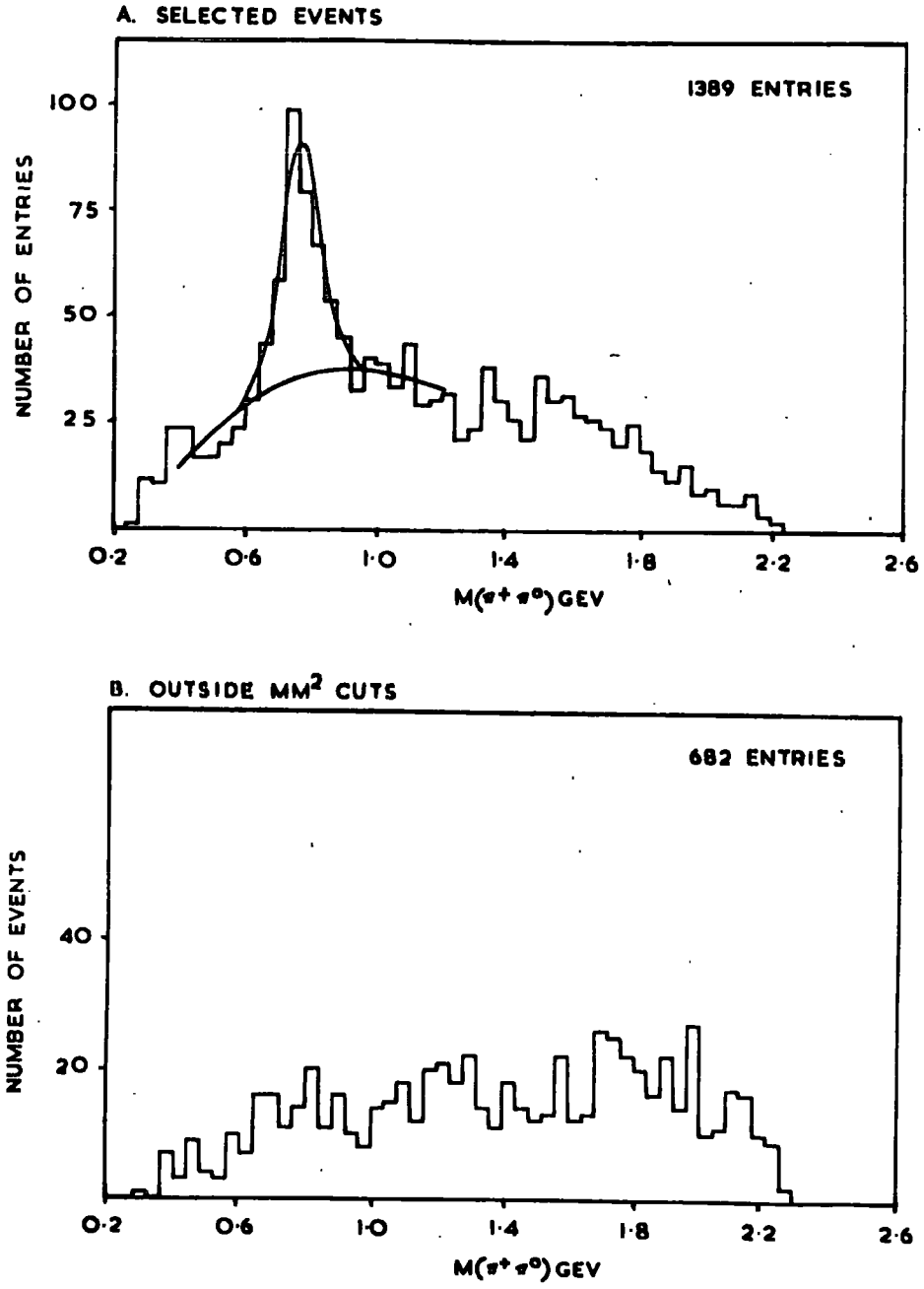

FIG. 40

# $M(n\pi^+)$ AND $M(\pi^+\pi^+)$ IN REACTION $\pi^+ p \longrightarrow \pi^+\pi^+ n$ AT 5 GEV/c

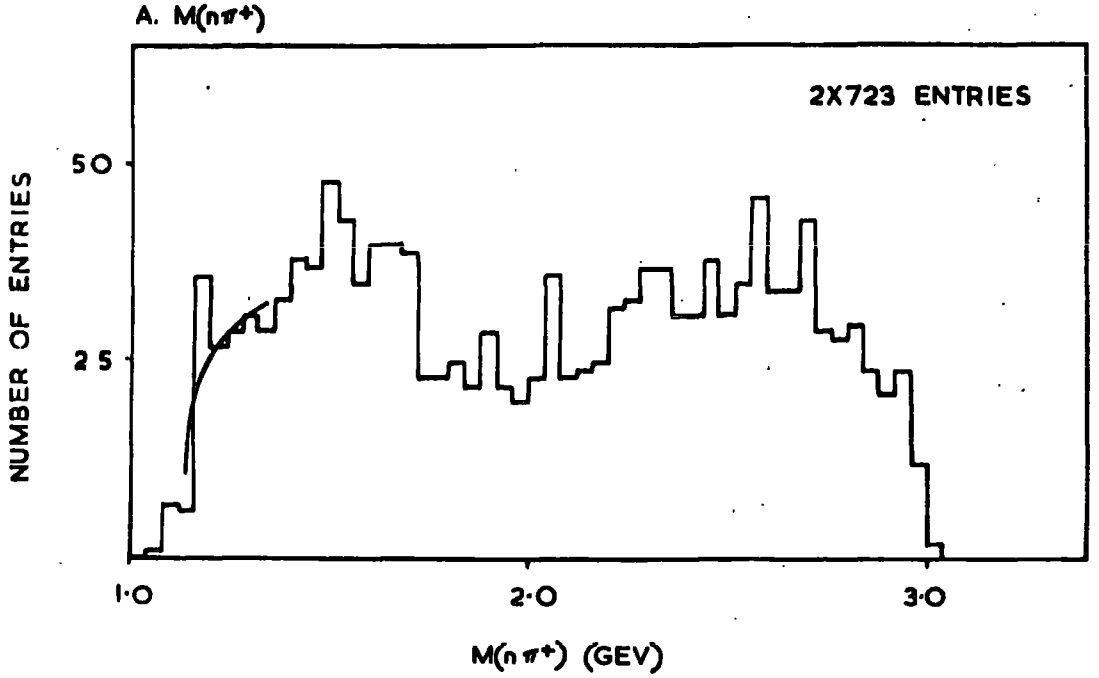


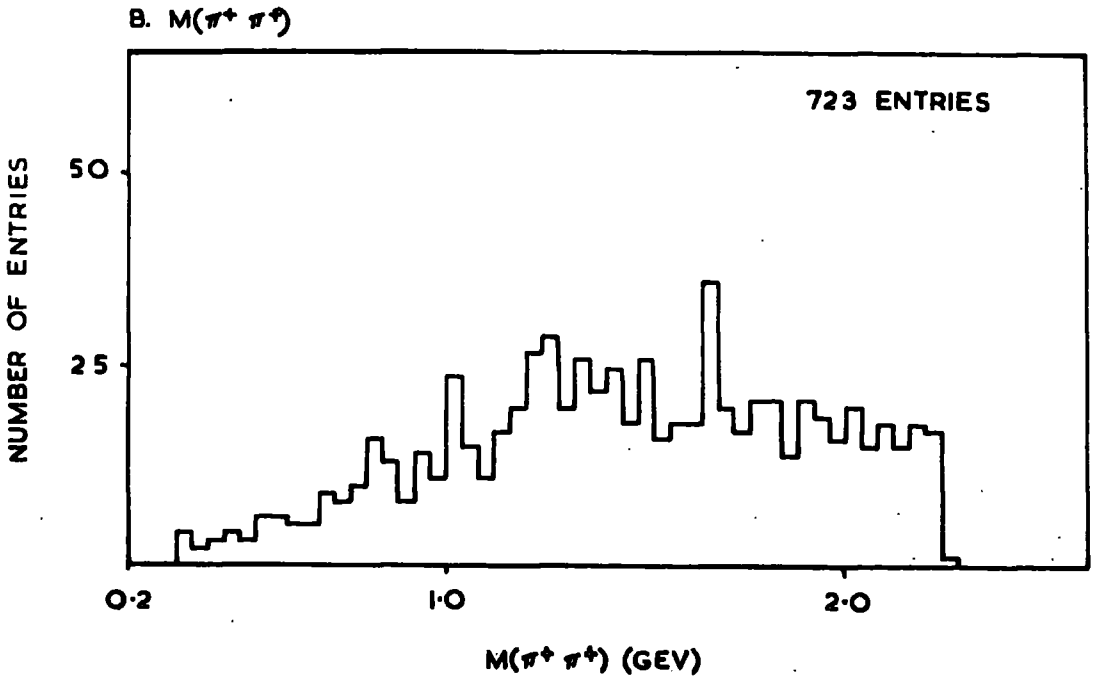

is evident in Fig.(38A), whereas there is only small evidence for $N^{*++}$ production in Figs.(38B) and (40A).

i) Cross section for N* production

The production cross sections have been determined by estimating the excess of events above a smooth background. The problem of estimating the background is a difficult one since Lorentz invariant phase space fails to reproduce the data in low multiplicity interactions due to the conservation of angular momentum and the peripheral nature of the interaction. A possible alternative is to fit the background on either side of the resonance by means of a polynomial. This is difficult in the case of the N* due to its closeness to the $M(p\pi^+)$ threshhold. Consequently, what has been done is to fit the background with a hand drawn curve. The obvious disadvantage of this approach is that it is a subjective one, but the advantage is that the estimated background can be made to agree with the experimental background whilst following the expected general shape of the phase space distribution. Obviously it is only possible to do this if the experimental background in adjacent regions to the resonance is smoothly varying. The uncertainty in this hand drawn background has been allowed for in the calculated cross sections.

The excess of events above the hand drawn background in the $N^{*++}$ peak ($1{\cdot}12 \leq M(p\pi^+) < 1{\cdot}32$ Gev) in Fig.(38A) is

estimated to be 98 ±6. This yields a cross section for the reaction

$$\pi^+ p \rightarrow N^{*++}\ \pi^o \quad ,\quad N^{*++} \rightarrow p\pi^+$$

of 0·10 ±0·01mb or 7·1 ±0·6% of reaction B.

Similar estimations of the excesses in the $N^{*+}$ regions in Figs.(38B) and (40A) give cross sections for the reactions

$$\pi^+ p \rightarrow N^{*+}\ \pi^+ \quad ,\quad N^{*+} \rightarrow p\pi^o \qquad\qquad \pi^+ p \rightarrow N^{*+}\ \pi^+ \quad ,\quad N^{*+} \rightarrow n\pi^+$$

of 0·019 ±0·004mb and 0·011 ±0·002mb respectively.

The ratios of the cross sections

$$\sigma_{N^{*++} \rightarrow p\pi^+} : \sigma_{N^{*+} \rightarrow p\pi^o} : \sigma_{N^{*+} \rightarrow n\pi^+}$$

become

$$9.00 \pm 0.90 : 1.71 \pm 0.36 : 0.99 \pm 0.18$$

which are in good agreement with the ratios of 9 : 2 : 1 expected from the Clebsch Gordon coefficients of isotopic spin.

ii) Mass and width of the $N^{*++}$

The $N^{*++}$ peak has been reproduced in Fig.(38A) by means of a Breit-Wigner function of the form (44)

$$\frac{M}{q} \cdot \frac{\Gamma(M_o)}{(M^2-M_o^2)^2 + M_o^2 \Gamma(M_o)^2}$$

where M is $M(p\pi^+)$ and $\Gamma(M_o)$ is the full width at half height of the resonance. $M_o$ is the value of $M(p\pi^+)$ at the central point, and q is the momentum of the proton (or pion) in the $N^{*++}$ rest system. By varying the values of $M_o$ and $\Gamma(M_o)$ a best fit was obtained with the following values for the central peak and the full width

$$M_o = 1210 \text{ Mev}$$
$$\Gamma(M_o) = 100 \text{ Mev}$$

The value of $M_o$ is some 26 Mev below the generally accepted value of 1236 Mev, and the width is considerably narrower than the expected value of 140 Mev. The shift of $M_o$ is of the same order as that expected from the decay from a P-state where, as shown by Jackson (44), the displacement is given in terms of $\Gamma(M_o)$ and the masses of the decay particles. The deduced shift is ~23 Mev giving a value for the central peak of ~1213 Mev, which agrees well with the present data.

The reduction in the width is indicative of a centrifugal barrier affecting the decay of the resonance. The width should be expressed as a function depending upon $M(p\pi^+)$ which takes the barrier into account. The function proposed by Jackson (44) has the following form

$$\Gamma(M) = \Gamma(M_o)\left[\frac{q}{q_o}\right]^{2\ell+1} \frac{(a.m_\pi^2 + q_o^2)}{(a.m_\pi^2 + q^2)}$$

and is known to work well for the $N^{*++}(1236)$ although it has not, as yet, been tried on the present data.

iii) t-dependence of $N^{*++}$ production

The peripheral nature of the production of the $N^{*++}$ isobar (ie. preference for low four momentum transfer) can be seen in Fig.(41). This shows the Chew Low plot of $M(p\pi^+)$ against the square of the four momentum transfer t from the incident proton to the $p\pi^+$ combination. Most of the $N^{*++}$ events are concentrated below $-t \simeq 0.3$ Gev$^2$. This can also be seen in Fig.(43A) in the Peyrou plot of the centre of mass longitudinal momentum (along the beam direction) against the transverse momentum for events within the $N^{*++}$ region. Since this is a two body process the points must lie on a circle, and it can be seen that the $N^{*++}$ is predominantly produced in the backward direction with consequent low four momentum transfer.

Since the $N^{*++}$ is produced with low four momentum transfer it is worthwhile to examine its production in terms of the peripheral model described in section (1.3.c). Conservation of angular momentum, parity, and G-parity restrict the possible exchange particles to the $\rho^+(760)$ meson (and also its Regge recurrence $g^+(1640)$). Stodolsky and Sakurai (21) proposed a

FIG. 41

# CHEW LOW PLOT OF $M(p\pi^+)$ vs. $t(p/p\pi^+)$ IN REACTION $\pi^+ p \longrightarrow \pi^+ p \pi^0$ AT 5 GEV/c

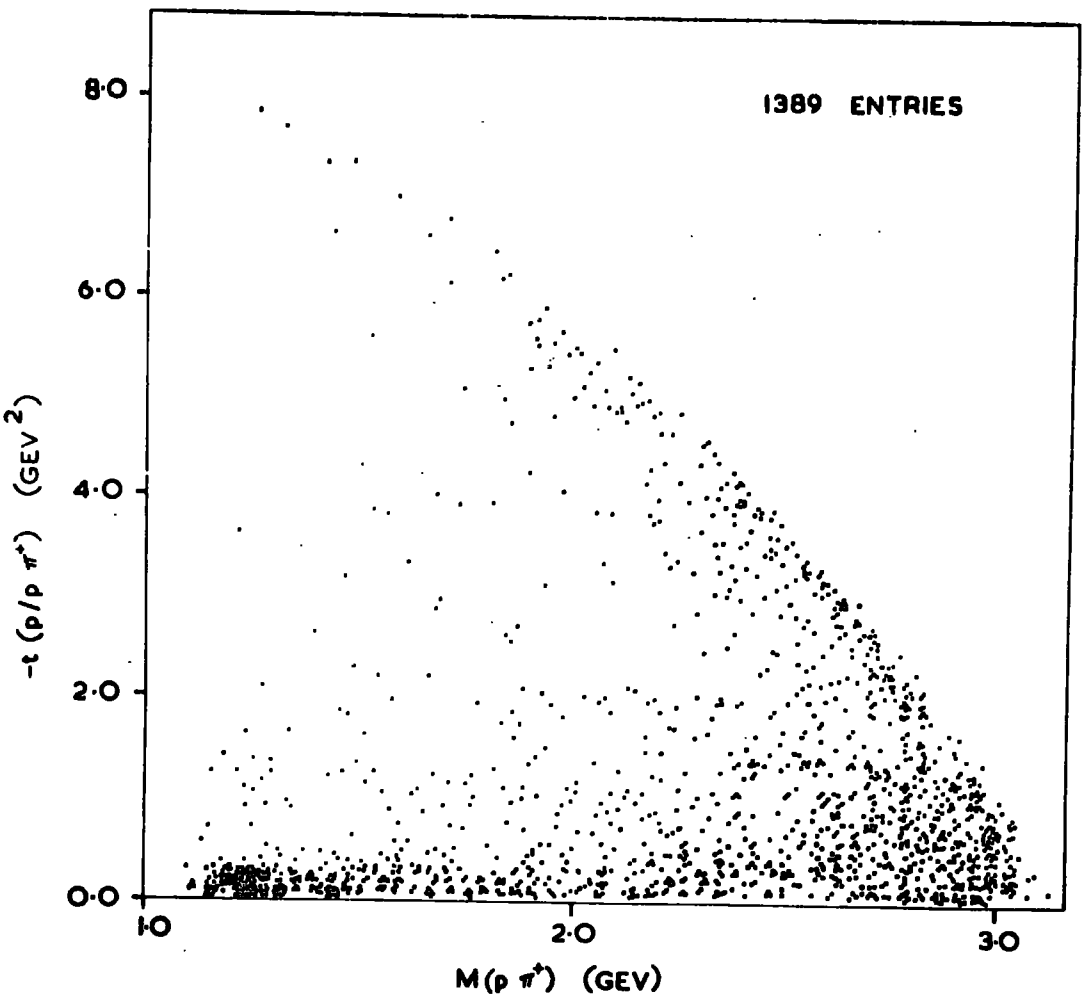

FIG. 42

# CHEW LOW PLOT OF $M(\pi^+\pi^0)$ vs $t(\pi^+/\pi^+\pi^0)$ IN REACTION $\pi^+ p \rightarrow \pi^+ p\, \pi^0$ AT 5 GEV/c

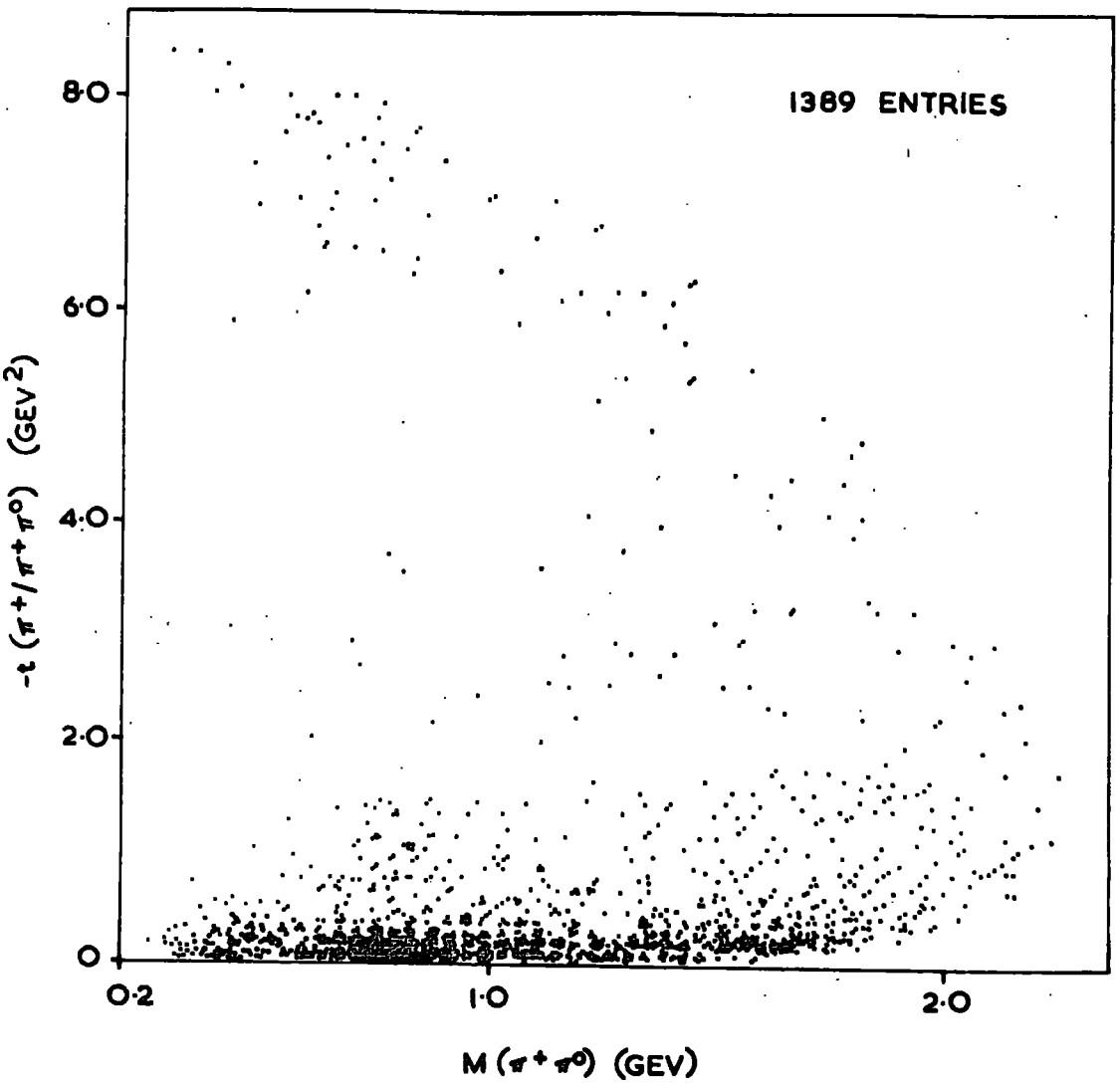

FIG. 43

# PEYROU PLOTS FOR $N^{*++}$ AND $\rho^+$ PRODUCTION IN REACTION $\pi^+ p \rightarrow \pi^+ p \pi^0$ AT 5 GEV/c

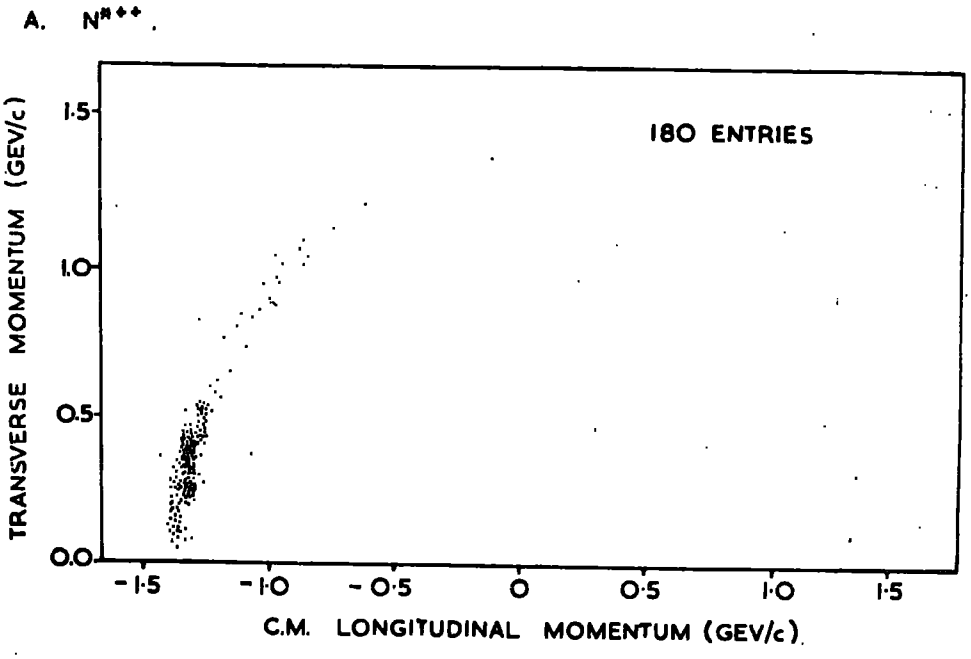


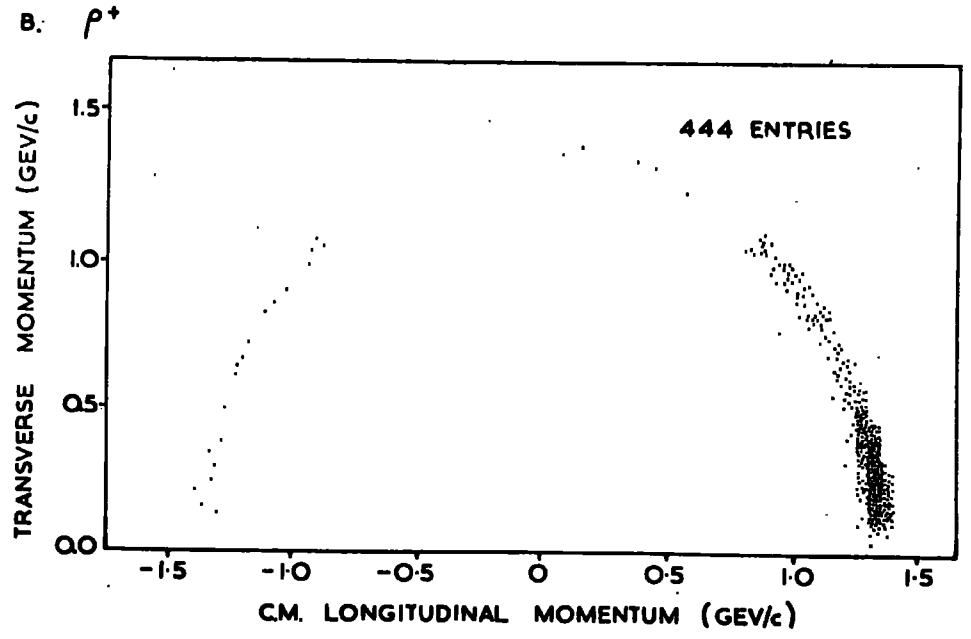

single ρ-exchange model for $N^{*++}$ production in which the pρN* vertex behaves like an M1 electromagnetic transition $N\gamma N^*$ since the $\gamma$ has the same quantum numbers as the ρ meson. Fig.(44) shows the differential cross section ($\delta\sigma/\delta t$) against t for events within the region $1{\cdot}12 \leq M(p\pi^+) < 1{\cdot}32$ Gev, where background events under the $N^{*++}$ peak have been removed by subtracting a normalised distribution of events from the regions adjacent to the $N^{*++}$. It is to be noted that instead of plotting t it would have been more correct to plot $t-t_{min}$, since the minimum four momentum transfer is not zero as in the case for elastic scattering but has a finite value which varies across the resonance. However, the effect is only small and it should not bias the results.

The dotted curve of Fig.(44) shows the prediction of the Stodolsky Sakurai model with absorptive corrections (16), and it is quite obvious that the experimental fall off is far greater than that suggested by the model. In order to fit the data the author has followed the method used at 1·59 Gev/c (45) and 4 Gev/c (46) by introducing a t-dependent form factor F(t) of the form

$$F(t) = \frac{a^2}{(-t + a^2)}$$

The dashed curve in Fig.(44) shows the fit with $a \approx 0{\cdot}28$. The agreement with the experimental distribution is quite good.

FIG. 44

$d\sigma/dt$ vs. t DISTRIBUTION FOR $N^{*++}$ PRODUCTION IN REACTION $\pi^+ p \rightarrow \pi^+ p \pi^0$ AT 5 GEV/c

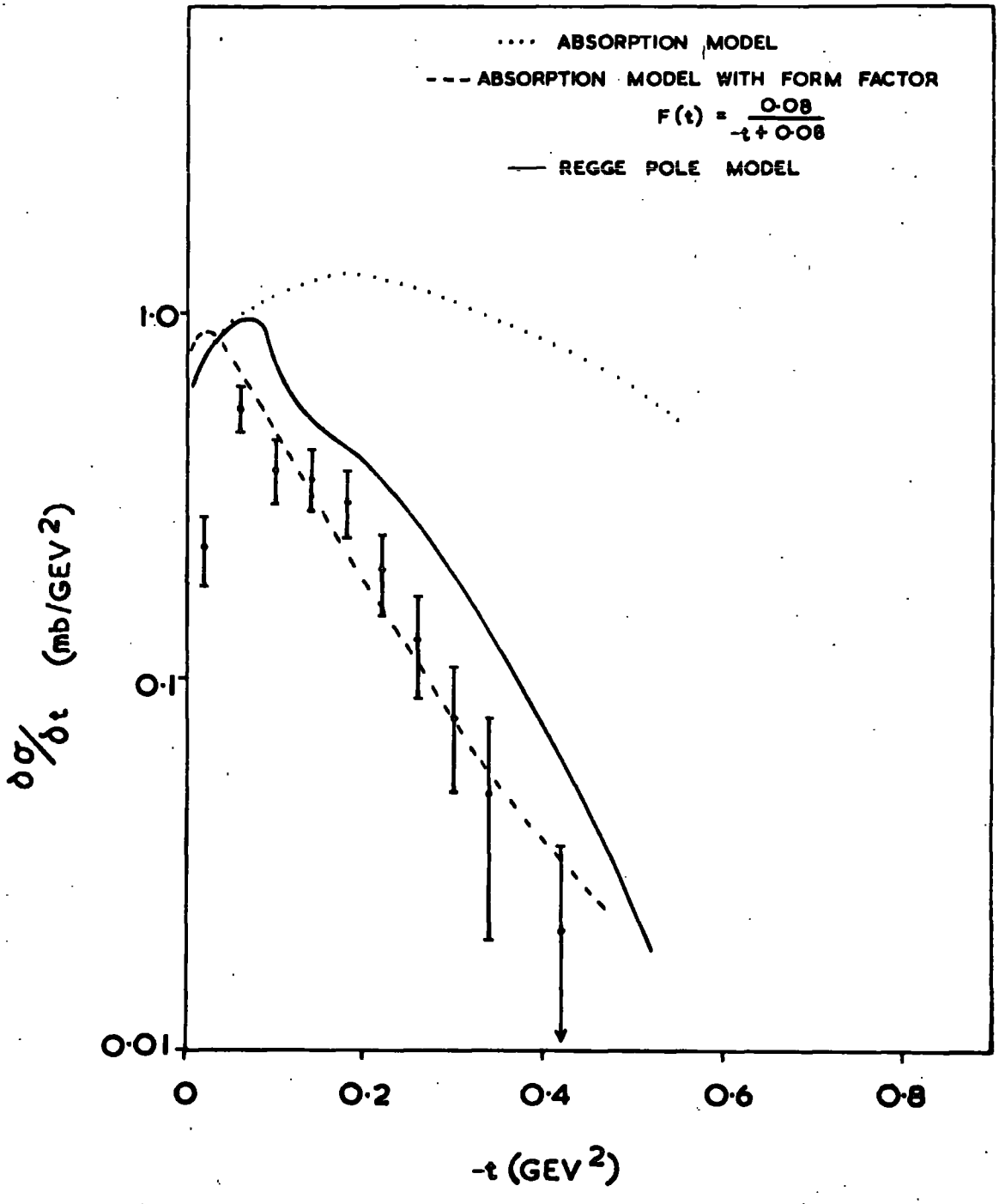

FIG. 45

$d\sigma/dt$ vs. $t$ DISTRIBUTION FOR $\rho^+$ PRODUCTION IN REACTION $\pi^+ p \rightarrow \pi^+ p\, \pi^0$ AT 5 GEV/c

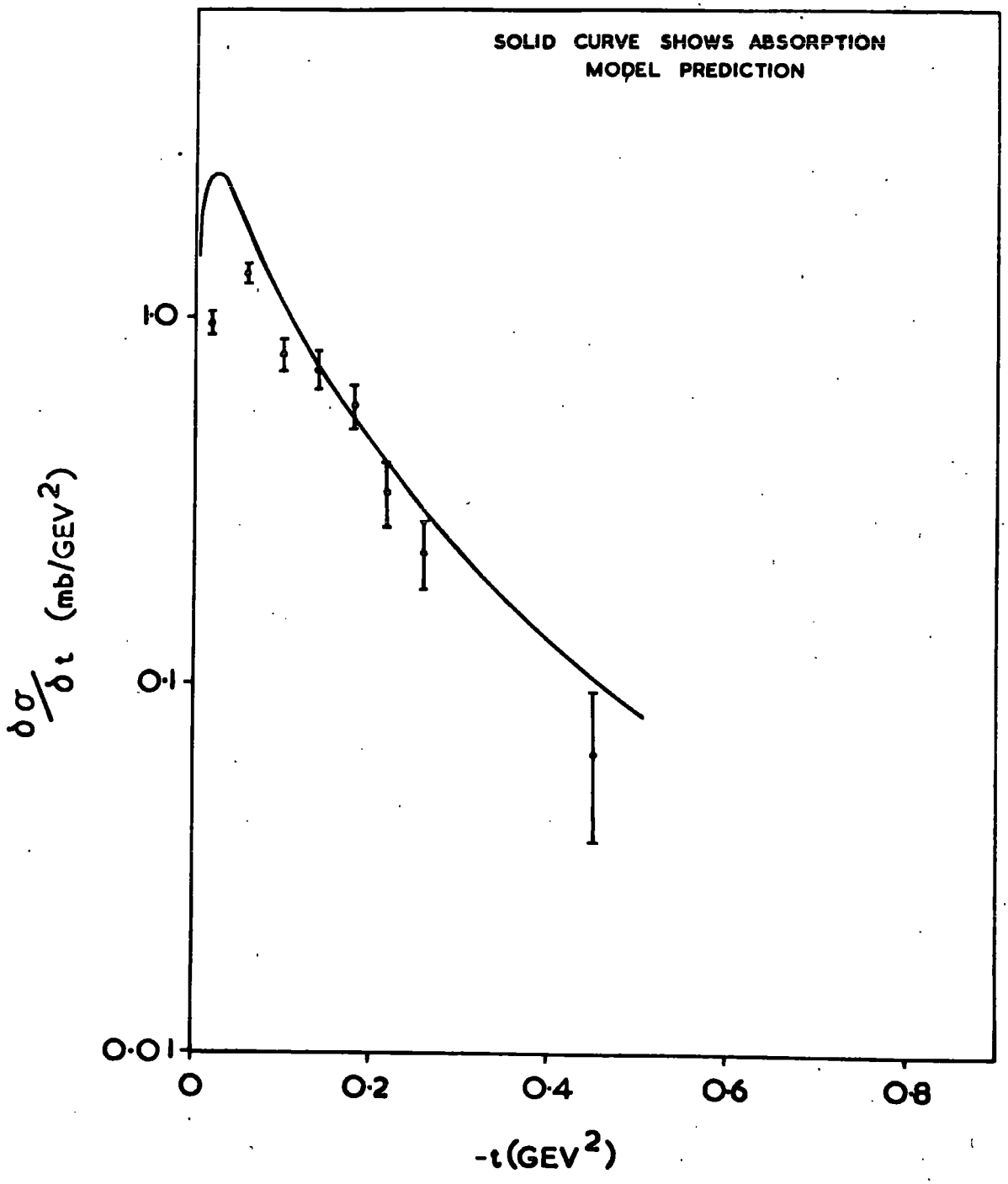

However, as has been pointed out in many previous publications, different form factors are required to make the fit at different primary energies. Furthermore, the model predicts an increasing cross section for $N^{*++}$ production whereas experimentally the cross section falls rather rapidly with increasing primary energy.

Consequently, the absorption model with form factors has doubtful significance when fitted to differential cross sections, at least for vector meson exchange processes.

The solid curve of Fig.(44) shows the Regge pole model prediction, taken from the work of Thews (47), assuming $\rho$ trajectory exchange. Thews has fitted the reaction $\pi^+ p \rightarrow N^{*++} \pi^0$ at 2·75, 3·54, 4·0, and 8·0 Gev/c with remarkable success. However, in the present data at 5 Gev/c the Regge prediction, although reproducing the experimental data qualitatively, fails to give good quantitative agreement. Nevertheless, the fit is very close considering the failure of the absorption model. The dip in the differential cross section at $-t \approx 0{\cdot}1$ Gev$^2$, which is also seen at the energies above, comes directly from the Regge pole model in that there is a nonsense coupling for the $\rho$ trajectory ($\alpha_\rho$) when $\alpha_\rho = 0$. The reaction amplitude becomes zero giving rise to an energy independent dip for t values corresponding to $\alpha_\rho = 0$.

iv) Decay angular distributions of the $N^{*++}$

Unfortunately the Regge pole model gives little information about decay angular distributions, consequently it is necessary to return to the Stodolsky Sakurai model (with absorptive corrections) which prdicts values for the elements $\rho_{mm'}$ of the decay density matrix (cf. section (1.3.c)). In terms of the elements of the $N^{*++}$ density matrix the angular distribution of the $N^{*++}$ decay should have the form

$$W(\cos\theta) = \frac{1}{4}\left[(1 + 4\rho_{33}) + (3 - 12\rho_{33})\cos^2\theta\right]$$

$$W(\phi) = \frac{1}{2\pi}\left[(1 + \frac{4}{\sqrt{3}}\,\mathrm{Re}\rho_{3,-1}) - \frac{8}{\sqrt{3}}\,\mathrm{Re}\rho_{3,-1}\cos^2\phi\right]$$

where $\theta$ and $\phi$ are the Jackson angles of the decaying resonance in its own rest system, and are defined in Fig.(3B). In order to purify the sample of $N^{*++}$ events only those have been used with four momentum transfer less than 0·3 $Gev^2$. Fig.(46A) shows the distributions of $\cos\theta$ and $\phi$ for the $N^{*++}$. Background events have been subtracted from these plots in the manner described previously, and the overlap of the $N^{*++}$ and $\rho^+$ bands has been repopulated with events in adjacent regions so as to avoid any distortions due to the decay angular distribution of the $\rho^+$ itself.

The solid curves show least squares fits of the form $A+B\cos^2\theta$ and $A+B\cos^2\phi$ respectively. From these fits the

FIG. 46

JACKSON ANGULAR DISTRIBUTIONS AT 5 GEV/c

[THE SOLID CURVES SHOW THE FITS $A+B\cos^2\theta$ AND $A+B\cos^2\phi$]

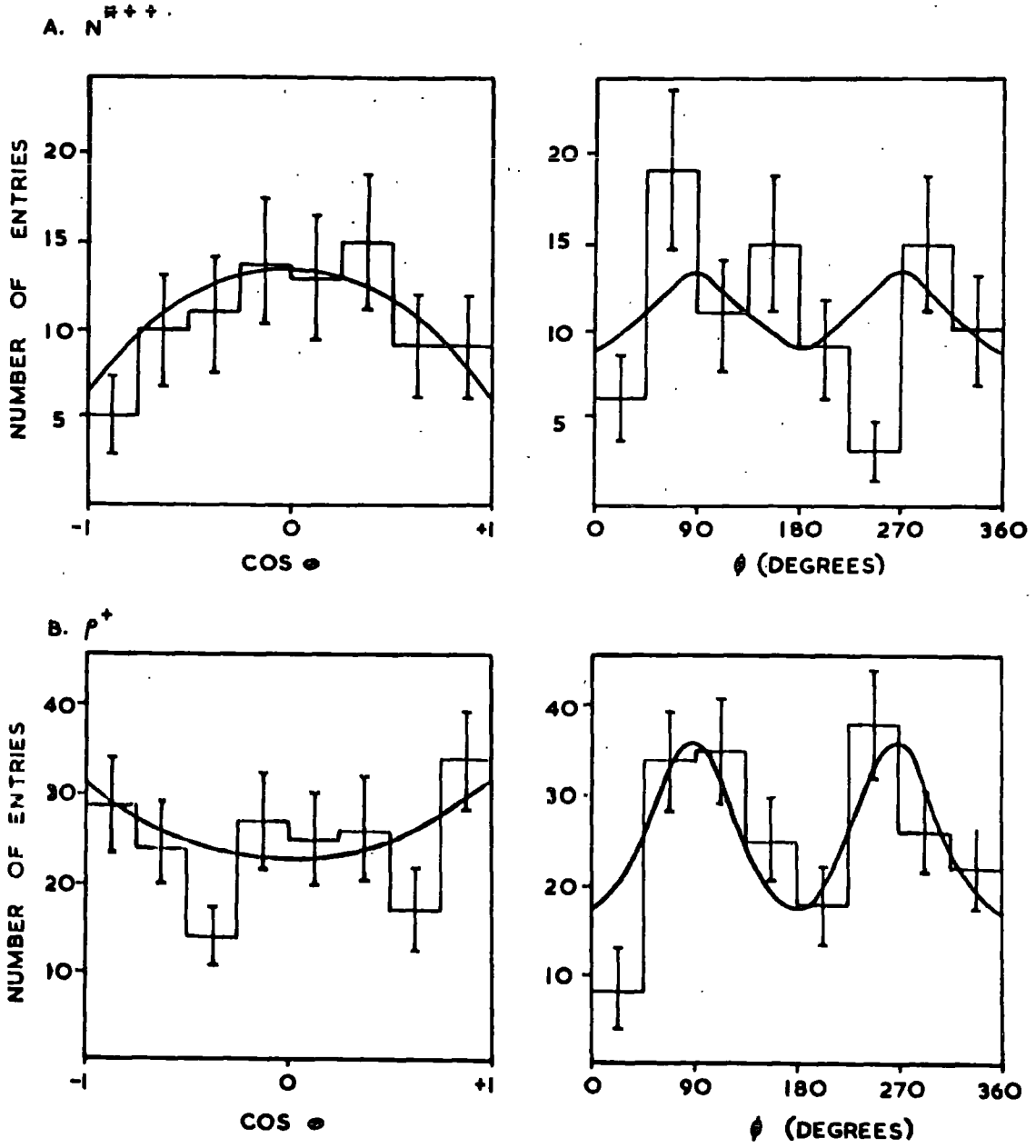

following values for the density matrix elements were obtained for $-t < 0{\cdot}3$ Gev$^2$ :

$$\rho_{33} = 0{\cdot}36 \pm 0{\cdot}04 \qquad \rho_{3,-1} = 0{\cdot}07 \pm 0{\cdot}06$$

The absorptive corrections to the simple peripheral model produce an energy and t dependence of the density matrix elements, consequently the above values are considered to be averaged over the t interval of $0{\cdot}3$ Gev$^2$. The value of $\rho_{33}$ is in good agreement with the model prediction of $\sim 0{\cdot}32$, whereas the value of $\rho_{3,-1}$ is in poor agreement with the model prediction of $0{\cdot}21$. Table (20) in the Conclusion part of this chapter lists the values of the density matrix elements at energies from 4 to $11{\cdot}5$ Gev/c.

c) $\rho^+(760\text{Mev})$ production

$\rho^+(760)$ meson production can be seen in the Dalitz plot of the effective masses $M(p\pi^+)$ and $M(\pi^+\pi^o)$ in Fig.(35). It gives a clear resonant signal in the projection onto the $M(\pi^+\pi^o)$ axis in Fig.(39A). The background under the resonant peak has again been estimated by means of a hand drawn curve.

i) Cross section for $\rho^+$ production

The excess of events under the $\rho^+$ peak ($0{\cdot}64 \leqslant M(\pi^+\pi^o) < 0{\cdot}92$ Gev) in Fig.(39A) above the hand drawn background is estimated to be $200 \pm 14$ giving a cross section for the reaction

$$\pi^+ p \rightarrow \rho^+ p$$
$$\hookrightarrow \pi^+ \pi^o$$

of 0·20 ±0·02mb or 14·1 ±1·4% of reaction B

Combining this cross section with that for N* production indicates that 24·8% of events in the final state reaction $\pi^+ p \rightarrow \pi^+ p \pi^o$ go through an intermediate quasi-two-body stage.

ii) Mass and width of the $\rho^+$

The $\rho^+$ peak in Fig.(39A) has been reproduced by the Breit-Wigner function as used for the $N^{*++}$ in section (5.3. b(ii)). The best fit was obtained with values for the central peak and width of

$$M_o = 770 \text{ Mev}$$
$$\Gamma(M_o) = 140 \text{ Mev}$$

which are in reasonable agreement with known values.

iii) t-dependence of $\rho^+$ production

From the Chew Low plot of $M(\pi^+ \pi^o)$ against the square of the four momentum transfer t in Fig.(42) and the Peyrou plot of the centre of mass longitudinal momentum of the $\rho^+$ against the transverse momentum in Fig.(43B), the peripheral nature of the production of the $\rho^+$ is clearly marked. There is also evidence for very anti-peripheral production which may be due to the exchange of a baryon (neutron in this case) in the u channel.

In treating the reaction with the peripheral model the only possible exchange particles are the $\pi$, $\omega$, and $A_2$ mesons. If only a pion is exchanged the absorption model predicts a cross section of $\sim 0.3$mb (48) which is in fair agreement with the value obtained of 0.2mb.

Fig.(45) shows the differential cross section for events within the region $0.64 \leq M(\pi^+\pi^0) < 0.92$ Gev, where once again background events within the $\rho^+$ region have been removed by subtracting distributions from the adjacent regions. The solid curve shows the prediction of the absorptive peripheral model (16) for single pion exchange. The agreement is remarkably good considering the failure of the $\rho$ exchange model to reproduce the $N^{*++}$ differential cross section. The model also gives reasonable fits at 2.75, 4, and 8 Gev/c.

iv) Decay angular distributions of the $\rho^+$

In terms of the elements of the $\rho^+$ density matrix the angular distribution of the $\rho^+$ decay should have the form

$$W(\cos\theta) = \frac{3}{4}\left[(1 - \rho_{00}) + (3\rho_{00} - 1)\cos^2\theta\right]$$

$$W(\phi) = \frac{1}{2\pi}\left[(1 + 2\rho_{1,-1}) - 4\rho_{1,-1}\cos^2\phi\right]$$

The $\rho^+$ sample has been purified by taking only events with four momentum transfer from proton to proton less than 0.3 $Gev^2$, and the background events under the $\rho^+$ peak have been

removed in the usual manner.

Fig.(46B) shows the distributions of $\cos\theta$ and $\phi$ for the $\rho^+$ with least squares fits of the form $A+B\cos^2\theta$ and $A+B\cos^2\phi$. From these fits the following values for the density matrix elements have been obtained for $-t < 0{\cdot}3$ Gev$^2$

$$\rho_{00} = 0{\cdot}48 \pm 0{\cdot}08 \qquad \rho_{1,-1} = 0{\cdot}19 \pm 0{\cdot}04$$

The value of $\rho_{1,-1}$ is in good agreement with the absorptive model prediction of 0·17, but the value of $\rho_{00}$ is a little below the prediction of $\sim 0{\cdot}65$. However, the absorption model for one pion exchange in the reaction $\pi^+p \rightarrow \rho^+p$ seems to give quite a fair description of the experimental data.

A further test of one pion exchange is that proposed by Treiman and Yang (20) where, in the incident pion rest system, there should be no correlation between the plane of the decay pions from the $\rho^+$ and the plane of the incoming and outgoing protons if a spinless pion is exchanged. Fig.(48A) shows the Treiman Yang angle for this reaction and it is evident that the distribution is not really consistent with isotropy. This is to be expected of course if there are initial and final state interactions as suggested by the absorption model.

v) $\pi^+\pi^o$ scattering cross section

An attempt has been made to determine the $\pi^+\pi^o$ scattering cross section using the extrapolation method of Chew and Low

(10) and following closely the work of Baton et al (49) where the $\pi^-\pi^o$ cross section has been determined in the reaction $\pi^-p \rightarrow \pi^-p\pi^o$ at 2·77 Gev/c.

Assuming that the reaction $\pi^+p \rightarrow \pi^+p\pi^o$ proceeds by one pion exchange Chew and Low suggest the construction of the following function

$$F(w,t) = \frac{-2\pi}{f^2} \cdot \frac{k^2(lab)}{w\sqrt{\frac{w^2}{4}-\mu^2}} \cdot (t-\mu^2)^2 \frac{\delta^2\sigma}{\delta t \delta w^2}$$

where w is the $\pi^+\pi^o$ centre of mass energy $M(\pi^+\pi^o)$, $f^2$ is the $\pi^op$ coupling constant ($\approx 0{\cdot}08$), k(lab) is the incident pion momentum, t is the square of the four momentum transfer to the proton, $\mu$ is the mass of the exchanged pion, $\sqrt{\frac{w^2}{4}-\mu^2}$ is the relative momentum of the pions in their centre of mass, $(t-\mu^2)$ is the usual propagator term for one pion exchange, and $\delta^2\sigma/\delta t\delta w^2$ is the experimental differential cross section.

For a fixed value of $w^2$, if $\delta^2\sigma/\delta t\delta w^2$ is extended to negative values of four momentum transfer it has a pole at $-t = -\mu^2$, where the value of $-F(w,t)$ is directly related to the scattering cross section of the incident $\pi^+$ on the exchanged $\pi^o$. Obviously this is only true at the unphysical point $-t = -\mu^2$, that is when the exchanged pion is 'on the mass shell'. The method of Chew and Low is to construct $-F(w,t)$ in the physical region and then extrapolate to $-t = -\mu^2$ to determine

the $\pi^+\pi^o$ scattering cross section from the expression

$$F(w,t) \longrightarrow \frac{t}{\mu^2}\,\sigma(\pi^+\pi^o) \qquad \text{as} \quad -t \rightarrow \mu^2$$

Baton et al have shown that for the reaction $\pi^-p \rightarrow \pi^-p\pi^o$ the function $F(w,t)$ goes through zero at $-t = 0$ as expected for one pion exchange. Moreover, they have shown that for $-t < 13\mu^2$ the function $F(w,t).\mu^2/t$ is linear and so can be extrapolated to $-t = \mu^2$ to give $\sigma(\pi^-\pi^o)$ directly.

In this experiment the statistics are limited at present to about one fifth of those of Baton et al. However, if the linear extrapolation of $F(w,t).\mu^2/t$ is still valid it is possible to determine $\sigma(\pi^+\pi^o)$ by calculating only two values of $F(w,t).\mu^2/t$. Table (17) shows the analysis data while Fig. (47) shows the linear extrapolations for six intervals of w, the intercepts of which give the values of $\sigma(\pi^+\pi^o)$. The plot of w against the $\pi^+\pi^o$ cross section is shown in Fig.(48B). The horizontal error bars in both figures represent the intervals chosen.

Although the errors are large and assumptions have been made, it can be seen that the scattering cross section passes through a resonance ($w \geqslant 12\pi\lambda\!\!\!^{-2}$) at the $\rho^+$ mass. Unfortunately it has been impossible to determine values for $\sigma(\pi^+\pi^o)$ well below the resonant point due to the assymptotic behaviour of the function $\sqrt{\frac{w^2}{4}-\mu^2}$.

FIG. 47

LINEAR EXTRAPOLATIONS OF THE FUNCTION $-F(\omega,t) \times \mu^2/t$ vs. $t/\mu^2$ IN REACTION $\pi^+ p \rightarrow \pi^+ p \pi^0$ AT 5 GEV/c

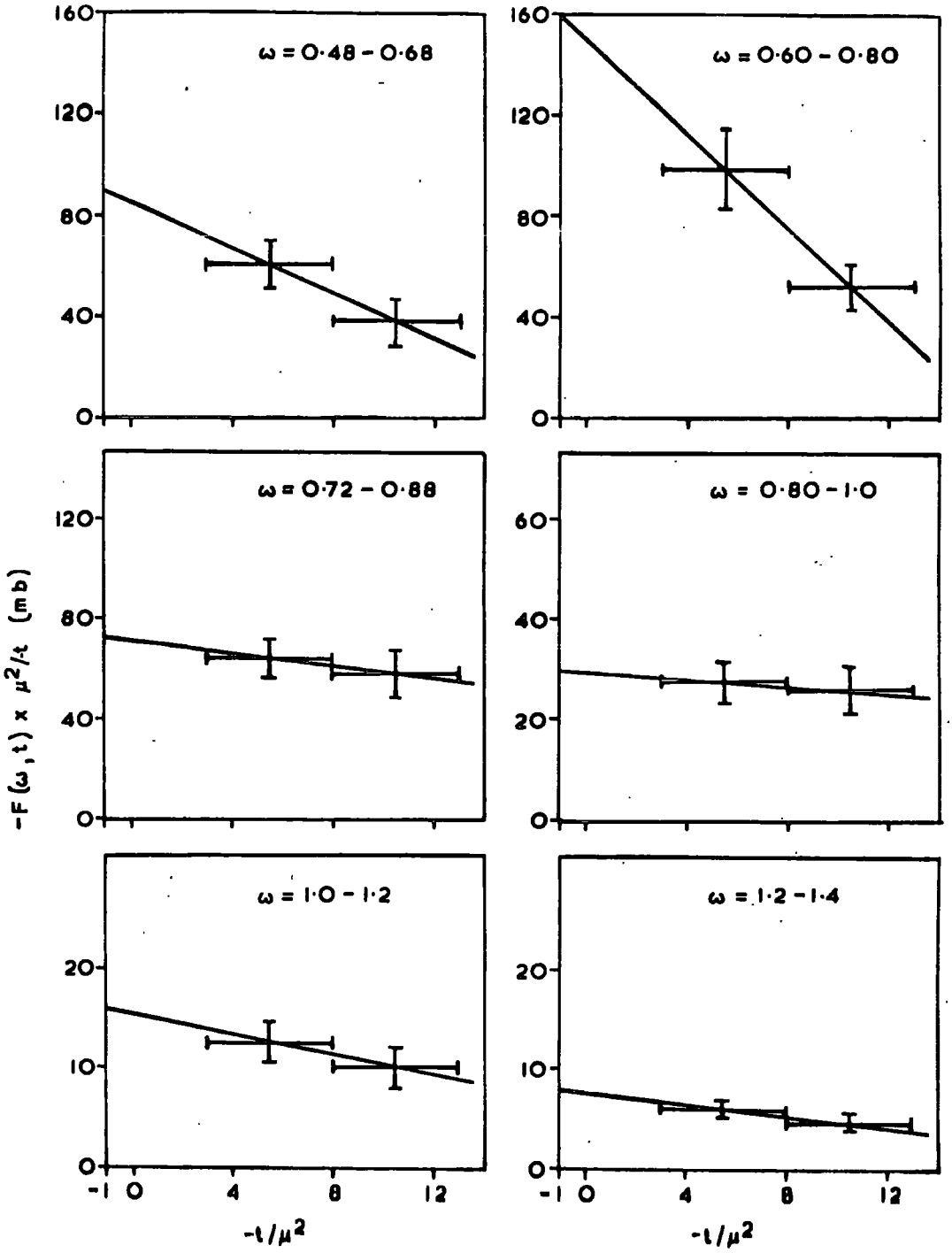

FIG. 48

# TREIMAN YANG ANGLE ($\theta$ TY) AND $\sigma(\pi^+\pi^0)$ IN REACTION $\pi^+p \rightarrow \pi^+p\pi^0$ AT 5 GEV/c

A. TREIMAN YANG ANGLE FOR $\rho^+\left[t < 0.3 \text{ GEV}^2\right]$

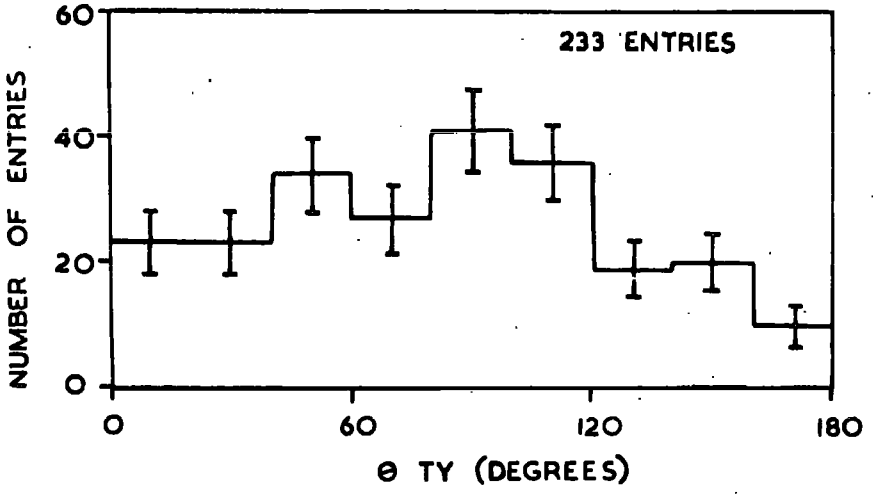


B. $\sigma(\pi^+\pi^0)\left[t < 0.26 \text{ GEV}^2\right]$

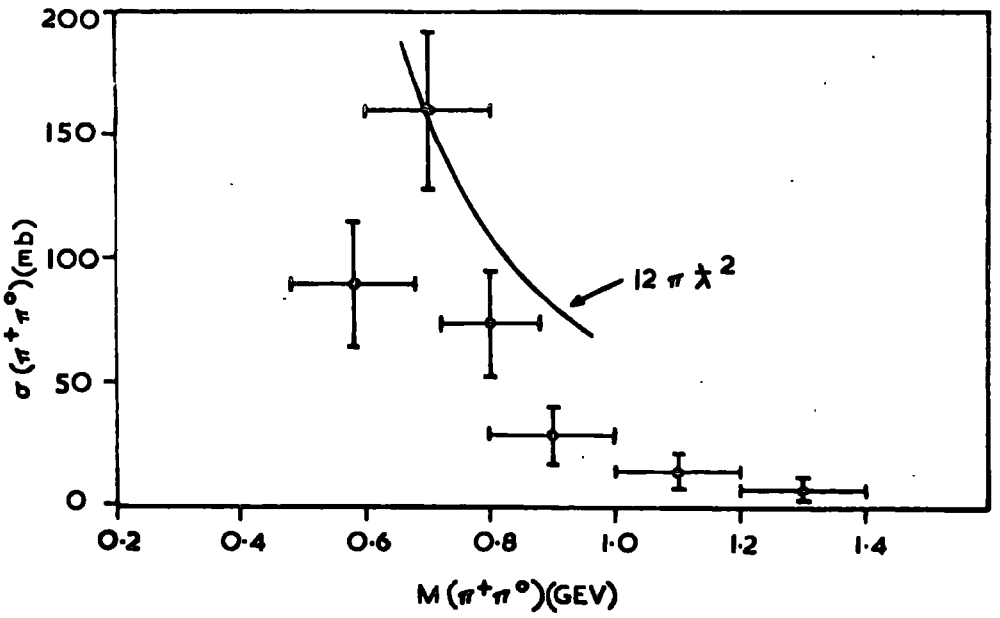

TABLE 17

Linear extrapolations made to obtain $\sigma(\pi^+\pi^o)$

| $\pi^+\pi^o$ mass interval (Gev) | Interval of $-t/\mu^2$ | $-F(w,t).\mu^2/t$ (mb) | $\sigma(\pi^+\pi^o)$ (mb) |
|---|---|---|---|
| 0·48-0·68 | 3·0-8·0<br>8·0-13·0 | 59·5 ±9·6<br>37·6 ±9·2 | 90·0 ±22·9 |
| 0·60-0·80 | " | 98·5 ±15·0<br>51.8 ±8·1 | 160·1 ±32·2 |
| 0·72-0·88 | " | 63·0 ±7·2<br>57·9 ±9·7 | 73·0 ±22.1 |
| 0·80-1·00 | " | 26·2 ±4·5<br>25·3 ±4·7 | 28·5 ±12·3 |
| 1·00-1·20 | " | 12.6 ±2.1<br>10·1 ±2·5 | 15·0 ±5·0 |
| 1·20-1·40 | " | 6·0 ±1·0<br>4·8 ±1·0 | 8·1 ±3·2 |

It is to be noted that most calculations performed have been for $\sigma(\pi^-\pi^o)$ rather than $\sigma(\pi^+\pi^o)$. This is because of the presence of the $N^{*++}$ resonance, which is normally produced with low four momentum transfer to the proton. Consequently it is likely that events of the type $\pi^+p \rightarrow N^{*++}\pi^o$ can contaminate the sample. In contrast, $N^{*+}$ production in the reaction $\pi^-p \rightarrow \pi^-p\pi^o$ is negligible.

The effect of $N^{*++}$ production in the present data should not be too significant because it represents only 7·1% of reaction B. However, its effect would be to increase the lower values

of $t/\mu^2$ which would in turn lead to higher intercept values in Fig.(47) and higher values of $\sigma(\pi^+\pi^o)$. In fact it can be seen in Fig.(48B), compared with Baton's work, that the cross section values are some 30mb higher.

## 5.4 5 Gev/c NO FIT reaction D

In selecting a sample of the NO FIT reaction D, $\pi^+p \rightarrow \pi^+p\pi^o$ $(m\pi^o)$ $m \geq 1$, only events have been taken where the proton could definitely be identified on the scanning table.

Fig.(49A) shows the effective mass distribution $M(p\pi^+)$ where the $N^{*++}(1236)$ isobar can be seen to be produced abundantly. The number of events above the hand drawn background in the region $1{\cdot}12 \leq M(p\pi^+) < 1{\cdot}32$ Gev is estimated to be 249 $\pm$16 representing a cross section for the reaction

$$\pi^+p \rightarrow N^{*++} + \text{neutrals}$$
$$\hookrightarrow p\pi^+$$

of $0{\cdot}24 \pm 0{\cdot}02$mb. The central peak value and width are estimated to be

$$M_o = 1215 \text{ Mev}$$
$$\Gamma(M_o) = 110 \text{ Mev}$$

which are in good agreement with the values obtained for the $N^{*++}$ in reaction B.

The missing mass (MM) for reaction D is shown in Fig.(49B)

FIG. 49

M($p\pi^+$) AND MISSING MASS (MM) IN REACTION (D)

$\pi^+ p \rightarrow \pi^+ p \pi^0$ ($m\pi^0$) $m \geq 1$ AT 5 GEV/c

A. M($p\pi^+$)

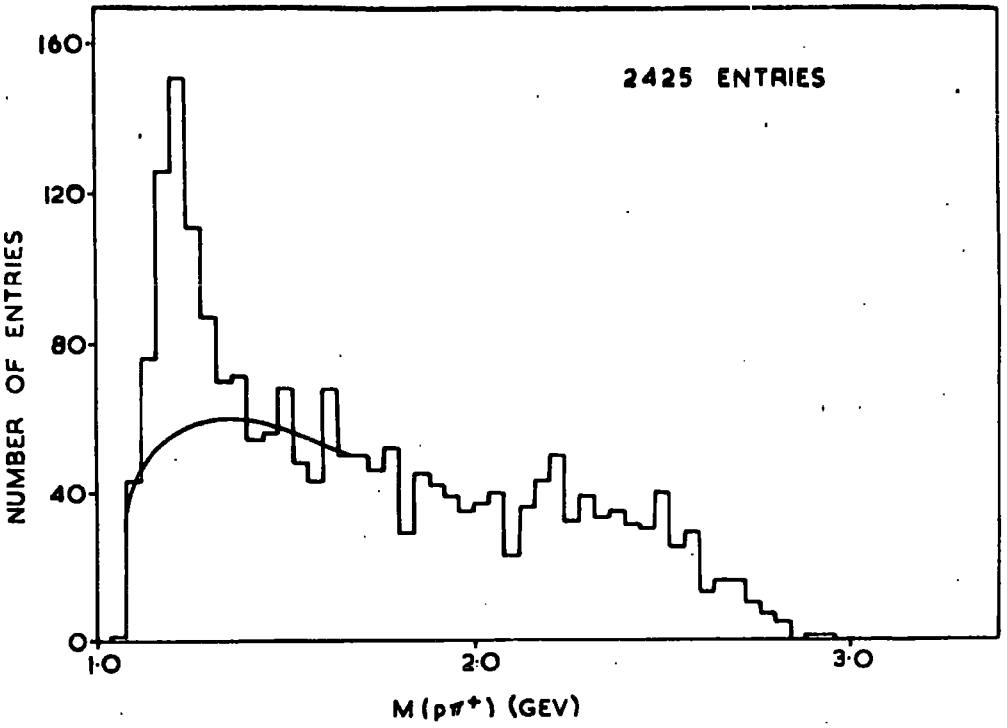


B. MM

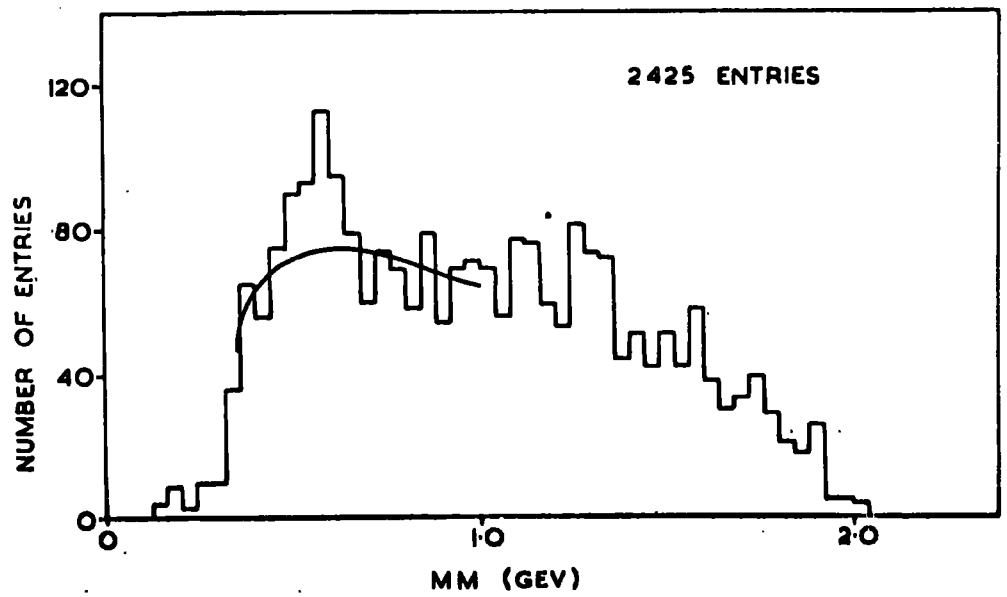

where it can be seen that there is a significant enhancement around MM≈ 560 Mev corresponding to the $\eta^{o}(550)$ meson. The known width of the $\eta^{o}$ is ~0·003 Mev whereas in Fig.(49B) the width is ~120 Mev. This is due to the experimental error which introduces an error of ~50 Mev on a resonant mass in a one constraint fit. In a NO FIT this constraint is removed and the error is considerably larger. In the $\eta^{o}$ region, 0·48 ≤ MM < 0·64 Gev, 94 ±8 events have been counted above the hand drawn background giving a cross section for the reaction

$$\pi^{+}p \rightarrow \eta^{o}\ \pi^{+}\ p$$
$$\qquad\qquad\quad \hookrightarrow \text{neutrals}$$

of 0·09 ±0·01mb.

The cross section obtained at this energy in the four prong interactions (50) for the reaction

$$\pi^{+}p \rightarrow \pi^{+}p\,\eta^{o}$$
$$\qquad\qquad\quad \hookrightarrow \pi^{+}\pi^{-}\pi^{o}$$

was 0·040 ±0·003mb which leads to the branching ratio

$$\frac{(\eta^{o} \rightarrow \text{neutrals})}{(\eta^{o} \rightarrow \text{charged})} = 2{\cdot}2 \pm 0{\cdot}3$$

which is in good agreement with values obtained at other energies. Also in Fig.(49B) there is a possible enhancement in the region of MM≈ 1300 Mev corresponding to the $f^{o}$(1260 Mev, $J^{P}=2^{+}$).

However, the background is uncertain in this region and it is not possible to deduce a cross section.

The missing mass (MM) is again shown in Fig.(5OA) but this time with the restriction that $M(p\pi^+)$ must lie in the range $1{\cdot}12 \leq M(p\pi^+) < 1{\cdot}32$ Gev. The $\eta^o$ signal is again clear and also the $f^o$ signal has improved considerably. The numbers of events in the $\eta^o$ and $f^o$ peaks above the smoothly drawn background are $22 \pm 3$ and $33 \pm 3$ respectively, giving cross sections for the processes

$$\pi^+ p \rightarrow N^{*++} + \eta^o \quad (N^{*++} \rightarrow p\pi^+ ; \ \eta^o \rightarrow \text{neutrals})$$

$$\pi^+ p \rightarrow N^{*++} + f^o \quad (N^{*++} \rightarrow p\pi^+ ; \ f^o \rightarrow \text{neutrals})$$

of $0{\cdot}021 \pm 0{\cdot}003$mb and $0{\cdot}031 \pm 0{\cdot}004$mb respectively. Unfortunately the numbers of events are too low to allow investigation of the t-dependence of these reactions.

In order to search for the decays of positively charged pion resonances into $\pi^+$+neutrals, the appropriate effective mass distribution has been plotted with $M(p\pi^+)$ outside the $N^{*++}$ region in Fig.(5OB). Although the statistical fluctuations are large there is a two standard deviation enhancement at the mass of the $A_2$(1300Mev) meson above the hand drawn background. However, there is no evidence for the $A_1$. In order to

FIG. 50

MM AND M($\pi^+$+MISSING NEUTRALS) IN REACTION (D).
$\pi^+p \rightarrow \pi^+p\pi^0$ ($m\pi^0$) $m \geq 1$ AT 5 GEV/c

A. MM [ M($p\pi^+$) IN $N^{*++}$]

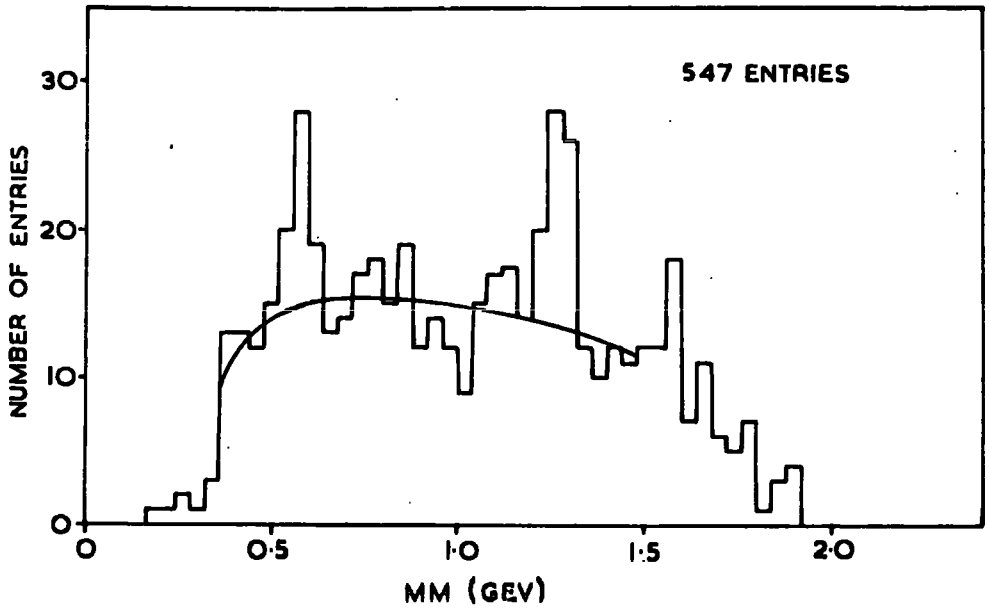


B. M ($\pi^+$+ NEUTRALS) [M($p\pi^+$) NOT IN $N^{*++}$]

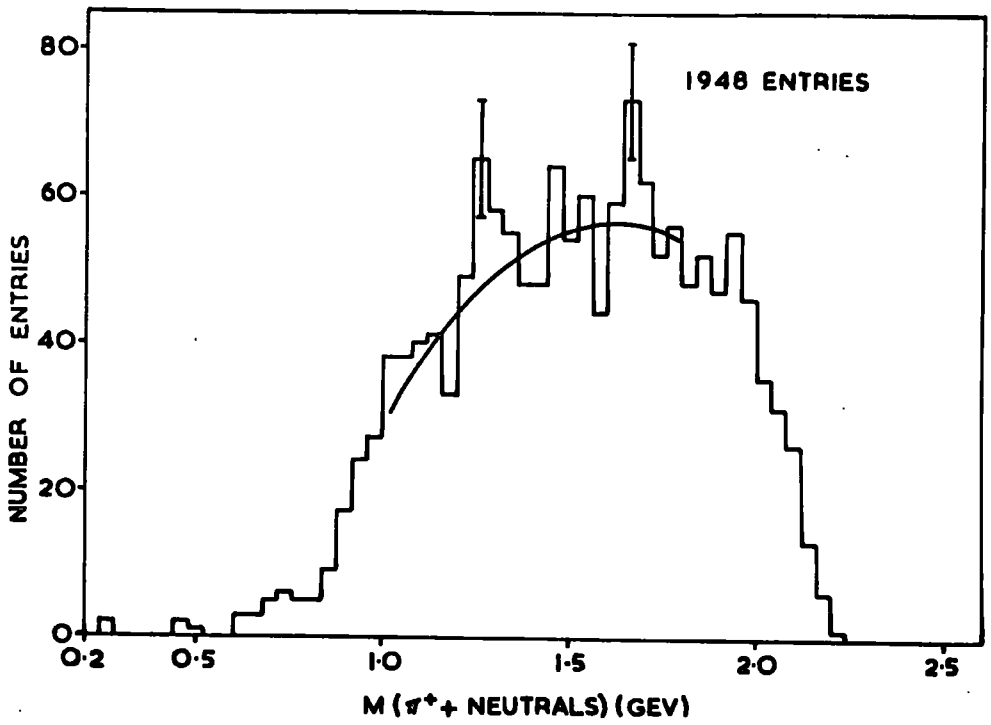

investigate the decay mode

$$A_2 \rightarrow \eta^0 + \pi^+$$
$$\eta^0 \hookrightarrow \text{neutrals}$$

the effective mass of the $\pi^+$+neutrals was plotted for events with MM in the $\eta^0$ region. Unfortunately there was no enhancement in the $A_2$ region. This is not so surprising in view of the fact that the $A_2$ decays to $\rho\pi$ in 85% of the cases.

Also in Fig.(50B) there is a two standard deviation enhancement in the region of 1650 Mev. The only known meson resonance in this region decaying to $\pi^+$+neutrals is the possible $A_3$(I=1, $J^P$ unknown) meson resonance at 1640 Mev which has a dominant $3\pi$ decay mode. This resonance has been reported several times, in particular by Ioffredo (51) in the $\pi^+\pi^-\pi^-$ spectrum of a deuterium experiment and by the author's collaborators in the four prong analysis at 11·5 Gev/c (52) in the $\pi^+\pi^+\pi^-$ spectrum. However, the signal to noise ratio is too small to make any critical examination of this enhancement possible in the present data.

## 5.5 11·5 Gev/c inelastic 1C reactions

### a) Contamination in the sample

Fig.(51) shows the Dalitz plot of the effective masses $M(p\pi^+)$ and $M(\pi^+\pi^0)$ in reaction B. The striking features are the unexpected excesses of events in two distinct regions:

FIG. 51

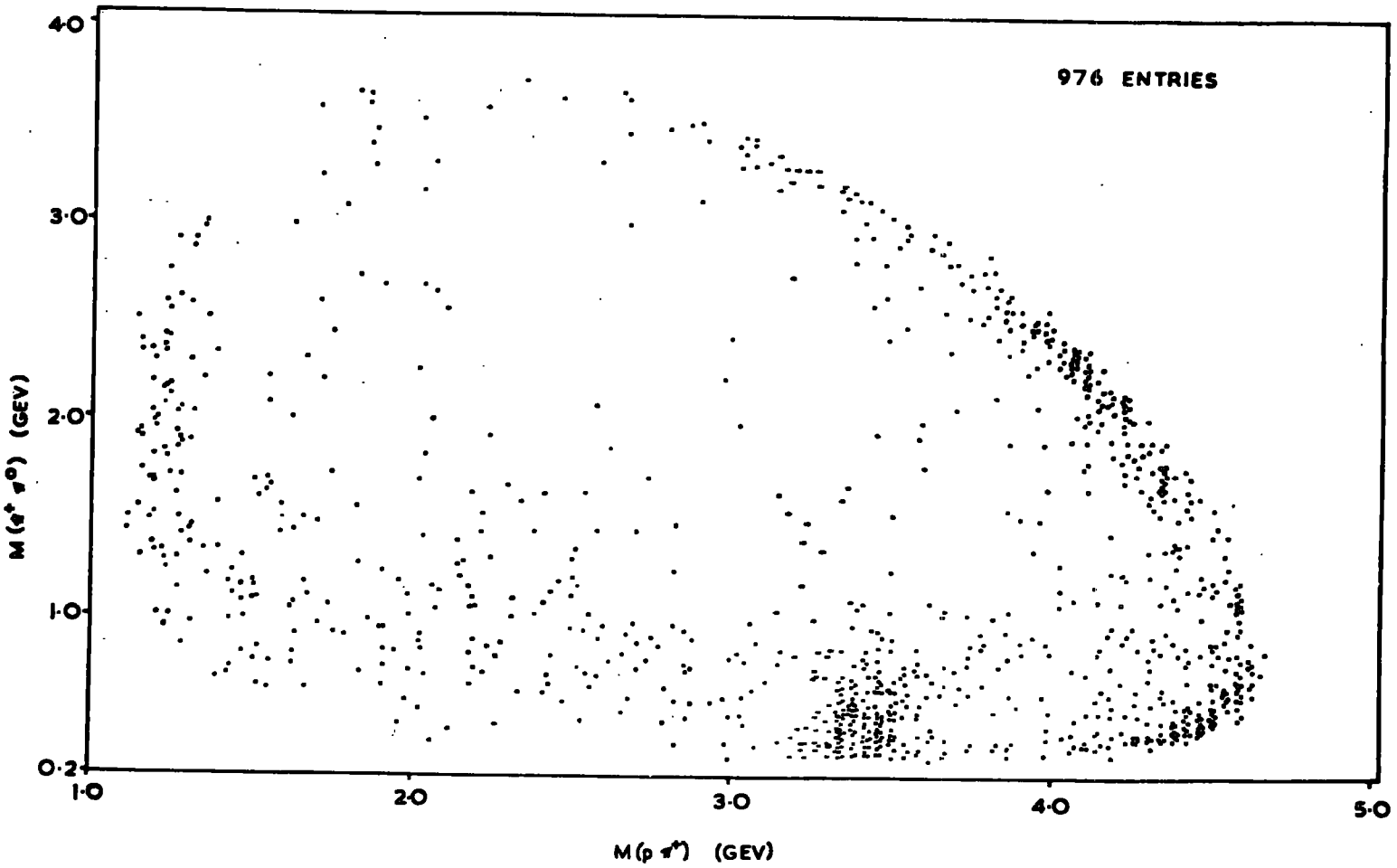
M(pπ+)vs. M(π+π0)IN REACTION π+p→π+pπ0 AT 11·5 GEV/c
976 ENTRIES
4·0
3·0
2·0
1·0
0·2
M(p π+) (GEV)
1·0
2·0
3·0
4·0
5·0
M(p π+) (GEV)

i) for $M(\pi^+\pi^o) < 0{\cdot}76$ Gev and $3{\cdot}20 \leq M(p\pi^+) < 3{\cdot}64$ Gev

ii) for $M(\pi^+\pi^o) < 0{\cdot}76$ Gev and $M(p\pi^+) > 4{\cdot}2$ Gev

The events in region (i) are characterised by a $\pi^+$ and $\pi^o$ both having a laboratory momentum of $6{\cdot}0 \pm 1{\cdot}5$ Gev/c as shown in Fig.(52A). No such peaks are observed at 5 Gev/c (Fig.(52B)) or in the reactions C, D, and E at $11{\cdot}5$ Gev/c.

The sagittas of the primaries and secondaries of region (i) events have been measured on the scanning table for the Durham data only. It is beyond doubt that for these events the sagittas of the secondary pions correspond to a momentum that is half the primary momentum, and that the primary sagitta corresponds to $11{\cdot}5$ Gev/c. Therefore it can be concluded that the events are not due to a 6 Gev/c primary contamination which undergoes elastic scattering. Furthermore, the events seem to have been well measured and the $\chi^2$ distribution is normal.

In terms of resonance production, it seems highly unlikely that such a low mass dipion resonance would not have been observed before now. A resonance in the $p\pi^+$ system would have a very assymmetrical angular distribution which could not arise from the parity conserving decay of an object of fixed spin.

However, the 6 Gev/c peaks in the pion momentum distributions could be accounted for by the following reaction

$$d + p \longrightarrow p + n + p(\text{recoil})$$

FIG. 52

# LABORATORY MOMENTA OF SECONDARY PIONS

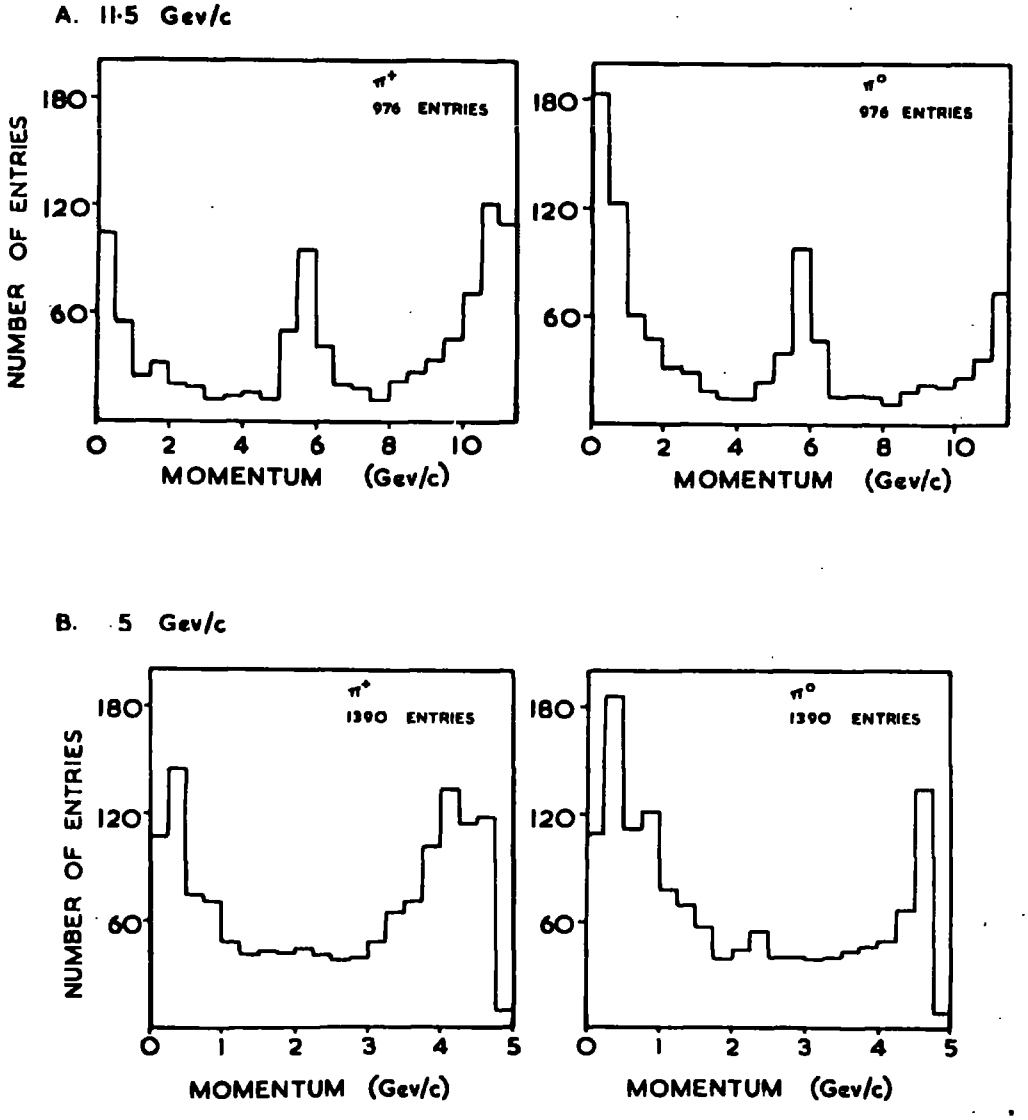

in which the deuteron primary undergoes a stripping reaction and the two secondaries would have approximately one half of the primary momentum (plus Fermion momentum).

The compatibility of this hypothesis with events in region (i) has been tested by calculating the square of the missing mass ($MM^2$) from the measured momenta assuming a deuteron beam and two protons in the final state. The distribution of $MM^2$ is shown in Fig.(53). The events in region (i) give rise to a sharp peak at the square of the neutron mass ($\sim 0{\cdot}88$ Gev$^2$).

On the question of whether or not deuterons could have been transported efficiently down the U3 beam, calculations by P. Lazeyras (CERN) indicate that, since the radiofrequency separators only rejected protons and kaons, the deuteron contamination could have been 0·5-1·0%. Using a deuteron stripping reaction cross section of ~11mb the deuteron contamination would need to be just under 1% to produce the observed excess in region (i).

In conclusion, the deuteron hypothesis seems to be the most likely explanation, but cannot be proved until a counter experiment is set up in the U3 beam and the deuteron flux measured.

In order to suppress this contamination a cut has been imposed of reaction B for $MM^2$ (assuming a deuteron beam) as follows

$$0{\cdot}8 \leqslant MM^2 < 1{\cdot}0 \text{ Gev}^2$$

Cutting out events within the above interval should not have

FIG. 53

$MM^2$ ASSUMING THE REACTION $d+p \rightarrow p+p+n$
FOR EVENTS FITTED WITH THE REACTION
$\pi+p \rightarrow \pi+p\pi^0$

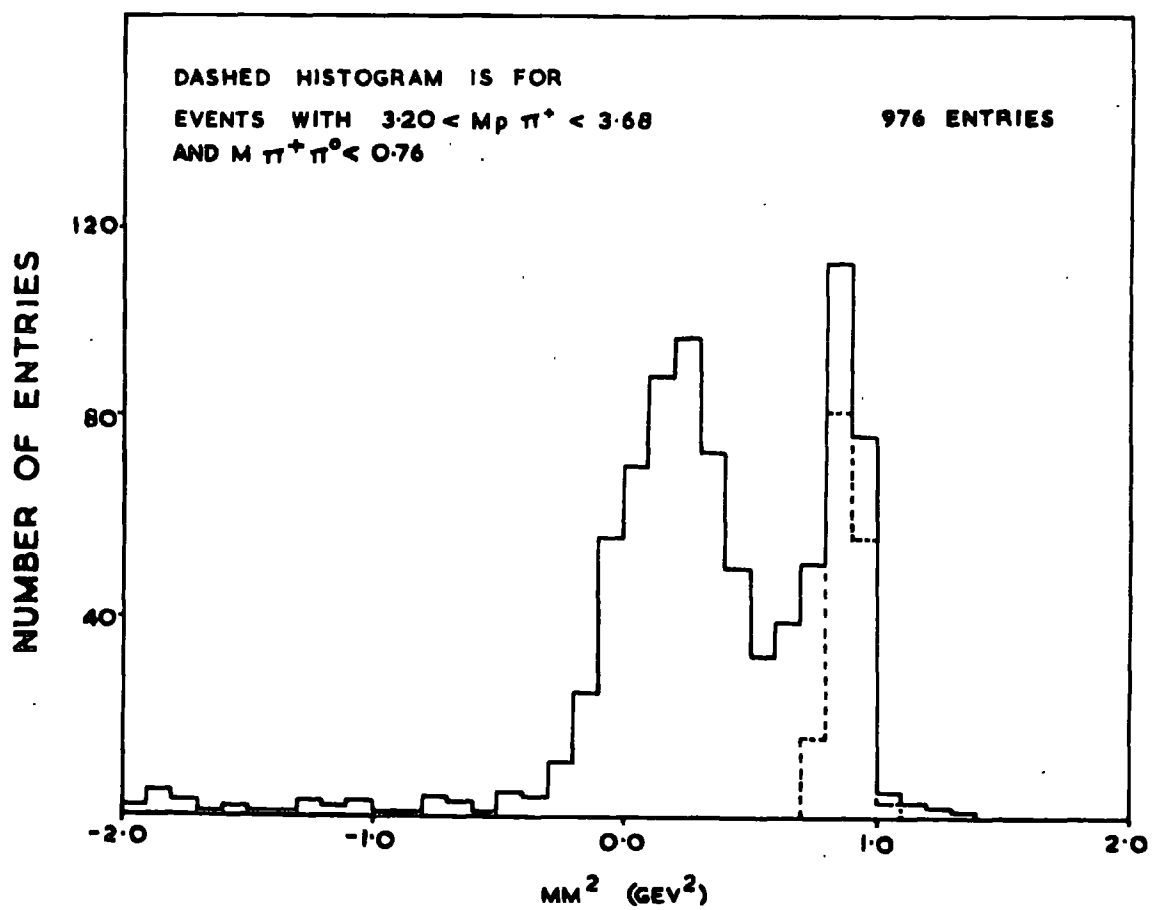

removed more than ~2% of the true reaction B events in region (i).

The excess of events in region (ii) was also reported in a similar plot by the Aachen-Berlin-CERN collaboration at 8 Gev/c (53) in which it was concluded that the excess was due to contamination from the elastic channel. The explanation was that when the outgoing pion of an elastic event suffers small angle scattering its momentum may be measured too low to fit the elastic reaction. The event is then fitted kinematically by introducing a $\pi^o$ lying in almost the same direction as the $\pi^+$. The $\pi^o$ will have low energy which automatically means that $M(\pi^+\pi^o)$ for such events will be low. If the normal elastic events of reaction A are allowed to contaminate the reaction B channel then they certainly do occupy region (ii) of the Dalitz plot in Fig.(51).

As a further test of this assumption the coplanarity of events in reaction A and reaction B have been determined. The $\pi^+$, proton, and incident $\pi^+$ should all lie in the same plane for an event to be coplanar. As expected the elastic events of reaction A are almost entirely coplanar, while events in reaction B are far from being coplanar because of the added $\pi^o$. However, the events of region (ii) are also very nearly coplanar which leads to the conclusion that these events are in fact poorly measured elastic events. Nevertheless, it must be borne in mind that genuine reaction B events in this region

must be similar, kinematically, to the elastic events.

In order to try and eliminate the contamination in region (ii), events with $\cos\theta > 0{\cdot}98$ ($\theta$ is the angle between the plane of the incident $\pi^+$ and proton and the plane of the outgoing $\pi^+$ and proton) have been excluded from the sample. The number of genuine reaction B events removed by this cut should not be in excess of 1%.

In view of the fact that there is deuteron contamination it is possible that some of the events in region (ii) are coherent deuteron scatterings which have been badly measured. However, these should also have been removed by the cut on $\cos\theta$, and in any case it is most likely that the majority of deuteron scatterings would have been fitted successfully by the elastic hypothesis and be fairly uniformly distributed in the elastic channel so as not to introduce any significant biases.

b) Introduction

The centre of mass momentum and angular distributions for reaction B and reaction C are shown in Figs.(54) and (55) respectively after the cuts described in the previous section have been applied. The peaking of the momentum distributions and the forward-backward assymmetry of the angular distributions again reflect the peripheral nature of the interactions as in the 5 Gev/c data.

FIG. 54

CENTRE OF MASS MOMENTUM (p*) FOR THE INELASTIC REACTIONS AT 11·5 GEV/c

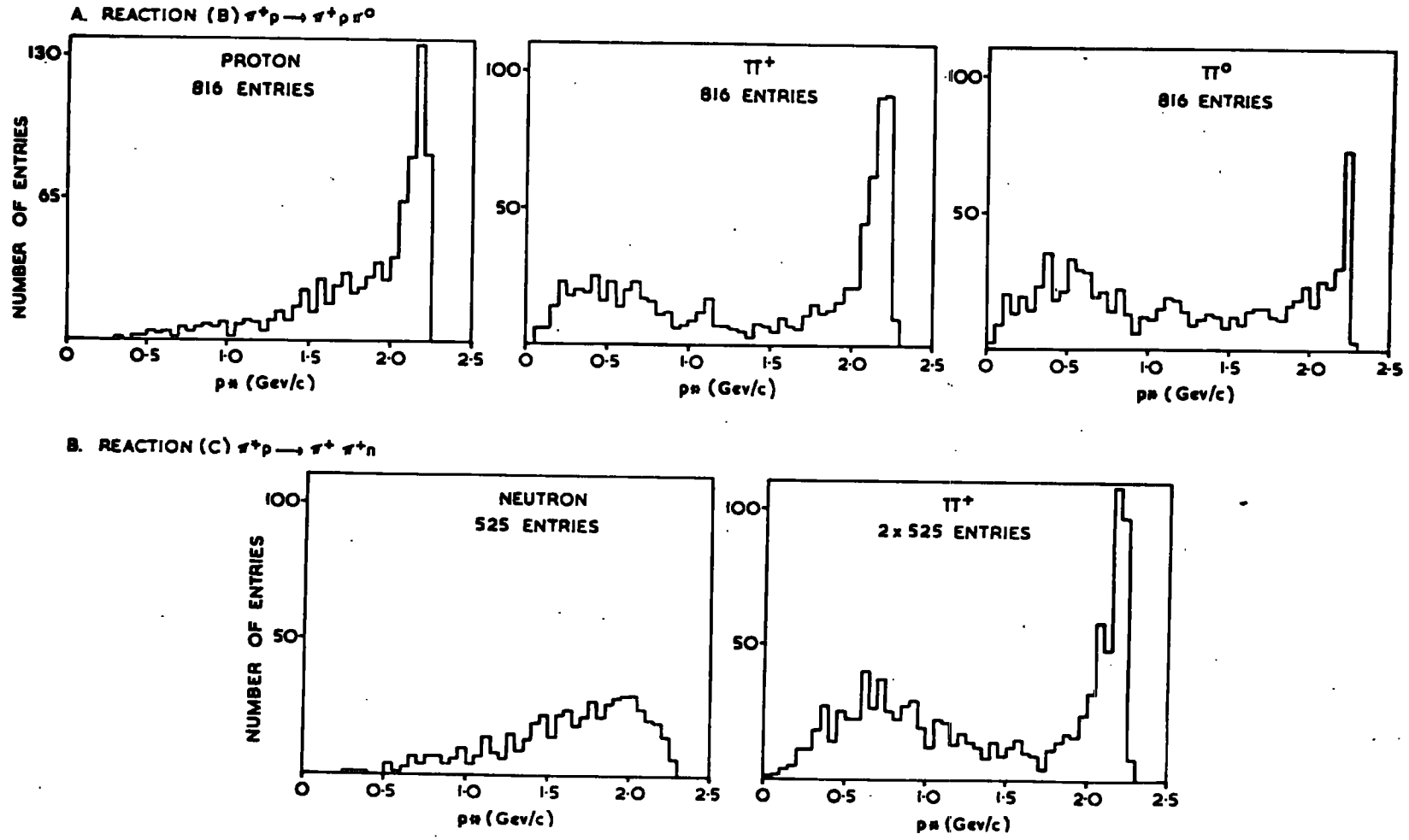

FIG. 55

# CENTRE OF MASS ANGLE ($\theta^*$) DISTRIBUTIONS FOR THE INELASTIC REACTIONS AT 11·5 GEV/C

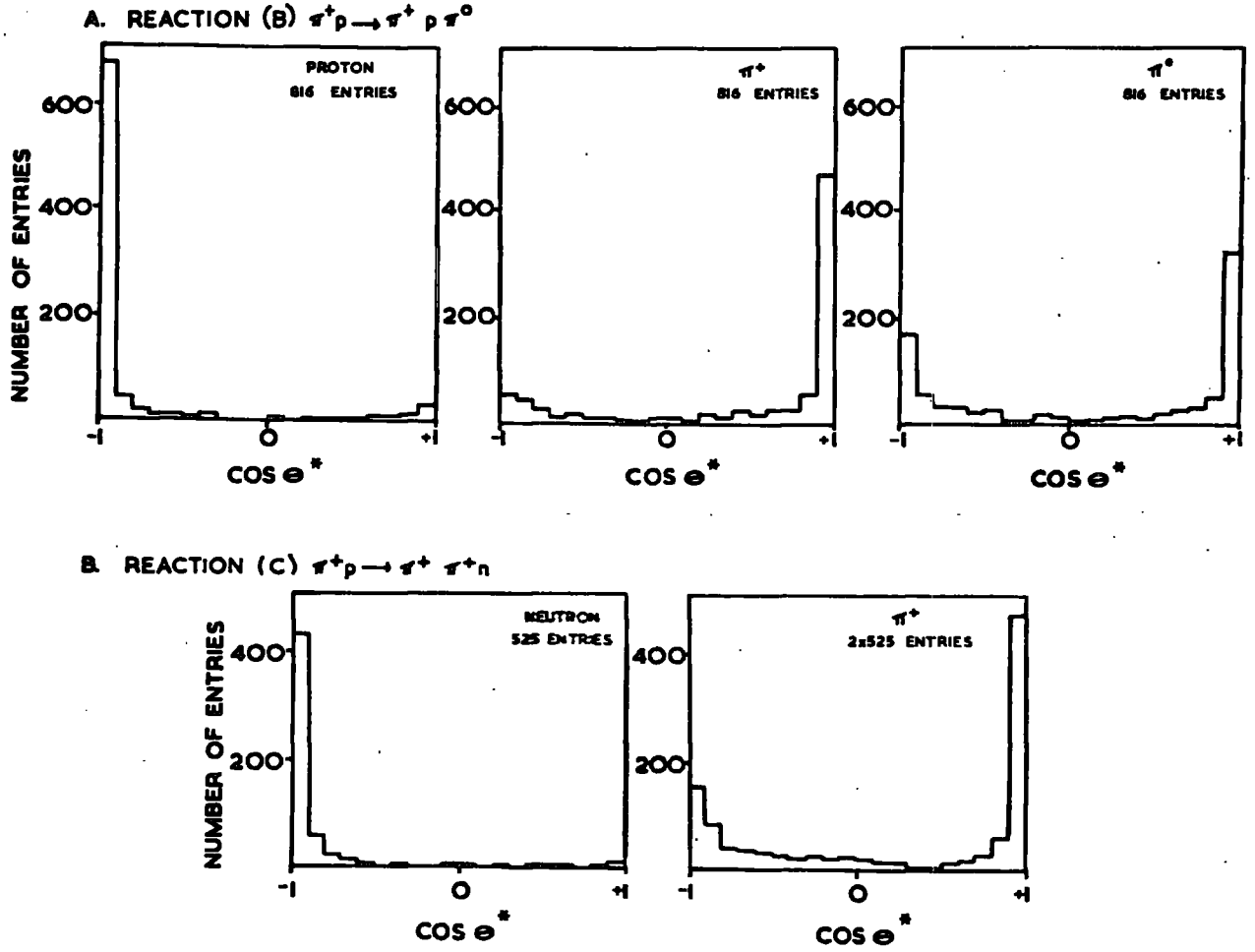

The values of the assymmetry parameter R (cf. section (5.3.a)) are listed in Table (18) for each of the particles in the two reactions.

TABLE 18

Assymmetry parameter R at 11·5 Gev/c

| Reaction | Particle | R |
|---|---|---|
| B. $\pi^+p \rightarrow \pi^+p\pi^o$ | Proton | -0·83 ±0·19 |
| | $\pi^+$ | 0·57 ±0·13 |
| | $\pi^o$ | 0·19 ±0·04 |
| C. $\pi^+p \rightarrow \pi^+\pi^+n$ | Neutron | -0·94 ±0·32 |
| | $\pi^+$ | 0·21 ±0·07 |

The values of R are in fair agreement with the values obtained for the 5 Gev/c experiment. However, it is noticeable that the $\pi^o$ angular distribution at 11·5 Gev/c is more symmetric than at 5 Gev/c and has a value of R much closer to the $\pi^+$ value in reaction C. This may well be a reflection of the lack of $\rho^+$ meson production at 11·5 Gev/c since the $\rho^+$, and therefore the $\pi^o$, go forward in the reaction centre of mass. Consequently the lack of $\rho^+$ production at 11·5 Gev/c could deplete the forward going contribution to the angular distribution.

Reaction B shows clearly the production of the $N^{*++}(1236)$ isobar in the $p\pi^+$ system, however, as was mentioned before, the $\rho^+(760)$ meson production cross section has fallen sharply from

FIG. 56

$M(p\pi^+)$ vs. $M(\pi^+\pi^0)$ IN REACTION $\pi^+ p \rightarrow \pi^+ p \pi^0$ AT 11.5 GEV/c

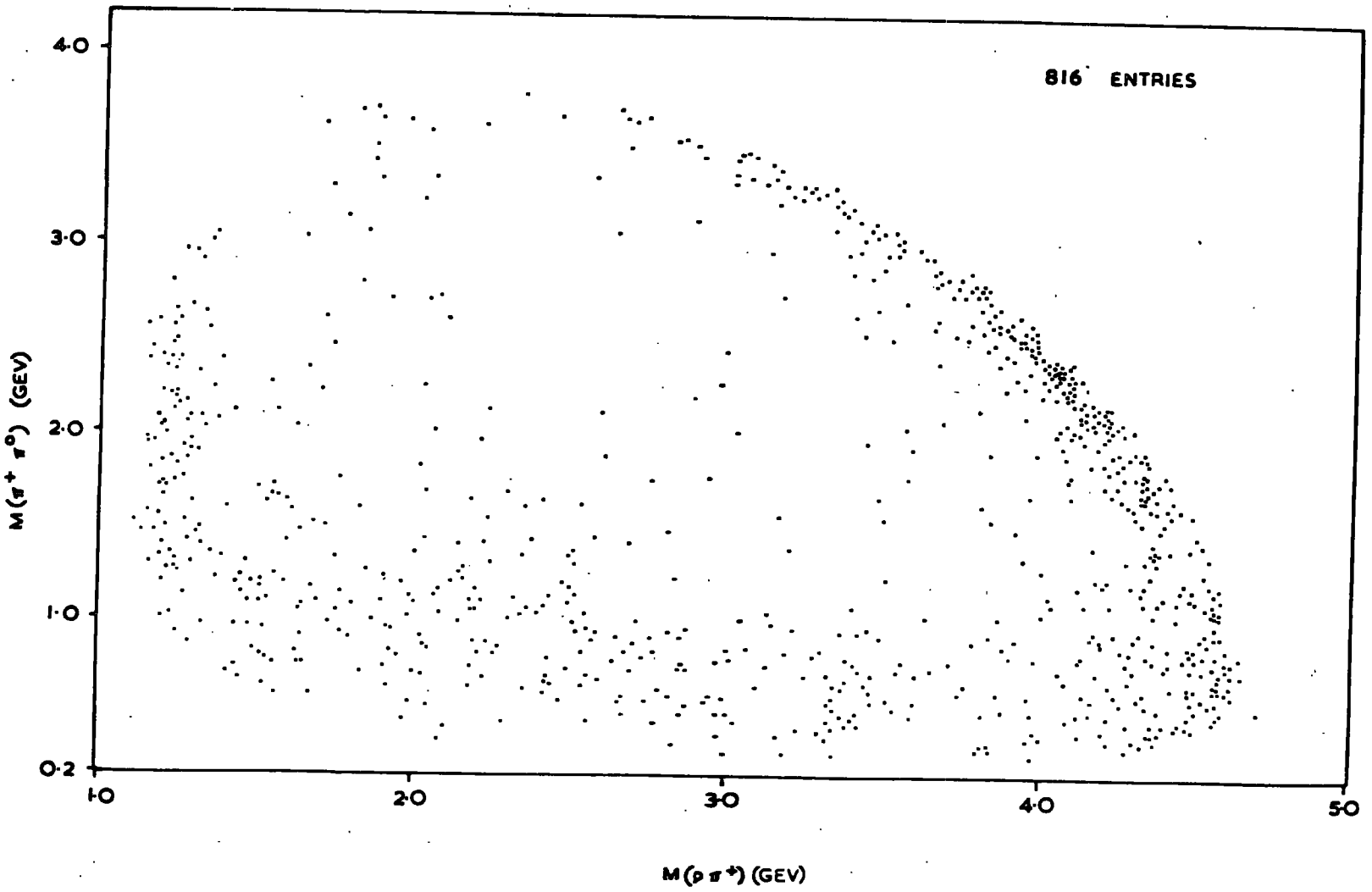

FIG. 57

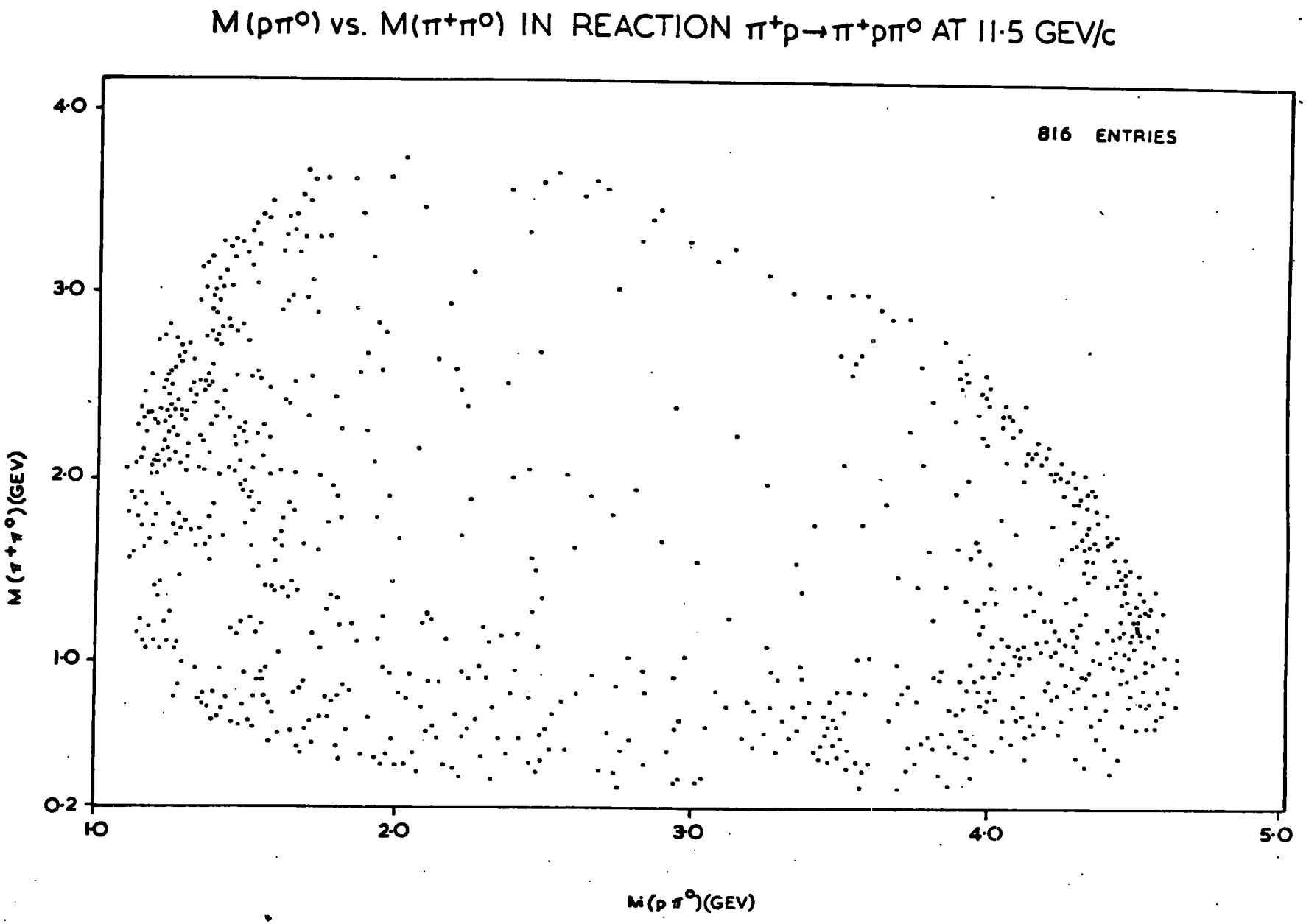
M(pπ°) vs. M(π⁺π°) IN REACTION π⁺p→π⁺pπ° AT 11·5 GEV/c
816 ENTRIES
4·0
3·0
2·0
1·0
0·2
1·0
2·0
3·0
4·0
5·0
M(π⁺π°)(GEV)
M(pπ°)(GEV)

FIG. 58

# $M(n\pi^+)$ vs. $M(\pi^+\pi^+)$ IN REACTION $\pi^+p \rightarrow \pi^+\pi^+n$ AT 11·5 GEV/c

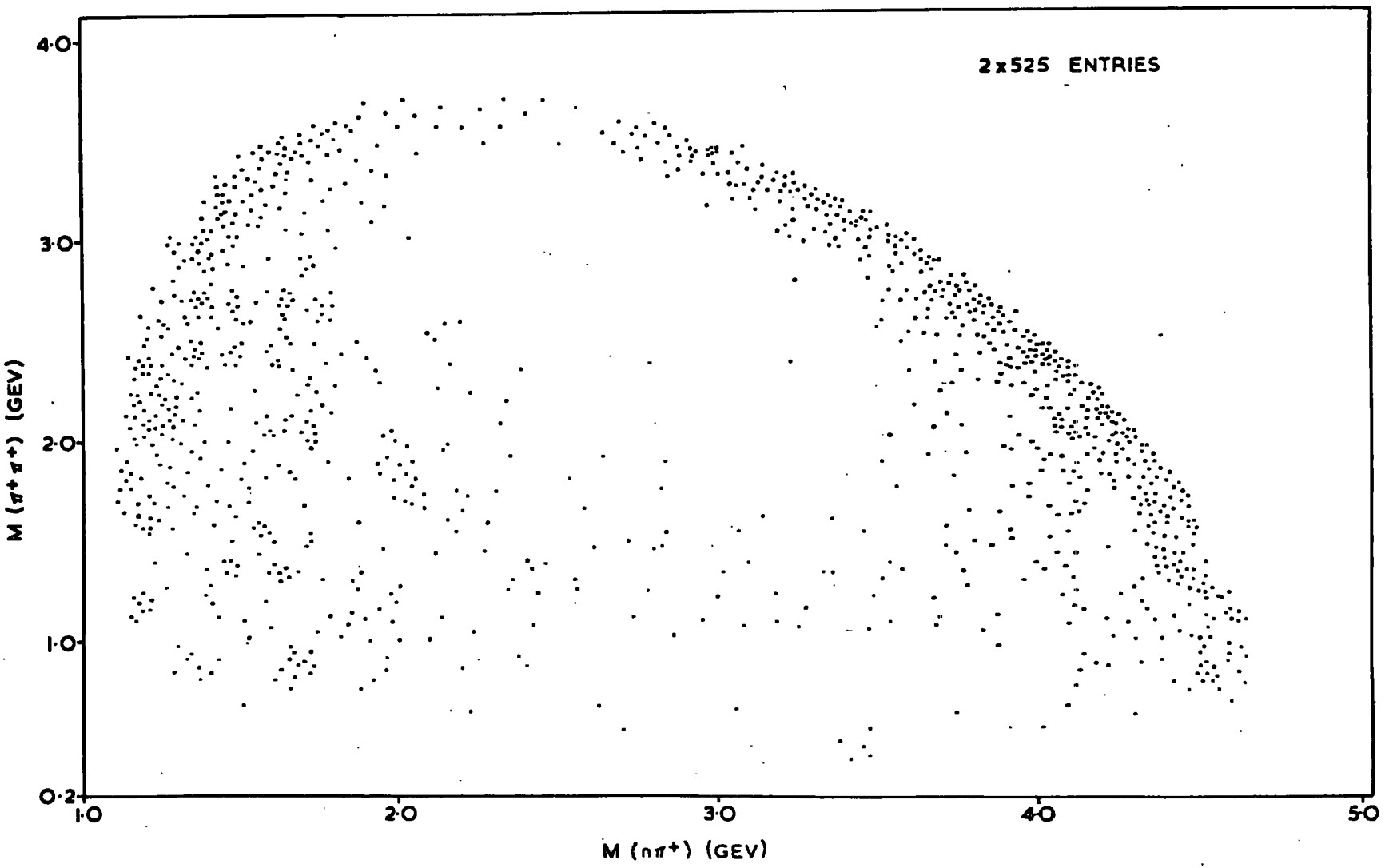

FIG. 59

# $M(p\pi^+)$ AND $M(p\pi^0)$ IN REACTION $\pi^+p \rightarrow \pi^+p\pi^0$ AT 11·5 GEV/c

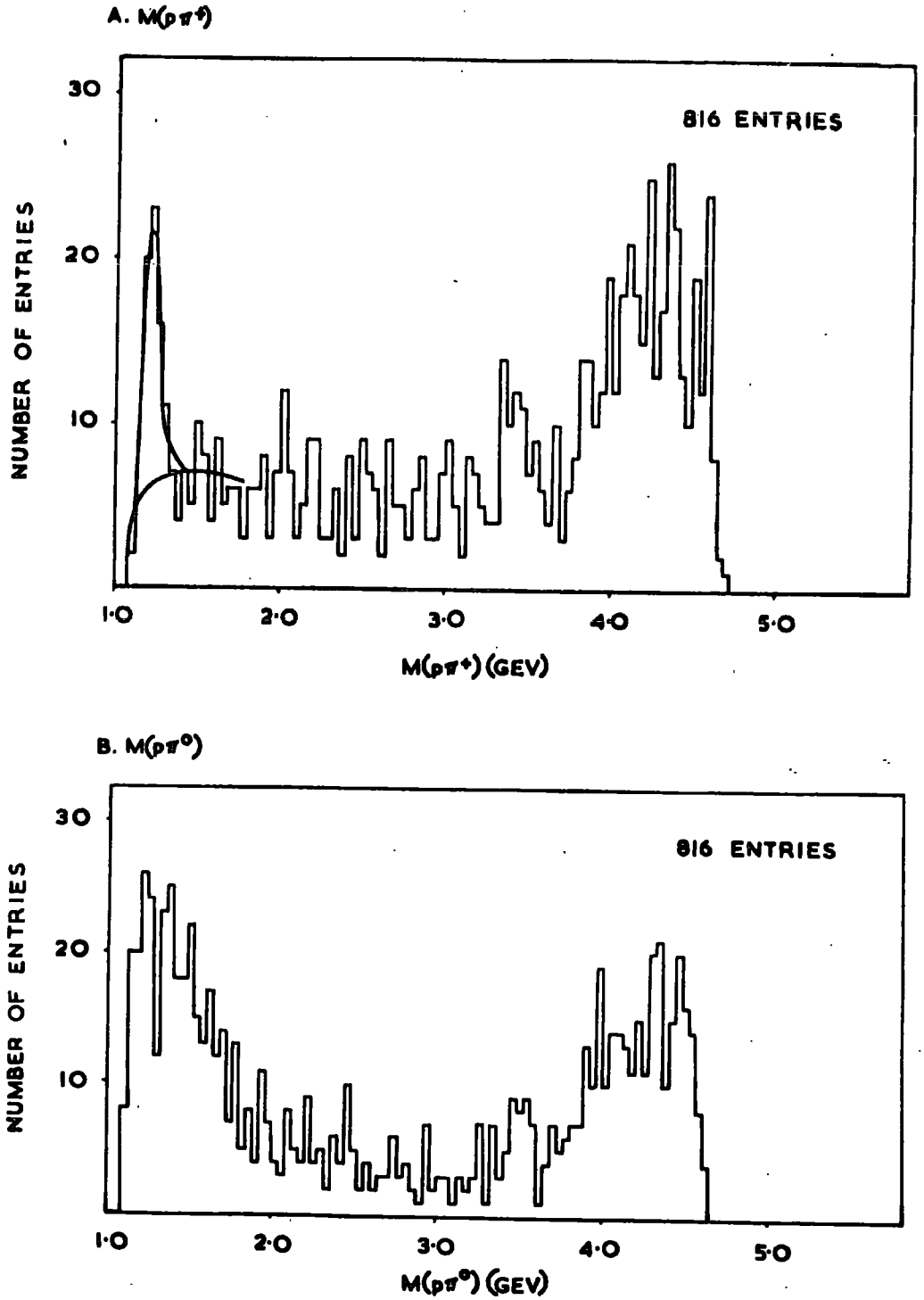

FIG. 60

M ($\pi^+\pi^0$) IN REACTION $\pi^+ p \rightarrow \pi^+ p \pi^0$ AT 11·5 GEV/c

A. SELECTED EVENTS

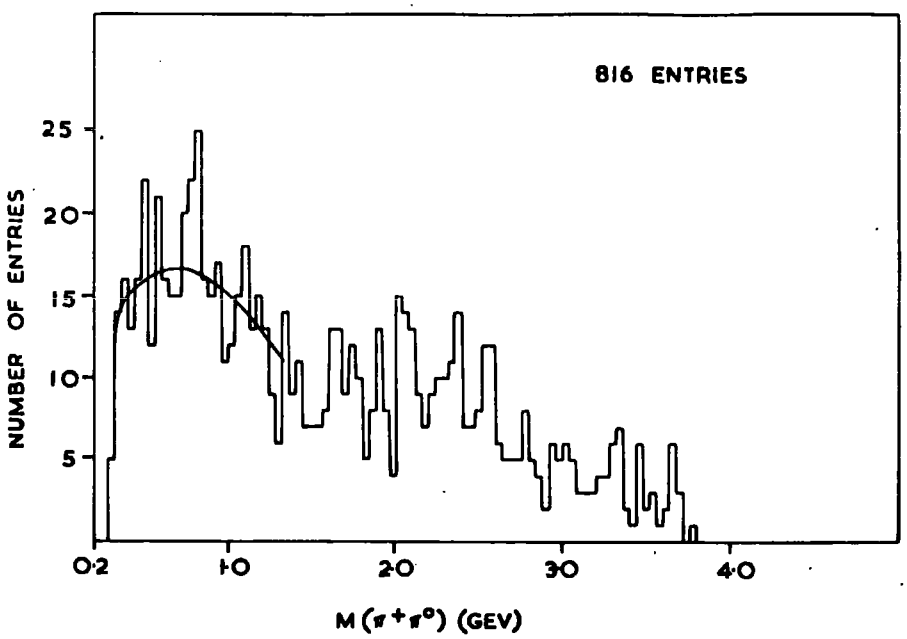


B. BEFORE ANY CUTS APPLIED TO DATA

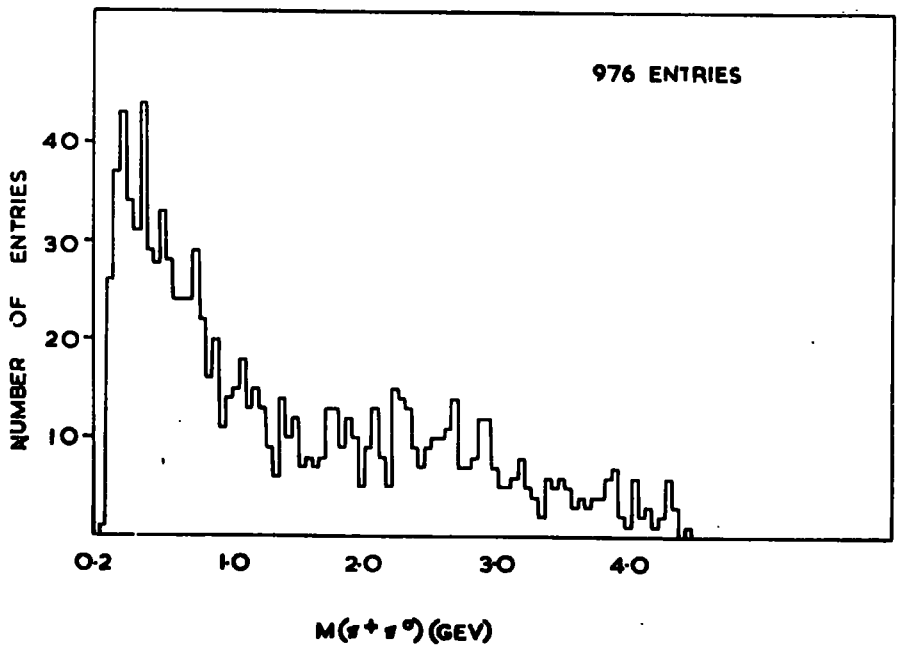

FIG. 61

# $M(n\pi^+)$ AND $M(\pi^+\pi^+)$ IN REACTION $\pi^+p \rightarrow \pi^+\pi^+n$ AT 11·5 GEV/c

A. $M(n\pi^+)$

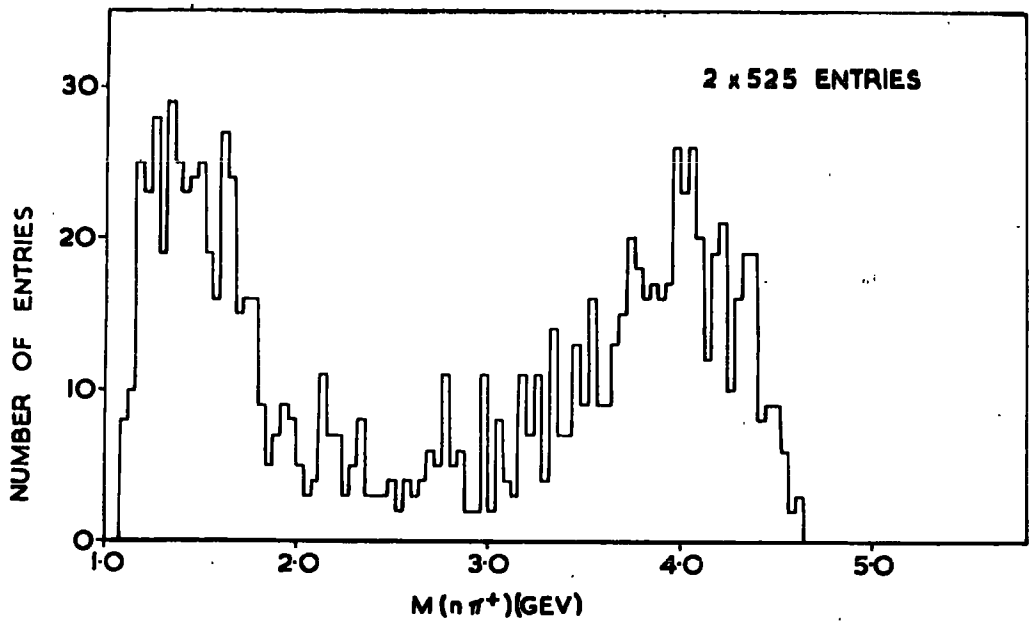


B. $M(\pi^+\pi^+)$

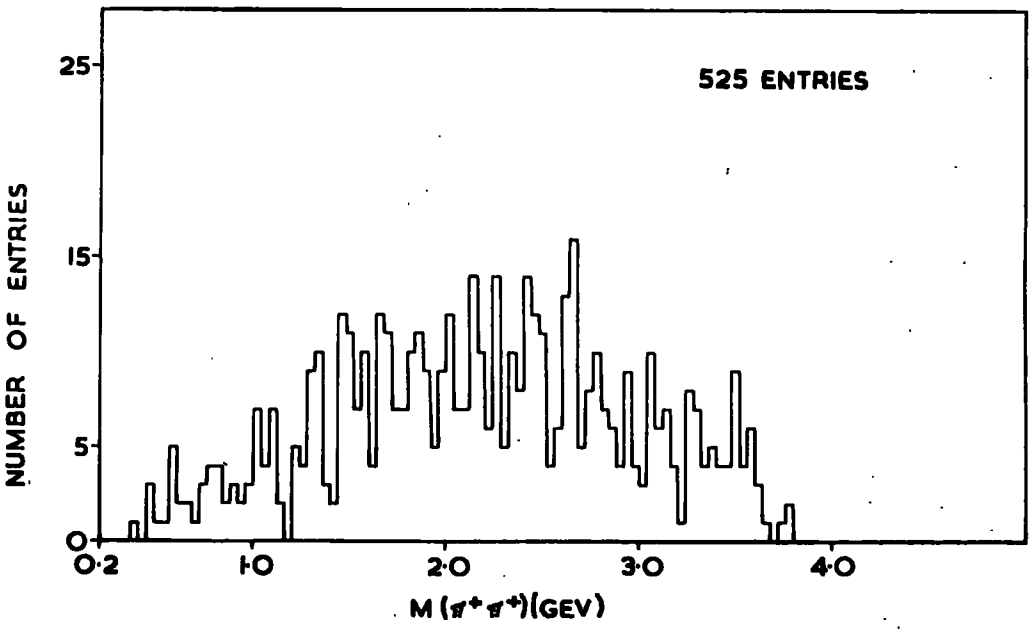

5 Gev/c. At 11·5 Gev/c, as at 5 Gev/c, there is no evidence for the $g^+(1650)$ meson in the $\pi^+\pi^o$ system.

Following the methods used at 5 Gev/c, the $N^{*++}$ production mechanism has been examined on the basis of the absorption model and the Regge pole model for $\rho$ exchange. However, due to the small $\rho^+$ signal it has not been possible to repeat the 5 Gev/c investigations into its production mechanism.

c) N*(1236Mev) production

The Dalitz plots of $M(p\pi^+)$ and $M(\pi^+\pi^o)$, $M(p\pi^o)$ and $M(\pi^+\pi^o)$, and $M(n\pi^+)$ and $M(\pi^+\pi^+)$ are shown in Figs.(56-58). There is clear evidence for an excess of events around the $N^{*++}(1236)$ in the $p\pi^+$ system. However, there is little evidence for $N^{*+}$ production in either the $p\pi^o$ system or the $n\pi^+$ system. Figs. (59A), (59B), and (61A) show the projections on to the $M(p\pi^+)$, $M(p\pi^o)$, and $M(n\pi^+)$ axes respectively.

i) Cross section for N* production

The production cross sections have been determined in the usual manner by estimating the number of events in the peaks above a smooth hand drawn background. The excess of events in the $N^{*++}$ peak ($1{\cdot}12 \leq M(p\pi^+) < 1{\cdot}32$ Gev) in Fig.(59A) above the drawn background is estimated to be $45 \pm 5$ giving a cross section for the reaction

$$\pi^+ p \rightarrow N^{*++} + \pi^o$$
$$\quad\quad\quad

of 0·034 ±0·007mb or 5·5 ±1·1% of the reaction B. The cross section has fallen sharply from the value of 0·1mb at 5 Gev/c in contradiction to the absorption model prediction of an increasing cross section. From Figs.(59B) and (61A) it has been impossible to determine any cross section for $N^{*+}$ production.

ii) Mass and width of the $N^{*++}$

The $N^{*++}$ peak has been reproduced using the Breit Wigner distribution of section (5.3.b(ii)) for which the best fit was obtained with values of the central peak and width of

$$M_o = 1215 \text{ Mev}$$
$$\Gamma(M_o) = 115 \text{ Mev}$$

which are in good agreement with the values obtained at 5 Gev/c.

Explanations for the narrower width and shift of the central value of the $N^{*++}$ peak from the generally accepted values of 140 Mev and 1236 Mev respectively are given in section (5.3.b(ii)).

iii) t-dependence of $N^{*++}$ production

At 11·5 Gev/c, as at 5 Gev/c, the $N^{*++}$ can be seen to be produced in highly peripheral interactions in the Chew Low plot of Fig.(62) and the Peyrou plot for $N^{*++}$ events in Fig. (64A).

The differential cross section ($\delta\sigma/\delta t$) distribution for

FIG. 62

CHEW LOW PLOT OF $M(p\pi^+)$ vs $t(p/p\pi^+)$ IN REACTION $\pi^+p \to \pi^+p\pi^0$ AT 11·5 GEV/C

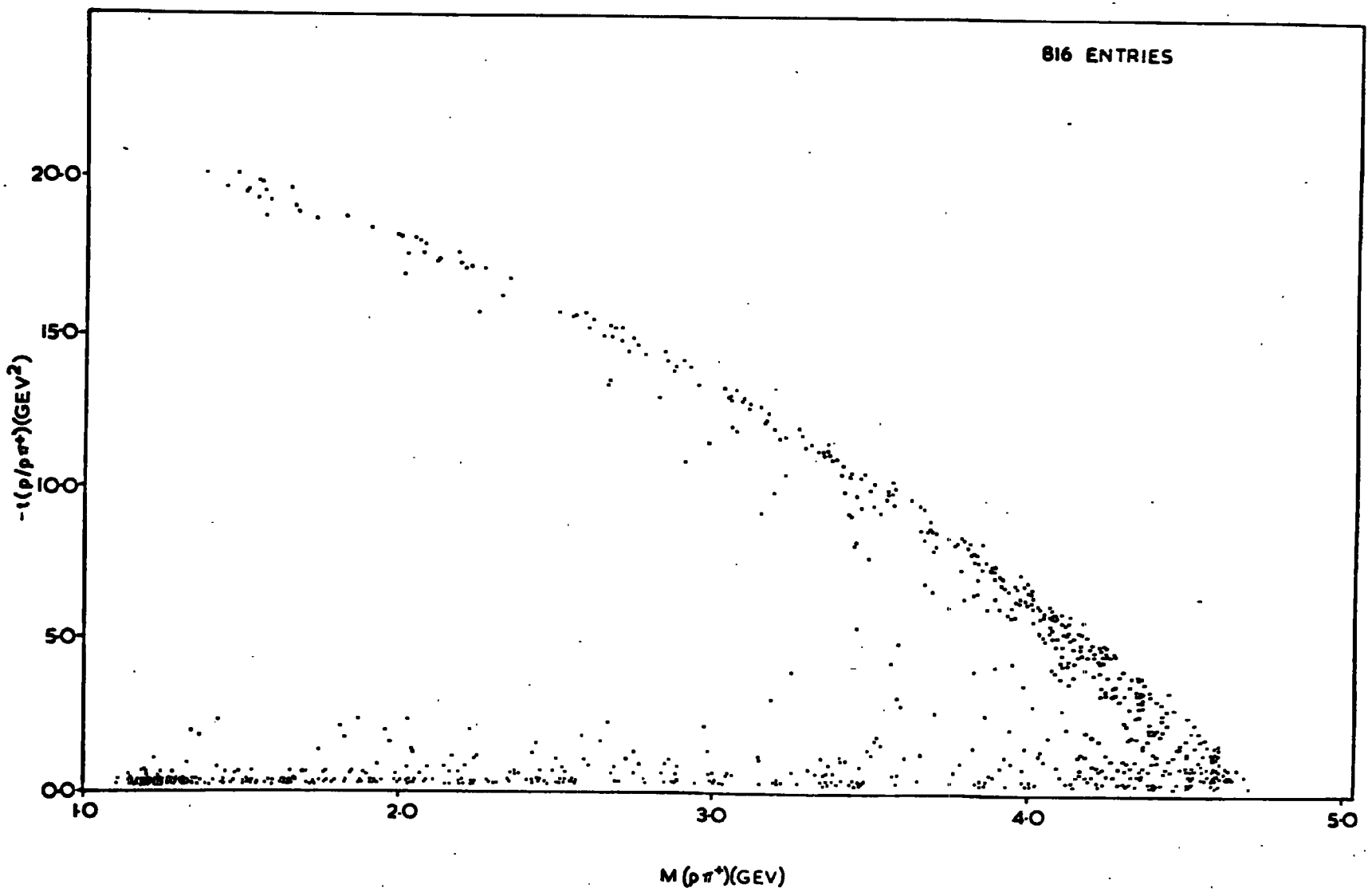

FIG. 63

CHEW LOW PLOT OF $M(\pi^+\pi^0)$ vs $t(\pi^+/\pi^+\pi^0)$ IN REACTION $\pi^+p \rightarrow \pi^+p\pi^0$ AT 11·5 GEV/C

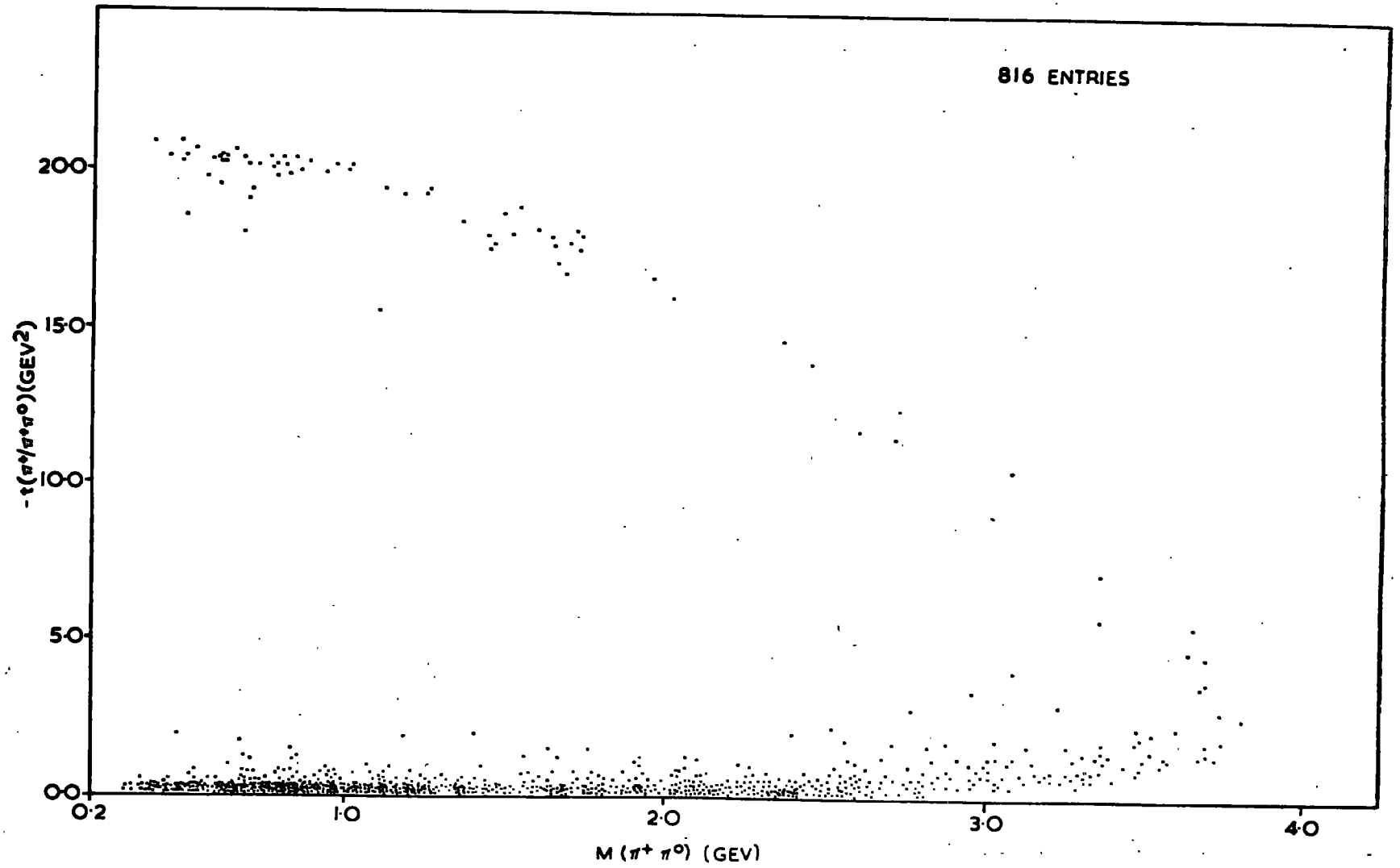

FIG. 64

PEYROU PLOT AND JACKSON ANGULAR DISTRIBUTIONS FOR $N^{*++}$ IN REACTION $\pi^+ p \rightarrow \pi^+ p \pi^0$ AT 11·5 GEV/c

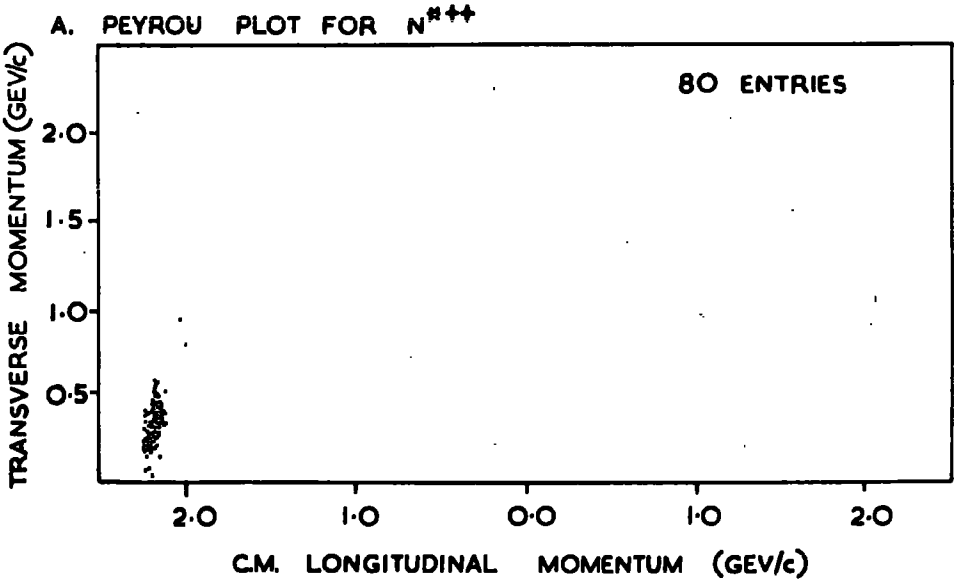


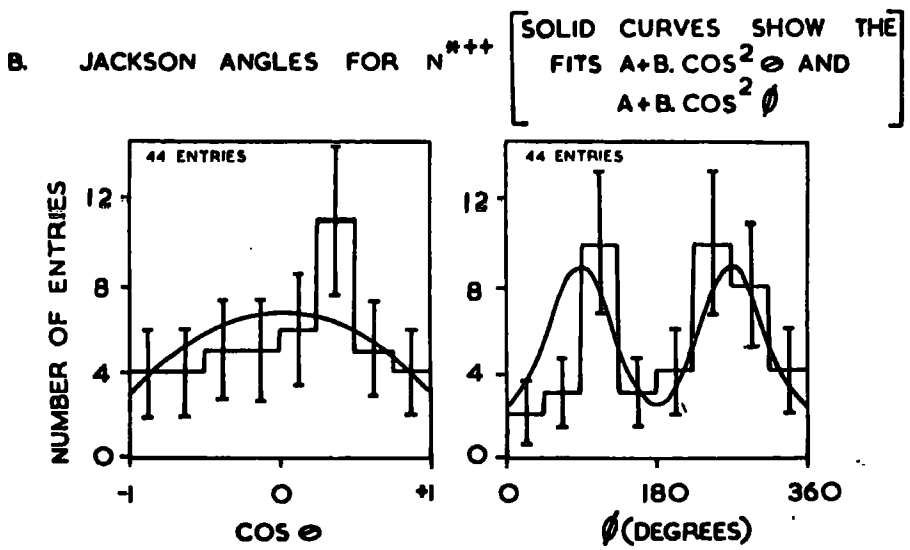

$N^{*++}$ events, with background events subtracted in the usual manner, is shown in Fig.(65). The absorptive peripheral model for ρ meson exchange again fails to reproduce the sharp fall in the cross section for increasing t values unless a t-dependent form factor is introduced. The dashed line of Fig.(65) shows the absorption model with a form factor

$$F(t) = \frac{a^2}{(-t + a^2)}$$

where a has the value 0·2. But as pointed out in section (5.3. b(iii)) a different form factor has to be invoked at different energies ($a \approx 0{\cdot}28$ at 5 Gev/c), and in any case the justification for form factors is very much in doubt.

On the other hand the Regge pole model for ρ trajectory exchange is shown by the solid curve of Fig.(65) and gives a reasonable description of the slope and shape of the differential cross section. However, the model predicts somewhat higher values of cross section than found experimentally.

iv) Decay angular distribution of the $N^{*++}$

The Jackson angular decay distributions for $\cos\theta$ and $\phi$ (defined in Fig.(3B)) for the $N^{*++}$ are shown in Fig.(64B). Only events have been plotted where the four momentum transfer to the $p\pi^+$ system is less than 0·3 $Gev^2$. Background events have been subtracted in the usual manner. The solid curves show the

FIG. 65

$\frac{d\sigma}{dt}$ vs. t DISTRIBUTION FOR $N^{*++}$ PRODUCTION IN REACTION $\pi^+ p \rightarrow \pi^+ p \pi^0$ AT 11·5 GEV/c

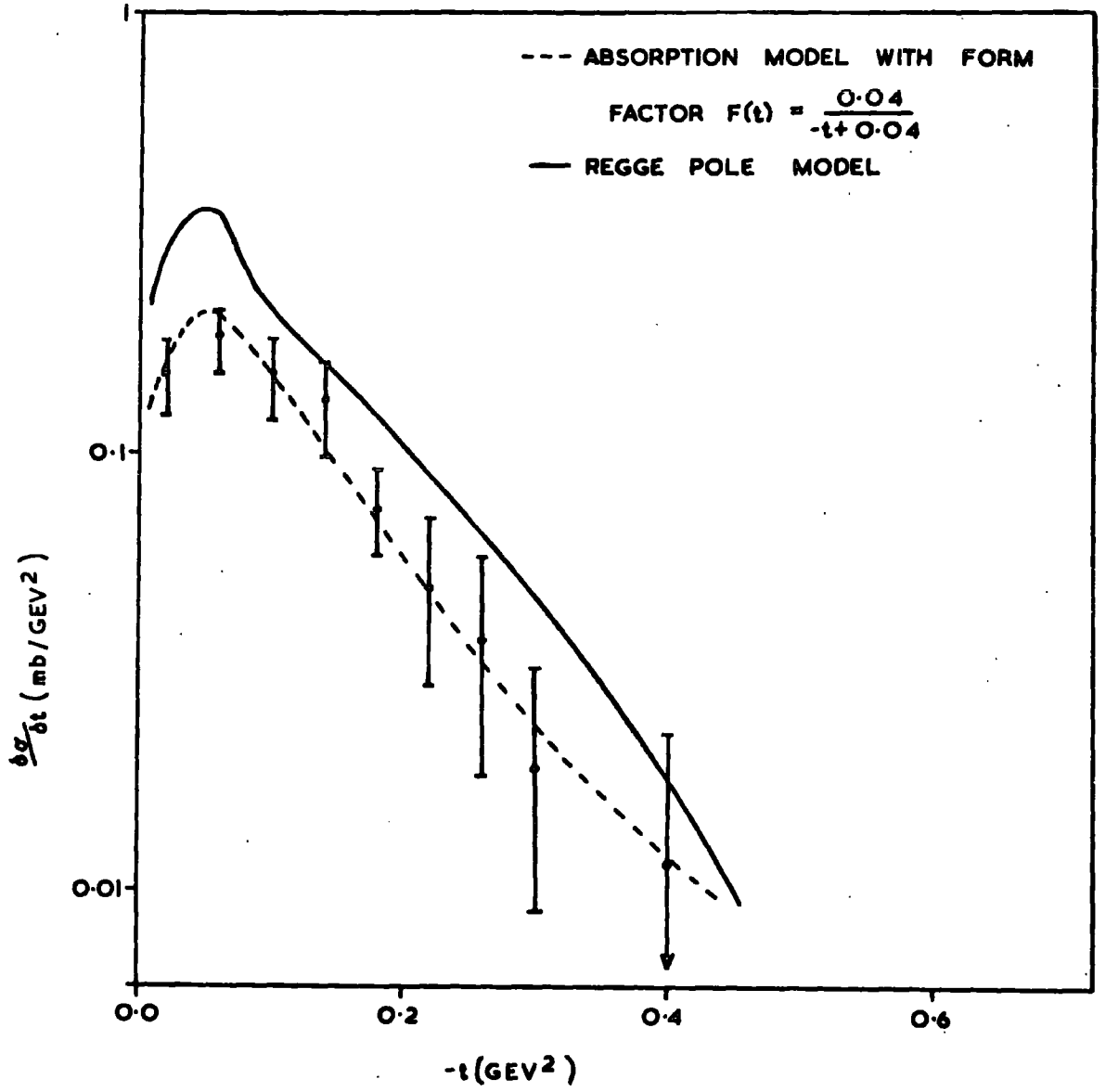

least squares fits $A+B\cos^2\theta$ and $A+B\cos^2\phi$ from which the $N^{*++}$ decay matrix elements have been determined using the expressions for the angular distributions given in section (5.3.b(iv)):

$$\rho_{33} = 0\cdot38 \pm 0\cdot10 \qquad \rho_{3,-1} = 0\cdot26 \pm 0\cdot03$$

The value of $\rho_{33}$ is much higher than the expected value of ~0·1 based on the absorption model. However, there is a large error present which occurs because of the single sharp peak in the $\cos\theta$ distribution, due probably to low statistics. The value of $\rho_{3,-1}$ is in good agreement with the absorption model prediction of 0·21.

As with the 5 Gev/c data the absorption model gives a fair description of the density matrix elements for the decay of the $N^{*++}$ but fails badly to describe the differential cross section unless t-dependent, and indeed energy dependent, form factors are introduced. The Regge pole model for ρ trajectory exchange, however, gives a much better description of the differential cross section.

d) <u>$\rho^+$(760Mev) production</u>

Fig.(60B) shows the effective mass $M(\pi^+\pi^o)$ in reaction B at 11·5 Gev/c before the cuts described in section (5.5.a) were imposed. Obviously any $\rho^+$ meson production is lost in the excess of events at low dipion mass values due to the contaminations described previously. Fig.(60A) shows $M(\pi^+\pi^o)$ again

after the cuts have been applied.

There appears to be an enhancement in the $\rho^+$ region but the background is high and very uncertain making it impossible to investigate the production mechanism.

A rough estimation of the number of events in the region $0{\cdot}64 \leq M(\pi^+\pi^o) < 0{\cdot}92$ Gev above the hand drawn background gives $20 \pm 3$ and a cross section for the reaction

$$\pi^+p \rightarrow p\ \rho^+ \quad (\rho^+ \rightarrow \pi^+\pi^o)$$

of $0{\cdot}015 \pm 0{\cdot}003$mb. The absorption model predicts a cross section of $\sim 0{\cdot}04$mb which is a factor of two difference, but obviously the $\rho^+$ production is not going to be very significant at this energy.

Adding this cross section to that for $N^{*++}$ production gives 8·2% as the fraction of quasi-two-body processes in the final state $\pi^+p\pi^o$.

5.6 <u>11·5 Gev/c NO FIT reaction D</u>

As with the 5 Gev/c data only events have been selected of the type $\pi^+p \rightarrow \pi^+p\pi^o$ $(m\pi^o)$ $m \geq 1$ where the proton has been definitely identified on the scanning table.

The $N^{*++}(1236)$ isobar can be seen in the effective mass plot of $M(p\pi^+)$ for these events in Fig.(66A). There are 161 $\pm 12$ events above the hand drawn background giving a cross

FIG. 66

# $M(p\pi^+)$ AND MISSING MASS (MM) IN REACTION (D) $\pi^+ p \rightarrow \pi^+ p \pi^0$ $(m\pi^0)$ $m \geq 1$ AT 11·5 GEV/c

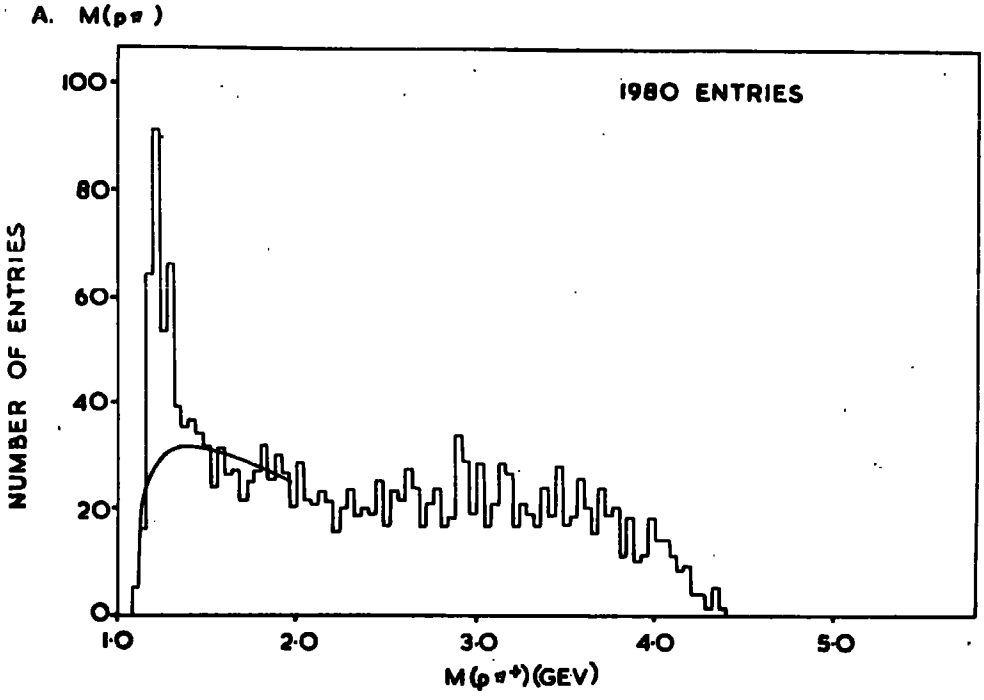


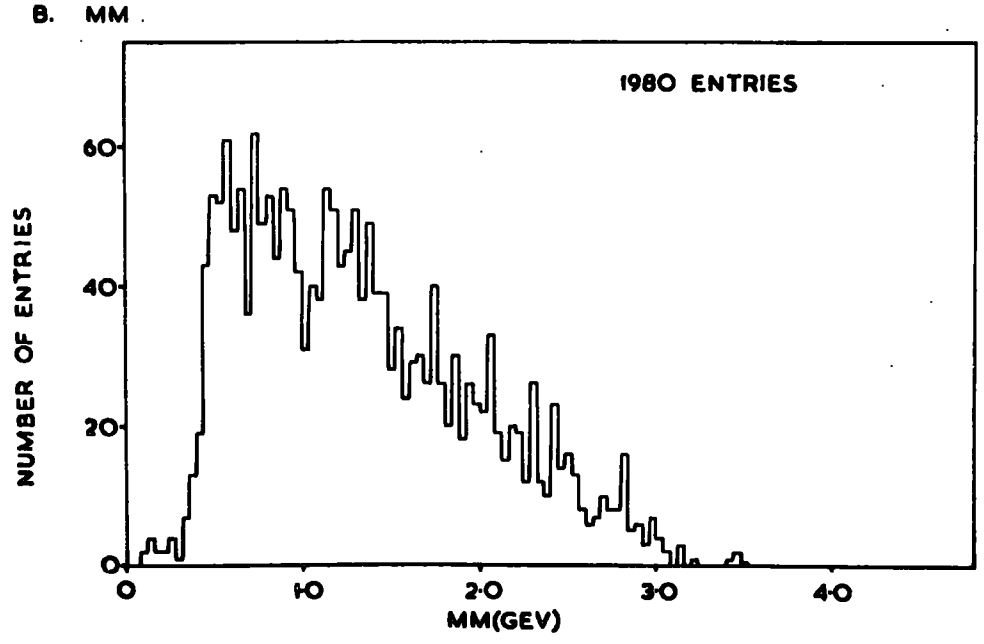

section for the reaction

$$\pi^+ p \longrightarrow N^{*++} + \text{neutrals}$$
$$\hookrightarrow p\pi^+$$

of 0·122 ±0·015mb.

The cental value of the peak and the width have been estimated to be

$$M_o = 1220 \text{ Mev}$$
$$\Gamma(M_o) = 120 \text{ Mev}$$

in good agreement with the values obtained for $N^{*++}$ production in reaction B.

The missing mass (MM) for reaction D is shown in Fig.(66B). Unlike the 5 Gev/c data there is no clear evidence for the $\eta^o(560)$ meson. In Fig.(67A) the missing mass is again shown with the restriction that the effective mass $M(p\pi^+)$ must lie in the $N^{*++}$ region ($1{\cdot}12 \leqslant M(p\pi^+) < 1{\cdot}32$ Gev). Although there are signs of enhancements in the regions of MM ≈ 600 Mev and MM ≈ 1300 Mev corresponding to the reactions

$$\pi^+ p \rightarrow N^{*++} + \eta^o$$
$$\hookrightarrow p\pi^+ \quad \hookrightarrow \text{neutrals}$$

$$\pi^+ p \rightarrow N^{*++} + f^o$$
$$\hookrightarrow p\pi^+ \quad \hookrightarrow \text{neutrals}$$

the background is so uncertain on the present data that it is

FIG. 67

# MM AND M($\pi^+$+MISSING NEUTRALS) IN REACTION (D)
# $\pi^+ p \rightarrow \pi^+ p \pi^0 (m\pi^0)$ $m \geq 1$ AT 11·5 GEV/c

A. MM [M($p\pi^+$) IN $N^{++}$]

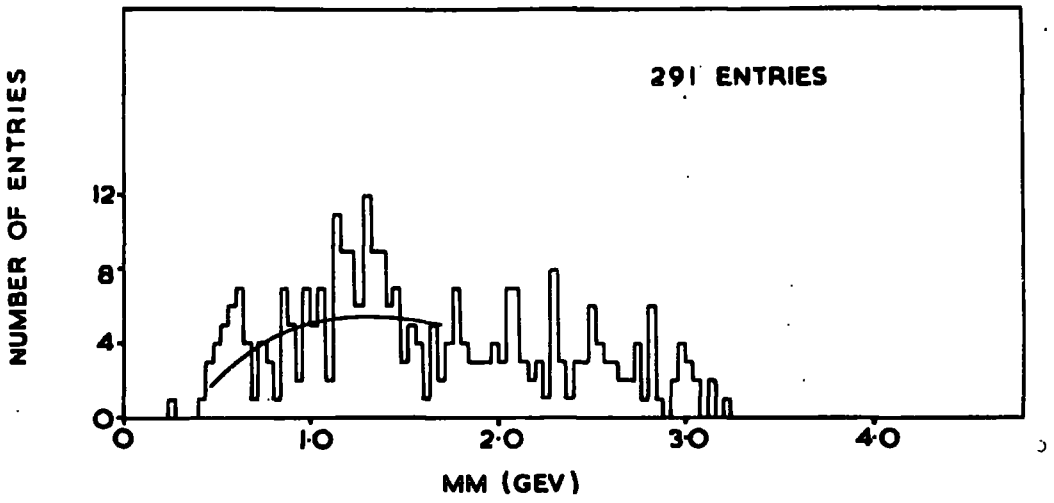


B. M ($\pi^+$+NEUTRALS) [M($p\pi^+$) NOT IN $N^{++}$]

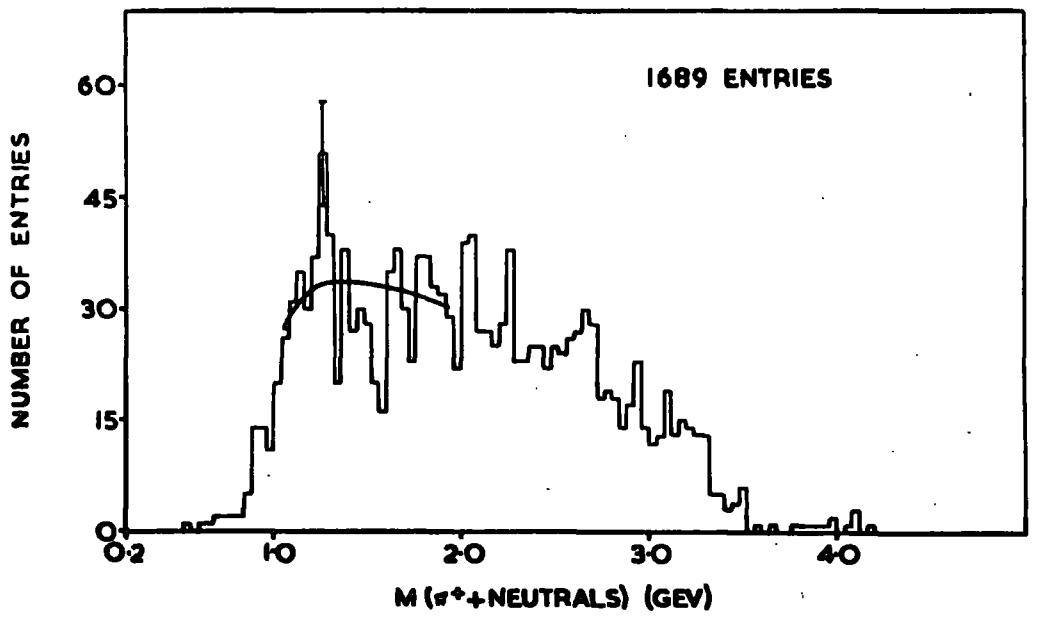

not possible to determine cross sections.

In order to look for the $A_2$ and $A_3$ mesons at this energy the effective mass of the $\pi^+$ and the missing neutrals, $M(\pi^+ +$ neutrals), has been plotted in Fig.(67B) with $M(p\pi^+)$ outside the $N^{*++}$ region. There is still clear evidence for the $A_2$ meson at ~1300 Mev, but there is no enhancement at ~1640 Mev corresponding to the $A_3$ resonance.

## CONCLUSIONS AND COMPARISONS

This thesis has described the preliminary results of two experiments at 5 Gev/c and 11·5 Gev/c concerning the interactions of positive pions on protons with two charged particles in the final state.

The total cross sections and the different channel cross sections have been found to be in agreement with the general trends found in other experiments. In particular, the total and elastic cross sections are seen to be approaching constant values asymptotically.

The elastic channel differential cross sections have been found to give slopes for the very forward diffraction peaks of the order of 7-9 $Gev^{-2}$, in good agreement with work at other energies. This confirms that the reaction $\pi^+p \rightarrow \pi^+p$ exhibits an energy independent optical diffraction behaviour for $-t < 0{\cdot}4$ $Gev^2$, as opposed to say pp scattering where the diffraction peak shrinks with increasing energy.

At a -t value of 0·7-1·0 $Gev^2$ there is seen to be a sharp change of slope at both 5 and 11·5 Gev/c such that two exponential straight lines can be fitted to the data. This effect has also been observed by the Aachen-Berlin-CERN collaboration at 8 Gev/c, and the explanation has been tentatively put forward that it may be due to multiple scattering corrections to Pomeron exchange.

A backward peak is observed in the elastic channel cross section at 5 Gev/c but not at 11·5 Gev/c. However, this may be due to the very low cross section and the relatively small number of events.

In the inelastic reaction channel

$$\pi^+ p \rightarrow \pi^+ p \pi^o$$

production of the $N^{*++}(1236)$ and $\rho^+(760)$ resonances is observed at both energies. However, the determination of the $\rho^+$ enhancement at 11·5 Gev/c is made uncertain because of the various contaminations in this channel at low dipion mass values. The cross sections for the reactions $\pi^+ p \rightarrow N^{*++} \pi^o$ and $\pi^+ p \rightarrow p\rho^+$ are shown in Table (19) over an energy range of 4 to 11·5 Gev/c.

TABLE 19

Quasi-two-body cross sections (mb)

| Final state | 4 Gev/c | 5 Gev/c | 8 Gev/c | 11·5 Gev/c |
|---|---|---|---|---|
| $N^{*++}\pi^o$ | 0·30 | 0·10 | 0·11 | 0·034 |
| $p\rho^+$ | 0·35 | 0·20 | 0·14 | 0·015 |

The cross sections for $\rho^+$ production are almost in agreement with absorption model predictions, whereas the $N^{*++}$ cross sections disagree violently. It is to be noticed that the $N^{*++}$ cross section at 5 Gev/c is rather low. From the values at 4

Gev/c and 8 Gev/c one might have expected a cross section of about 0·15mb. The fraction of quasi-two-body states is seen to be falling quickly with energy from 24·8% at 5 Gev/c to 8·2% at 11·5 Gev/c.

The $N^{*++}$ and $\rho^+$ have been seen to be produced with low four momentum transfer, even more so at the higher energy of 11·5 Gev/c. Consequently the peripheral model has been used to attempt to describe the production mechanisms. In $\rho^+$ production, where the exchanged particle is assumed to be a pseudoscalar pion, the absorptive peripheral model reproduces the differential cross section quite well. However, for $N^{*++}$ production which is assumed to be dominated by $\rho^+$ vector meson exchange the absorption model fails to fit the data. In contrast, the Regge pole model for $\rho$ trajectory exchange gives an appealing fit to the data although the predicted cross sections are a little higher than observed. This is quite possibly due to the low cross section observed for the $N^{*++}$ at 5 Gev/c and to the low statistics at 11·5 Gev/c.

The density matrix elements have been determined from the decay angular distributions of the $N^{*++}$ and $\rho^+$ and seem to be in fair agreement only with absorption model predictions. Table (20) summarises the data on the density matrix elements in the energy range of 4 Gev/c to 11·5 Gev/c.

Using the Chew and Low extrapolation method for one pion exchange the $\pi^+\pi^o$ scattering cross section has been determined

TABLE 20

Density matrix elements

| Final state | Matrix element | 4 Gev/c | 5 Gev/c | 8 Gev/c | 11·5 Gev/c |
|---|---|---|---|---|---|
| $N^{*++}\pi^{o}$ | $\rho_{33}$ | 0·40 ±0·06 | 0·36 ±0·04 | 0·22 ±0·06 | 0·38 ±0·10 |
| | $\rho_{3,-1}$ | 0·21 ±0·08 | 0·07 ±0·06 | 0·13 ±0·07 | 0·26 ±0·03 |
| $p\rho^{+}$ | $\rho_{00}$ | 0·70 ±0·08 | 0·48 ±0·08 | 0·54 ±0·07 | -- |
| | $\rho_{1,-1}$ | 0·17 ±0·08 | 0·19 ±0·04 | 0·07 ±0·06 | -- |

at 5 Gev/c and found to exhibit a resonance behaviour in the region of the $\rho^{+}$ meson.

As was mentioned in Chapter 1 it must be concluded that the absorption model is somewhat unsound in that it fails to describe vector meson exchange processes. The Regge pole model seems to give much better results and predicts fairly well the observed energy dependence.

It is interesting to note that the differential cross sections for $N^{*++}$ and $\rho^{+}$ production can be fitted roughly with straight lines in the region $0{\cdot}04 < -t < 0{\cdot}4$ Gev$^2$ of the form

$$\frac{\delta\sigma}{\delta t} = \text{constant}.\exp(At)$$

in the same way as for the elastic reaction. Values for the slope A are given in Table (21) for the energy range 4 to 11·5 Gev/c.

TABLE 21

Slope of the differential cross sections ($Gev^{-2}$)

| Final state | 4 Gev/c* | 5 Gev/c | 8 Gev/c[41] | 11·5 Gev/c |
|---|---|---|---|---|
| $p\pi^+$ | 7·3 ±0·2 | 7·0 ±0·2 | 7·5 ±0·1 | 7·9 ±0·4 |
| $N^{*++}\pi^o$ | 7·1 ±0·6 | 8·1 ±0·8 | 7·5 ±0·7 | 9·0 ±1·1 |
| $p\rho^+$ | 8·0 ±0·9 | 8·7 ±1·1 | 8·4 ±0·9 | -- |

*Calculated from the differential cross section of reference (24)

The interesting point is that the quasi-two-body reactions exhibit slopes in the region of 7-9 $Gev^{-2}$ of the same order as that for elastic scattering suggesting an optical model description in which $A = (R/2)^2$ where R is the radius of the interaction volume. However, it has been found that certain quasi-two-body processes do not show such a slope ($N^{*++}\omega^o$ exhibits a slope of 3·2 $Gev^{-2}$ (41)) indicating that such an optical picture, representing the passage of a particle through an absorbing medium, is only qualitative.

The no-fit reaction

$$\pi^+p \rightarrow \pi^+p\pi^o\ (m\pi^o)\ m\geqslant 1$$

shows copious resonance production, especially at 5 Gev/c where the $N^{*++}(1236)$ isobar is dominant in the $p\pi^+$ system, and also the $\eta^o(550)$ meson in the missing neutrals system. There is also quite significant production of the quasi-two-body

processes

$$\pi^+ p \rightarrow N^{*++} \eta^o$$
$$\pi^+ p \rightarrow N^{*++} f^o$$

In the ($\pi^+$+missing neutrals) spectrum the $A_2(1300)$ meson has been observed, and there is also evidence for the $A_3(1640)$ meson.

At 11·5 Gev/c, although $N^{*++}$ production is still prevalent, there is no clear evidence for $\eta^o$ production in the missing mass spectrum. There is still some evidence for the quasi-two-body states above, but the statistics are small as yet. The $A_2$ enhancement is still present at 11·5 Gev/c but the $A_3$ is not seen.

## ACKNOWLEDGMENTS

The author wishes to thank Professor G.D. Rochester for his encouragement and interest in the work and Dr J.V. Major, his supervisor, for his guidance and help throughout. He would also like to thank his colleagues Dr D. Evans, Mr R. Maddock, and Dr S. Scarrott for their assistance with various stages of the analysis, and for many helpful discussions.

His thanks are also due to the technical staff of the Physics Department. In particular to Mr E. Lincoln and Mr C. Mullaney for maintaining the measuring machines, Mrs E. Errington, Mrs J. Gibson, Mrs T. Richardson, Miss D. Richmond, and Miss D. Wood for their painstaking work in measuring the events and drawing the diagrams, and to Mr M. Lee for his work in photographing the diagrams. Thanks are also due to the personnel of the CERN proton synchrotron, the 02 and U3 beams, the CERN 2m chamber, and the British National bubble chamber.

Finally, the author would like to thank the Science Research Council for a studentship and for travel grants.

## REFERENCES


1. T. Lee and C. Yang
   Il Nuovo Cimento 3, 749 (1956)
2. M. Gell Mann
   Il Nuovo Cimento 4, 2848 (1956)
   K. Nishijima
   Progress Theoretical Physics (Kyoto) 13, 285 (1955)
3. M. Gell Mann
   California Institute of Technology CSTL 20 (1961)
4. Y. Ne'eman
   Nuclear Physics 26, 222 (1961)
5. S. Okubo
   Progress Theoretical Physics 27, 949 (1962)
6. V. Barnes et al
   Physical Review Letters 12, 204 (1964)
7. F. Gursey and L. Radicati
   Physical Review Letters 13, 173 (1964)
8. M. Foccaci and G. Giacomelli
   CERN report 66-18 (1966)
9. B. Svensson
   CERN report 67-24 (1967)
10. G. Chew and F. Low
    Physical Review 113, 1640 (1959)

11. J. Jackson
Review of Modern Physics 37, 484 (1965)

12. E. Ferrari and F. Selleri
Il Nuovo Cimento 24, 453 (1962)

13. F. Selleri
Physics Letters 3, 76 (1962)

14. U. Amaldi and F. Selleri
Il Nuovo Cimento 31, 360 (1964)

15. N. Sopkovitch
Il Nuovo Cimento 26, 186 (1962)

16. K. Gottfried and J. Jackson
Il Nuovo Cimento 34, 735 (1964)

17. M. Jacob and G. Wick
Annals of Physics 7, 404 (1959)

18. B. Svensson
Il Nuovo Cimento 37, 714 (1965)

19. K. Gottfried and J. Jackson
Il Nuovo Cimento 33, 309 (1964)

20. S. Treiman and C. Yang
Physics Review 8, 140 (1962)

21. L. Stodolsky and J. Sakurai
Physical Review Letters 11, 90 (1963)

22. A-B-B-B-H-L-M Collaboration
Physics Letters 10, 229 (1964)

23. A-B-B-B-H-L-M Collaboration
Il Nuovo Cimento 31, 729 (1964)

24. A-B-B-B-H-L-M Collaboration
Il Nuovo Cimento 34, 495 (1964)

25. A-B-B-B-H-L-M Collaboration
Il Nuovo Cimento 35, 659 (1965)

26. A-B-C Collaboration
Physics Letters 12, 356 (1964)

27. A-B-C Collaboration
Physics Letters 19, 608 (1965)

28. A-B-C Collaboration
Physics Letters 22, 533 (1966)

29. R. Lynch et al
Physics Letters 9, 359 (1964)

30. M. Ferro-Luzzi et al
Il Nuovo Cimento 36, 1101 (1965)

31. T. Regge
Il Nuovo Cimento 14, 951 and 18, 947 (1959)

32. G. Chew and S. Frautschi
Physical Review Letters 7, 394 (1961)

33. W. Blum
CERN Internal Report TC/NBC 65-4 (1965)

34. P. Fleury, P. Shephard, and R. Vanderhaghen
CERN Internal Report TC/NBC 65-2 (1965)

35. C. Kitchen

Durham University Thesis (1967)

36. K. Foley et al

Physical Review Letters 19, 330 (1967)

37. A. Citron et al

Physical Review Letters 13, 205 (1964)

38. E. Fett

CERN Internal Report (1965)

39. C. Alff et al

Physical Review Letters 9, 322 (1962)

40. A-B-B-B-H-L-M Collaboration

Physical Review 138, B897 (1965)

41. A-B-C Collaboration

CERN /D.PH.II/PHYSICS 68-20 (1968)

42. A-B-B-B-H-L-M Collaboration

Physics Letters 10, 248 (1964)

43. S. Frautschi and B. Margolis

CERN Internal Report TH 909 (1968)

44. J. Jackson

Il Nuovo Cimento 34, 1644 (1964)

45. A. Daudin et al

Physics Letters 7, 125 (1963)

46. A-B-B-B-H-L-M Collaboration

Physics Letters 2, 229 (1964)

47. R. Thews

M.I.T Preprint (1966)

48. J. Jackson et al

Physical Review 139, B428 (1965)

49. J. Baton et al

Physics Letters 25B, 419 (1967)

Nuclear Physics B3, 349 (1967)

50. Z. Bhuiyan

Durham University Thesis (1967)

51. M. Ioffredo et al

Physical Review Letters 21, 1212 (1968)

52. D-G-H-M-S Collaboration

Report to Vienna Conference (1968)

53. A-B-C Collaboration

Physics Letters 18, 351 (1965)